

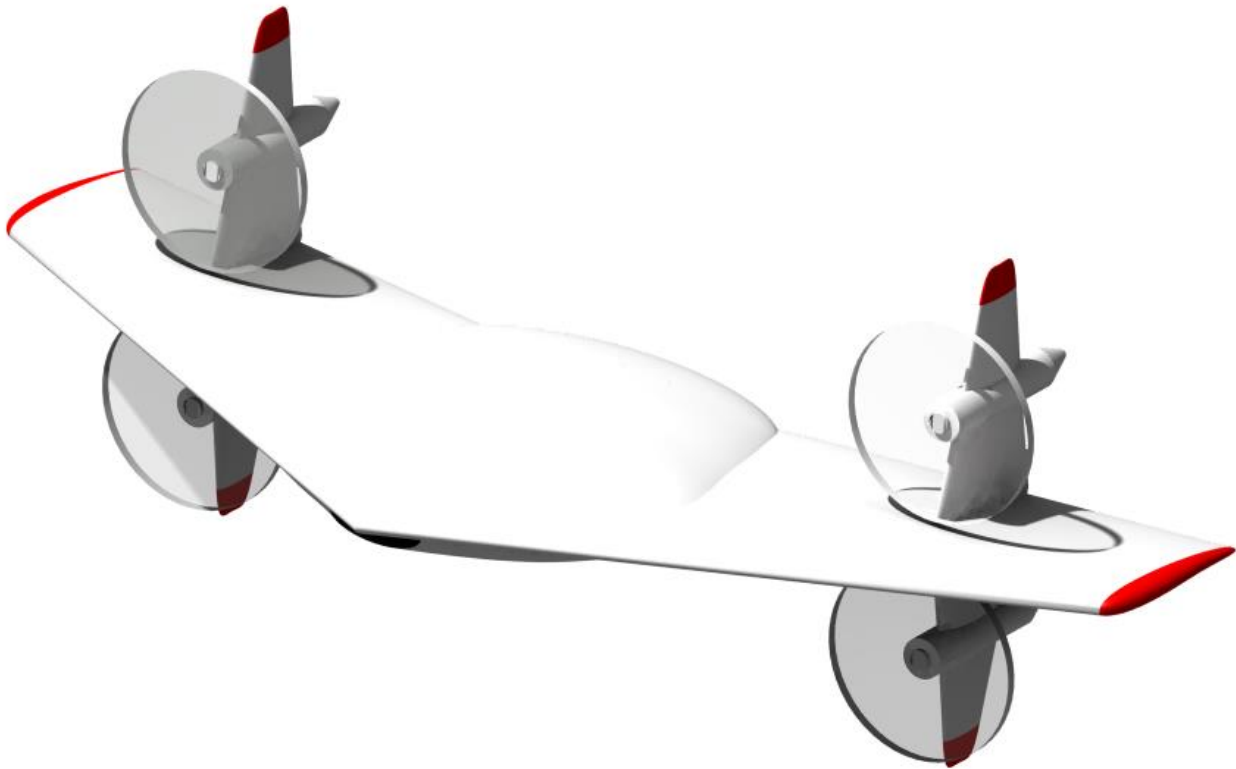
Department of Precision and Microsystems Engineering

Dr.One

'Realizing a small UAV for medical transport in developing countries'

Ferdinand Peters

Report no : EM 2014.016
Coach : Dr.ir. P. Tiso
: Drs. G. Poppinga (NLR)
: Dr. A.A. Zadpoor
Professor : Prof.dr.ir A. van Keulen
Specialisation : Engineering Mechanics
Type of report : Master Thesis
Date : 24 June 2014



DR.ONE

REALIZING A SMALL UAV FOR MEDICAL TRANSPORT IN DEVELOPING COUNTRIES

by

Ferdinand Peters

in partial fulfillment of the requirements for the degree of

Master of Science
in Mechanical Engineering

at the Delft University of Technology,
to be defended publicly on Tuesday June 27, 2014 at 14:00 AM.

Supervisor:	Prof. dr. ir. A. van Keulen	TU Delft
Thesis committee:	Dr. ir. P. Tiso,	TU Delft
	Drs. G. Poppinga,	NLR
	Dr. A.A. Zadpoor,	TU Delft

This thesis is confidential and cannot be made public until December 31, 2014.

An electronic version of this thesis is available at <http://repository.tudelft.nl/>.

Preface

The potential of the use of Unmanned Aerial Vehicles (UAV) for medical transportation has been recognized and these initiatives have already received some publicity, such as Matternet [10]. This concept includes establishing a futuristic infrastructure of landing platforms all over Africa, but considering the stark realities of the severe lack of resources I felt this was not the right approach. Developing a hybrid drone that combines the UAV's performance in flight with the VTOL capabilities of being able to land almost anywhere would increase the operational range and eliminate the need for a landing platform infrastructure and therefore be more adaptable to the conditions in which it would operate. Given the same concerns of the critical lack of resources I believe it is also necessary to create a design that would be cheap and easy to operate and maintain locally. A design that is mechanically as simple as possible constructed from simple inexpensive materials.

The project has allowed me to apply the wide variety of knowledge and skills I have obtained from my master PME (Precision and Microsystems Engineering) and my bachelors in Aerospace Engineering.

- Developing the log platform; I applied knowledge gained from - How to perform accurate measurements, process and analyze data, learned in the subjects Experimental Dynamics (WB1406-07) and Measurement in Engineering (WB2303-10).
- In the wing sizing; I applied Optimization techniques taught in Optimization (WB1440).
- The dynamic model was derived using the theory taught in Engineering Dynamics (WB1218-07) and Multibody Dynamics B (WB1413-04). Together with mathematical background of Engineering Mechanics Fundamentals (WB1451-05) and the software knowledge from Matlab in Engineering (WB1443).
- In the motor tests; Knowledge of electrical circuits and their characteristics were applied and obtained as part of the course Mechatronics System Design (WB2414-09).

Knowledge in flight conditions, flight performance, aerodynamics, came from My Bachelors in Aerospace Engineering.

My experience in Radio Control (RC) flying helped me considerably in the project since I was aware of what was available on the market and allowed me to see the potential

of using these off-the-shelf and relatively low-cost electronics with open source software to control new systems. Moreover it helped in the building of the first prototype and testing the equipment.

Dr.One also made me explore areas which were new to me. On the technical side; micro controller programming, serial interfacing and data processing in different languages, Java, C++, C. Autopilot configuration, soldering electronic components on PCB boards, 3D milling and hot-wire cutting.

Project management and business; from its conception, the potential of the Dr.One project has been recognized. So as the technical project leader I have not only been challenged by the technical side but also the business side as my role required me to be involved in the process of promotion, developing a business plan, finding partners and financial support.

For the Dr.One project I developed some specific tools and conducted specific research myself:

- Design tool (development and testing) (chapter 4 - 11)
- Verification of the log platform (appendix J)
- Motor tests for experimental determination of motor characteristics (development and testing) (appendix G.2)
- Propeller motor matching (static and dynamic) (section 8)
- A layout for the dynamic Analysis (section 10.3)
- Using quad copter control for horizontal flight (i.e. no control surfaces) and a first step in control design and analysis (chapter 11)

Acknowledgments

I would like to thank everybody who was involved in this project including:

Intern colleges at NLR's UAS laboratory for the inspiring atmosphere and in particular the following people:

- Ludovic Tyack: teaching serial connection and data processing in Java
- Aran Dokoupil: design of circuit boards
- Coen Fransen: assisting in the motor tests
- Laura Schmidt: manufacturing of Dr.One

NLR Personnel for their advice:

- Skander Tamaalah: for the advanced dynamic computer model and expertise on dynamics and control
- Martijn Roelofsch: sensors for the log platform
- Harm van Gilst: interface and programming
- Jacco Domunicus: dynamics and control
- Christian Muller: autopilot advice and flying skills as a pilot
- Roalt Aalmoes: Raspberry PI

People who have supported the project from the start:

- Miriam Janssen op de Haar (AMREF): for her endless time and energy on the business side
- Gerard ten Buuren (Politie): for his critical questions and the printing of the 3D scaled model

My loving father Mike Senneck for his endless efforts in revising the report and his support throughout the project.

Abstract

This thesis presents the development of a small UAV, Dr.One for transporting medical supplies in developing countries. After consultations with concerned parties, a range of applications have been established. These are, establishing the final link in the supply chain, the urgent delivery of medical supplies, blood sample collection and the reaching of locations that are inaccessible by other means of transport.

Ghana has been selected as the beachhead market. Estimating €2500 per system and €2000 for a repair facility, brings the Total Addressable Market to 5.5 million euros, which is 0.46 euro per person living in remote areas.

The Dr.One project will start in the upper East region and will roll out to the upper West and the Northern region.

The project development master plan has been established for the TRL levels I-II

The design of Dr.One has 3 critical design requirements, VTOL, Long range and high flight speed.

A new type of UAV was required for the purpose which combined the VTOL capabilities with the flying characteristics of a fixed wing. This four motor hybrid configuration is a combination of a flying wing and a quad copter. The dimensions of Dr.One are kept flexible to design for specific needs.

A design tool has been developed to allow for rapid design around the needs of the payload. No technical expertise is needed as all relevant decisions are automatically made by the design tool itself. The main focus points of the design tool are: scalability, easy to use, modular approach, affordability.

The design tool consists of a sequence of events, starting with body sizing relative to the needs of the payload dimensions and the wing and propulsion sizing relative to the performance requirements.

The body is sized in two planes, which are combined into a 3D body. The side consists of a NACA-Airfoil and the front-plane consists of a cosine or a spline fit. The wings are sized using an optimization scheme for range. The minimum drag is determined, using the wingspan and the root chord as design variables.

To size the propulsion, the characteristics including the efficiency curves of the motors have to be known. The efficiency curve of a motor is calculated in three different manners, from data from the manufacturer, an online tool eCalc and experimentally with a developed setup. The shape of the curve is similar for the three methods but the absolute values of the efficiency differ: the online tool is too optimistic, the test data

of the manufacturer is accurate for perfect conditions and the experimental setup is slightly too pessimistic since heat losses from the DC motor used as the torque meter are incorporated in the results.

The motor is coupled to a range of propellers. Using wind tunnel data the performance of the propellers can be obtained accurately. The motor's torque is matched to the propeller's torque resulting in the complete propulsion system. The efficiency curve of the motor is multiplied with the efficiency curve of the propeller to determine the effective range of rotational velocities.

For the design of Dr.One the propeller motor combination with the least drawn current was selected to obtain maximum endurance.

An example case is given which guides the reader through the design process.

The body and wings are manufactured using 3D-milling and hot-wire cutting techniques, which have been proven in the process of constructing prototypes.

A dynamic model has been created using rigid body dynamics. A more advanced model is used to simulate the aerodynamics of the propellers and the wing.

A systematic approach to the dynamic analysis has been laid out on this model, however first the model should be validated before any collaborated results can be established.

To validate the model flight tests have to be performed and logged at high frequency (100Hz). A log platform has been created for this purpose and has been tested successfully.

The controls of Dr.One consist of two modes, the vertical control mode and the horizontal control mode. The vertical is a quad copter control mode. For the horizontal mode the vertical control mode is rotated 90 degrees, resulting in a pitch that has rotated 90 degrees, the roll becoming the yaw and the yaw becoming the roll.

An approach on how to determine the gains for a PID control system has been laid out and performed for the pitch on the non-validated model. The gains found by the tuning algorithms on the linearized system are consistent with expected results.

Future

A prototype has been built and fitted with a programmable autopilot and flight tests are being carried out. After the autopilot is configured in vertical mode (quad copter) the configuration will be frozen, test flights will be carried out and the model will be validated.

Contents

Preface	i
Acknowledgments	iii
Abstract	v
List of Terms	xiii
1 Introduction	1
2 Problem definition	3
2.1 Applications	3
2.1.1 Urgent medical supply	4
2.1.2 Final link in the supply chain	4
2.1.3 Unreachable locations	4
2.1.4 Blood sample collection and Lab on a chip	4
2.2 Advantages and Disadvantages using a UAV	5
2.3 Business and project management	6
2.4 Pilot and roll out strategy	7
2.5 Conclusion	7
3 Design	9
3.1 Requirements	9
3.1.1 VTOL	9
3.1.2 Long range	9
3.1.3 High flight speed	9
3.2 Type of UAV	10
3.3 Hybrid system	10
3.4 Chosen configuration	10
3.5 Conclusion	11
4 Design Tool	13
4.1 Main focus points	13
4.1.1 Scalability	13

4.1.2	Easy to use	14
4.1.3	Modular Approach	14
4.1.4	Affordability	14
4.2	Design methodology	14
4.2.1	Payload	17
4.2.2	Wing sizing	17
4.2.3	Motor selection	18
4.2.4	Propeller selection	18
4.3	Production	18
4.3.1	Body	18
4.3.2	Wings	19
4.4	Conclusion	19
5	Body Sizing	21
5.1	Side-plane	21
5.2	Front-plane	22
5.2.1	Cosine fit	22
5.2.2	Spline fit	23
5.2.3	Comparison	24
5.3	3D-Body	24
5.4	Nose	25
5.5	Body parameters	27
5.6	Manufacturing the body	27
5.7	Conclusion	27
6	Wing sizing	29
6.1	Airfoil	29
6.2	Parameterization wing	30
6.3	Objective function	31
6.3.1	Flight condition	31
6.3.2	Lift and drag forces	32
6.3.3	Weight estimation	33
6.3.4	Maximum range	33
6.4	Production	33
6.5	Conclusion	33
7	Motor selection	35
7.1	Motor characteristics	35
7.1.1	Selected motor	35
7.1.2	Performance characteristics using test data from manufacturer	36
7.1.3	Theoretical tool eCalc	38
7.1.4	Test results	38
7.2	Conclusion	39
7.2.1	Recommendations	40

8 Propeller Performance	41
8.1 Propellers parameters effects on performance	42
8.2 Motor and propeller matching	43
8.3 Static Thrust	47
8.4 Conclusion	48
9 Example Design	49
9.1 Improving the range	52
10 Dynamic Model	53
10.1 Rigid body dynamics	53
10.2 Advanced Model	56
10.2.1 Dr. One representation	57
10.3 Dynamic analysis	58
10.4 Trim	58
10.5 Eigenmotions	59
10.6 Conclusion	60
11 Control	61
11.1 Vertical flight controls	61
11.2 Horizontal flight controls	62
11.3 Control design	63
11.4 Control on linearized system	65
11.5 Pitch control	65
11.5.1 Linear system	66
11.5.2 Non-linear system	67
11.6 Roll and yaw control	69
11.7 Vertical and horizontal flight controls	69
11.8 Model validation	70
11.9 Flight Tests	70
11.9.1 Verification sensors	71
11.9.2 Test maneuvers for model validation	71
11.10 Validation of log platform	71
11.11 Future	71
11.12 Conclusion	72
12 Conclusion	73
A Existing UAV	75
A.1 Multitrotor systems	75
A.1.1 Principle	76
A.1.2 Payload	76
A.1.3 Flight velocity	76
A.2 Fixed wing systems	76

A.2.1	Principle	76
A.2.2	Payload	76
A.2.3	Flight velocity	77
A.2.4	Conclusion	78
A.3	Hybrid UAVs	78
A.4	Quadshot	78
A.5	ATMOS	79
B	Flight scenario	81
C	Development master schedule	85
D	Naca 4 digit airfoil shape	89
E	Analyzing design variables	91
E.1	Wingspan and flight speed on minimum drag	91
E.2	Brute force method	94
F	Thrust and Power coefficients	97
F.1	Thrust coefficient	97
F.2	Power coefficient	98
G	Motor Test	99
G.1	Data of manufacturer	99
G.2	Set up	101
G.2.1	DC motor as torque meter	101
G.2.2	Torque measurements	103
G.3	Test results	105
G.4	Motortest measurements	106
G.4.1	$K_{T_{dc}}$	106
G.4.2	Motortest	107
H	Static Thrust MK3638	109
H.0.3	Weight estimation	112
H.1	Drag estimation body	113
I	Manufacturing of the body	115
J	Log Platform (Flight recorder)	117
J.1	Required data	117
J.2	IMU	118
J.2.1	Communication setup	119
J.2.2	Calibration	120
J.2.3	Stationary test	120
J.2.4	EKF tuning	127

J.2.5	Checklist IMU	128
J.2.6	Train test	129
J.2.7	delay	137
J.3	Altitude	139
J.3.1	Test	139
J.3.2	Height test	141
J.4	Noise	143
J.5	Altitude derivation for baro meter	144
J.6	RPM measurements	148
J.6.1	Square wave test	148
J.6.2	Motor test	149
J.6.3	Rotational velocity	149
J.7	Interface	151
J.7.1	Baro	155
K	Autopilot	157
L	Attitude control	161
L.1	Feedback PID	161
L.2	Feedforward control	162
M	Flight test	163
M.1	Sweeps	163
M.2	Steps	165
N	Checklist for flight test	167
N.1	IMU	167
O	Checklist for flight test	169
O.1	IMU	169

List of Figures

1.1	The present and the future	1
3.1	Dr. One	11
4.1	Design methodology	15
4.2	Design tool flow chart	16
4.3	Meaning of icons	17
4.4	Body design	17
4.5	Wing design	18
5.1	Side view of body design generation for different payload dimensions . . .	22
5.2	Spline fit	23
5.3	Front view of body design generation for different payload dimensions using a cosine fit and a spline fit function	24
5.4	Body design generation for different payload dimensions	25
5.5	Adding the nose onto the body design	26
5.6	Body shaping side with added nose of $dc = 0.1\text{m}$	26
6.1	MH-60 airfoil	29
6.2	Parameterization of the wing	30
6.3	Flight condition	31
7.1	Robbe Roxyy 2827-34 Outrunner [1]	36
7.2	Results Robbe 2827 torque vs ω and current from manufacturer	36
7.3	Results Robbe 2827 torque vs P_{elec} and P_{mech} from manufacturer	37
7.4	Results Robbe2827 torque vs η from manufacturer	37
7.5	eCalc motor characteristics of 2728-34	38
7.6	Results Robbe2827 torque vs η from test setup	39
8.1	The selected propellers	41
8.2	Effect of diameter of efficiency	42
8.3	Effect of pitch of efficiency	42
8.4	Effect of rotational velocity of efficiency, for the 10x4.7 slow flyer	43
8.5	Efficiency curves of the motor and propellers	44

8.6	Rotational velocity (ω) matching for propeller and motor	45
8.7	Efficiency curves	45
8.8	Total efficiency curves as a function of torque	46
8.9	Rotational velocity vs Torque for the propeller and Robbe Roxxy 2827-34	47
9.1	3D body	50
9.2	Dr.One design	51
10.1	Dynamic model calculation sequence	57
10.2	Flow chart dynamic analysis	58
10.3	Pitch angle at trimmed condition for different velocities u	59
10.4	Eigenvalues for the Dutch roll for different velocities u	60
11.1	Control modes of a quadcopter	62
11.2	Control modes of Dr.One	63
11.3	Control design scheme, the different colors represent the different models, linear, non-linear, real flight respectively	64
11.4	DrOne configuration of the motors	66
11.5	K_p for different trimmed velocities u	66
11.6	K_p, K_i, K_d for different trimmed velocities u	67
11.7	K_p, K_i for different trimmed velocities u	68
11.8	Non-linear simulation at hover ($u=[0\ 0\ 0]$) using a PI controller	68
11.9	Non-linear simulation at hover ($u=[0\ 0\ 0]$) using a PID controller	69
A.1	Different multirotor configurations [2][3][4]	75
A.2	Performance comparison multicopters and fixed wing aircraft	77
A.3	Hybrid UAVs [5] [6]	78
B.1	Time line mission for Dr.One	81
B.2	Time line mission for Dr.One	84
C.1	TRL I-IV	85
C.2	Planning TRL I-II	86
C.3	TRL IA	86
C.4	TRL IB	87
C.5	TRL IIA	87
C.6	TRL IIB	88
C.7	TRL cost estimation	88
E.1	Wingspan and flight speed against drag	91
E.2	Drag curve for $b = 0.8\text{m}$	92
E.3	Drag curves for increasing wing geometry	92
E.4	D_{min} for different root chord and tip chord	93
E.5	Wing geometry initial design	94

G.1	Results Robbe 2827 torque vs current from manufacturer	99
G.2	Results Robbe 2827 torque vs ω from manufacturer	100
G.3	Setup for motor characteristics	101
G.4	Setup for measuring k_V	102
G.5	Setup for measuring k_V	102
G.6	measuring K_V for powered and driven tests	103
G.7	Setup for measuring motor characteristics	104
G.8	Final setup for measuring motor characteristics	104
G.9	Results Robbe 2827 torque vs current from test setup	105
G.10	Results Robbe 2827 torque vs ω from test setup	105
H.1	Efficiency curve for MK3638 and Robbe Roxxy 2827-34	109
H.2	Extrapolation of C_t and C_p	110
H.3	Static thrust for MK3638	110
I.1	PyCam screenshot, imported <i>.stl</i>	115
I.2	Tool path for rough and finish milling of the body	116
I.3	Tool path reduction	116
J.1	CH Robotics CHR-UM6 IMU	118
J.2	Measured accelerations in default settings	121
J.3	Accelerations after bias correction	121
J.4	Angular velocities in default settings	122
J.5	Angular velocities in default settings	123
J.6	Angular velocities after zero rate gyros command	123
J.7	Bias with equal rotations as calibration method	124
J.8	Bias with random rotations as calibration method	125
J.9	Euler angles with default settings	126
J.10	Euler angles after sending reference vector command	126
J.11	Bias stabilized after reference vectors commands	127
J.12	Attitude in Euler angles in stationary position	127
J.13	Attitude in euler angles in stationary position with EKF tuning	128
J.14	Train experiment setup	129
J.15	Accelerations in the body fixed frame of the train test	130
J.16	FFT of the accelerations	130
J.17	Accelerations with a low pass filter	131
J.18	Euler angles of the train running on a track	131
J.19	FFT of Euler angles	132
J.20	Euler angles with a low pass filter	133
J.21	Quaternion representation of the train test	133
J.22	FFT of quaternions	134
J.23	Quaternion representation with low pass filter	135
J.24	Euler angles using filtered signal of quaternions	135
J.25	Velocity estimates obtained from accelerations	136

J.26	Position estimates obtained from accelerations	137
J.27	Euler angle ϕ of the train with both time vectors	137
J.28	Delay vs time	138
J.29	The MS5611 Barometer [7]	139
J.30	Temperature measurement from MS5611	140
J.31	Pressure measurement from MS5611	140
J.32	Altitude measurement from MS5611	141
J.33	The height of the shelves of the closet	142
J.34	The measured pressure during the heighttest. NOTE the test starts at $t = 60$ to let the barometer stabilize before the test	142
J.35	Heighttest: the test starts at $t = 60$ to let the barometer stabilize before the test	143
J.36	Lab Power Device [8]	144
J.37	Noise comparison with different power sources	144
J.38	Function generator [9]	148
J.39	Output of the function generator shown on channel 1	148
J.40	Output RPM sensors at a 100Hz square wave	149
J.41	Layout of the sensors connected to the Raspberry PI	151
J.42	Circuit board with the components	151
J.43	The Polulu USB connector incorporated in the circuit board	152
J.44	The Cortex μC incorporated the circuit board	152
J.45	Circuit board powered up and functional	153
J.46	Layout of the interface for the CHR-UM6 IMU sensor	153
J.47	Layout of the sensors connected to the Raspberry PI	155
K.1	Attitude control loop	157
K.2	XFLR5 screenshot for wing of Dr.One	158
K.3	XFLR5 finding the neutral point	159
M.1	Flight test pitch sweep	163
M.2	Flight test roll sweep	164
M.3	Flight test yaw sweep	164
M.4	Flight test pitch step	165
M.5	Flight test roll step	165
M.6	Flight test yaw step	166

List of Tables

- 2.1 Total addressable market for Ghana 7
- 7.1 Parameters at maximum efficiency 38
- 7.2 Parameters at maximum efficiency 38
- 7.3 Parameters at maximum efficiency 39
- 8.1 The selected propellers 41
- 8.2 Propeller comparison 46
- 8.3 Static thrust with Robbe Roxxy 2827-34 47
- 9.1 Payload definition 49
- 9.2 Fuselage parameters 50
- 9.3 Wing parameters 51
- 11.1 Gains at vertical and horizontal flight 70
- E.1 Wing parameters initial design 93
- G.1 Powered test DC motor 106
- G.2 Driven DC motor test for determination of torque constant $K_{T_{dc}}$ 107
- G.3 Motor characteristics test Roxxy 2827-34 at 12V 107
- H.1 Static thrust with MK3638 111
- J.1 Communication setup parameters 120
- J.2 Communication setup parameters 120
- J.3 Calibration method 124
- J.4 Checklist before measurements 129
- N.1 Communication setup parameters 167
- N.2 Checklist before measurements 168
- O.1 Communication setup parameters 169
- O.2 Checklist before measurements 170

List of Terms

- A Amplitude. 22
 α Angle of attack. 53
 AR Aspect ratio. 32
- b wingspan. 30
 β Propeller diameter. 42
 b_f Width of the body. 23
- c_b Resizing coefficient. 22
 c_b Width vector. 23
 C_d Drag coefficient. 32
 C_{d_0} zero lift drag coefficient. 33
 C_{d_1} induced drag coefficient. 33
 C_{d_f} Drag coefficient body. 27
 C_f Skin friction coefficient. 27
 C_l Lift coefficient. 32
 C_p Power coefficient. 41
 C_t Thrust coefficient. 41
- D Drag force. 31
 d Propeller pitch. 42
- e Oswald factor. 32
 η Efficiency. 37
- f_{LD} Fuselage length ratio coefficient. 27
 f_M Mach number coefficient. 27
- I Current. 37
 i Index. 55
- J Advance ratio. 41
 \mathbf{J} Inertia tensor. 55
- \mathbf{Kd} Differential gain. 65
 \mathbf{Ki} Integral gain. 65

- K_p** Proportional gain. 65
- L* Lift force. 31
- λ Quaternion elements. 55
- l_r Root chord. 30
- l_t Tip chord. 30
- M_G Moment. 55
- ω Rotational velocity. 36
- p* Rotational velocity around x-axis. 53
- P_{elec} Electrical power. 36
- P_{mech} Mechanical power. 36
- ϕ Euler angle around x-axis, roll. 53
- π ratio of circumference of circle to its diameter. 32
- ψ Euler angle around z-axis, yaw. 53
- ψ Sweep angle. 30
- Q* Torque. 36
- q** Quaternion. 55
- q* Rotational velocity around y-axis. 53
- r* Rotational velocity around z-axis. 53
- ρ Density of air. 32
- S* Wing area. 32
- S_b Wetted area of the body. 27
- T* Thrust. 46
- F_t Thrust force. 32
- θ Euler angle around y-axis, pitch. 53
- UAS** Unmanned Aerial Systems. viii, 1
- UAV** Unmanned Aerial Vehicle. viii, 2
- V* Flight speed. 32
- v** Velocity vector. 54
- V* Voltage. 36
- L* Weight. 32
- Y** State vector. 56

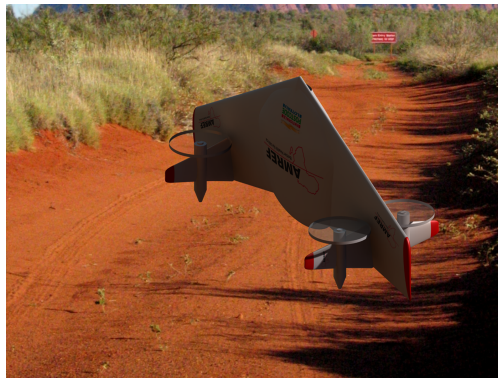
Chapter 1

Introduction

The concept of Dr. One was conceived and evolved in response to the demand for an effective means to deliver essential medical items to remote areas where using existing means of transportation is very difficult due to extreme conditions or not feasible due to high costs. In many areas of the world, Africa in particular, many people live where medical supplies are difficult to deliver see figure 1.1(a). Using traditional manned aircraft is often not considered viable due to very high costs, the dangers it presents to personnel, limited availability and that it takes too much time to arrange.



(a) Land transportation



(b) Dr.One

Figure 1.1: The present and the future

The new technological advances in the domain of Unmanned Aerial Systems (UAS), could provide an effective solution to many of the logistical problems associated with operating in such difficult conditions. Medical products and services could be delivered much faster and be more patient focused. Infrastructures could be developed around the capabilities of the system, for example the quick delivery of samples to laboratories for diagnostics and treatment and the delivery of essential medical supplies directly to where they are needed.

This master thesis will show how the development of an Unmanned Aerial Vehicle (UAV) specifically designed for the purpose see figure 1.1(b), that takes into consideration all the key factors associated with operating in such difficult conditions, could be a viable solution.

Chapter 2 defines the problem and possible areas of application. Chapter 3 the requirements for the design of Dr.One are explained as the chosen configuration. Chapter 4 until chapter 8 show the specially developed design tool for rapid design of Dr.One. Chapters 10 and 11 show the dynamics and possible control system for Dr.One.

Chapter 2

Problem definition

The logistics of providing health care items and services when and where they are needed in such countries as Africa has always been extremely difficult and is considered a major factor inhibiting the delivery of effective health care.

Overcoming the problems imposed by extreme weather conditions and their effect on the existing infrastructure, difficult terrain, hostile environment, lack of infrastructure, very limited resources and a lack of technical expertise is a real challenge but is possible by avoiding the physical problems by flying over them and developing an automated system that can be operated at very low cost with a minimum of expertise.

The development of a new type of UAV (Unmanned Aerial Vehicle) for logistical purposes would help overcome some of the challenges the continent faces. This thesis will focus on the development of mechanical tools that allow for the building of such a UAV. This UAV will be referred to as Dr.One.

This chapter determines the problem definition and possible applications for Dr.One. These definitions are developed in consultation with concerned parties and have evolved during throughout the project. Finally a section is committed to the business and project management side of the Dr.One project.

2.1 Applications

A range of possible specific applications for Dr One have been researched and evaluated in consultation with different parties that are continually confronted with the problems associated with providing healthcare in Africa. The Dr.One project works closely with AMREF flying doctors, which is an African based non-profit organization for providing health care throughout the continent. The director of International Health Consultants (AMPC) with his years of practical in the field experience together with aerospace experts within Dutch Aerospace laboratory (NLR) were brought together to explore and develop possible applications for Dr.One considering the conditions and the available technology. This has resulted in a better understanding of the applications and cases for which a Dr.One could be deployed. A specific use case has also been provided by the director of a regional hospital in Ghana.

- Urgent medical supply
- Final link in the supply chain
- Unreachable locations
- Lab on a chip

These cases are discussed below.

2.1.1 Urgent medical supply

For delivering urgent medical supplies to treat victims of accidents or complications during child-birth, Dr.One would be a good alternative for existing transporters. Currently this kind of medical supply can only be done by helicopters, which are very expensive to operate and maintain in contrast to Dr.One which is cheap and flexible. Moreover due to its small size it could land in smaller spaces than the larger manned helicopters. Most likely examples are:

- Flying First-aid kit carrying supplies to stabilize patients before sending to hospital.
- Blood for transfusion, many lives have been lost by transfusion blood not able to arrive in time or arrive at all. Therefore this could be a useful payload when deployed for urgent medical supply.

2.1.2 Final link in the supply chain

Dr.One could also be deployed as the final link in the supply chain to more remote locations. In the case of Ghana at the moment these journeys have to be completed by road. The driver and jeep are relatively cheap but slow. The direct flight distances would not be long but by road navigating around obstacles such as mountains and rivers makes the journey by road much longer and time consuming and sometimes dangerous. Significant time reduction could be achieved by using Dr.One. A quick and efficient means of delivering vaccines would be invaluable when dealing with epidemics and a fast and efficient means of delivering vital specimens to laboratories for analysis would aid treatment.

2.1.3 Unreachable locations

Dr One could be a valuable asset as in the rainy season many roads are impassable making it impossible to supply health care over land. Using a UAV would make it possible to maintain the supply of essential items

2.1.4 Blood sample collection and Lab on a chip

Dr.One could also be deployed for sending blood samples to the lab quickly and efficiently. This data can be communicated to specialists and any vital specimens needed can be transported to laboratories for analysis.

Lab on a chip is a relatively new and promising development, that allows for the testing of blood samples on a portable chip locally. Dr. One could be fitted with a chip so as to perform blood testing on site. Dr. One could carry medication appropriate the most prevalent diseases to allow for immediate treatment.

2.2 Advantages and Disadvantages using a UAV

The main advantages of using a small UAV instead of existing means for medical transportation would be:

- Significantly lower cost than that of manned aerial transport
- Quicker response time
- Able to reach remote locations which have no road access
- Faster than transport over land

Limitations would be;

- Limited payload capacity
- Not possible to operate in bad weather conditions

The UAV can be deployed very rapidly. Apart from pre-flight preparation, no other precautions need to be taken. A trained pilot is not required significantly reducing the operating costs. Furthermore the size and propulsion system make it far cheaper than manned aircraft.

The cost-effectiveness makes the UAV suitable for missions for only one patient. Take for example a pregnant women in a remote village which needs to be tested for aids. Sending a manned aircraft in most situations would not be feasible, whereas a specifically designed UAV could be used effectively.

Dr. One should not be considered a replacement for existing transportation systems but as an additional alternative.

To safely operate Dr. One a procedure was developed and explained in appendix B.

2.3 Business and project management

Dr.One is a social enterprise consisting of a consortium of partners.

The Dr.One system will be implemented in the district/regional ecosystem and operated as a self-sustaining business. The market segment specifically focuses on health care in remote locations, where the end users are governments and (Health) Service providers. The lead customers are the UN, the Red Cross and AMREF.

Operational costs are variable depending on the number of systems and health workers involved and consist of:

- Initial Set-up
- Operations and maintenance
- Logging, trending and safety
- Billing
- Training of health workers
- Maintenance of routes and locations
- enabling the Dr.One program

The costs of Dr.One have been initially estimated at €2500 per system including the ground station. An additional €2000 will be needed to set up a repair facility. Ghana has been selected as the Beachhead market, or point of entry market. The reasons are:

- Relatively good working health system
- More than 50% of the population lives in remote areas
- Very challenging transport of small medical goods to/from remote areas
- Indicators for maternal and child health in the remote areas are poor.
- Stable country
- Tech savvy
- There is a long standing relationship between Ghana and the Netherlands

For Ghana the Total Addressable Market, which is a reference to the revenue opportunity has been analyzed. First the health sector has been broken down into all the possible clinics for this application. After which the required systems are estimated along with the required repair facilities. This is done for the upper East region, the North which consist of the upper East, upper West and Northern region and the total of Ghana.

	Teach	Reg	Psy	H	Poly	Health	Matern	CHPS	Total
Upper East	1	1	2	97	7	299	55	4	466
North	2	8	1	246	4	1784	334	375	2754
Ghana total	3	9	3	343	11	2083	389	379	3220
RS	1	10	0	10	1	1	1	1	
RRF	1	1	0	1	0	0	0	0	
Total RS	3	90	0	3430	11	2083	389	379	6385
Total RRF	3	9	0	343	0	0	0	0	355
TAM [k€]	4.5	81	0	3087	9.2	1736	324	316	5558

Table 2.1: Total addressable market for Ghana

Where:

- RS = required systems
- RRF = required repair facilities
- TAM = Total Addressable Market
- Teach = Teaching hospital, are
- Reg = Regional hospitals
- Psy = Psychiatric hospitals
- H = Hospitals
- Poly = Poly clinics
- Health = Health centers
- Matern = Maternal homes
- CHPS = Community-based Health Planning and Services

Making the assumption that TAM indicates the actual market, and considering the population of Ghana which is 2.5 million people and using the assumption that 50% live in remote areas gives the cost per person to be €0.46.

2.4 Pilot and roll out strategy

There are three target areas, the upper East region, which will function as the pilot area, the upper West region and the Northern region. These are the most remote areas, with the worst health indicators but with a good working CHPS system. When the system is operational the other regions can be included as well as other nations with a similar health system set-up, for instance Kenya, Tanzania and Uganda.

The development planning together with the cost estimation has been established using the Technology Readiness Level (TRL) definitions and is shown in appendix C.

2.5 Conclusion

In this chapter the problem definition has been determined, and four possible applications have been developed in consultation with concerning parties; Urgent medical

supply, final link in the supply chain, unreachable locations and blood sample collection. The advantages and disadvantages of the use of a UAV were discussed as well as the business and project management side of the Dr.One project, including the Total Addressable Market value of the chosen Beachhead market, Ghana. Finally the pilot target area and roll out strategy were shown.

Chapter 3

Design

This chapter explains the design of Dr.One. First the requirements established from the use cases defined in section 2.1 are explained. Then a section is committed to describing existing types of UAVs and their limitations and strengths and explaining why a new type of hybrid aircraft is required that combines the capabilities of both.

3.1 Requirements

Apart from Dr.One having to carry the specified payload, it needs to be able to have certain functionalities which are translated into critical design requirements. These critical design requirements are;

- Vertical take-off and landing (VTOL)
- Long range
- High flight speed

3.1.1 VTOL

To effectively reach remote locations and accident sites Dr.One should be able to land anywhere and take-off from the target site, without depending on a prepared runway.

3.1.2 Long range

Considering the distances from the district hospitals to an arbitrary location a target operating range of 100km is aimed for.

3.1.3 High flight speed

The great distances could be covered quickly. Based on comparable flying systems speeds of 70km/h are feasible and should be aimed for. This could be used as a starting point for the design of Dr.One, however higher flight speeds may be preferable in the the case where there is a urgent need for medical supplies.

3.2 Type of UAV

After carrying out a literature study on the performance of two types of UAVs, the multicopter and the fixed wing aircraft; see appendix A. It was established that both of these types of aircraft did not meet the requirements and what was needed is a combination of both the flight performance of the fixed wing aircraft and the VTOL capabilities of a multicopter. These systems are referred to as hybrid UAVs and are relatively new. Dr.One will take-off as a multicopter and transition into horizontal fixed flight. More information about the chosen configuration can be found in section 3.4.

3.3 Hybrid system

Several applications for Dr.One have been determined, namely delivering urgent medical supplies, accessing unreachable locations, providing the final link in the supply chain, lab on a chip. Based on these applications the requirements for Dr.One have been determined resulting in a aircraft system that has VTOL capabilities and the flight performance of a fixed wing aircraft. These considerations lead to the conclusion that there was a need for of a hybrid system that combined the characteristics of a multi-rotor and a fixed wing aircraft.

This report will explain the design of this UAV from a mechanical engineering perspective. Focusing more on the flexibility of the design tool, practicality of the design and the production process.

3.4 Chosen configuration

Considering the scope of its requirements, for the effective application of the Dr. One concept, a revolutionary new design was needed that accommodated the constraints and conditions in which it will operate. The development of miniature autopilots, control software and fast reacting brush-less electric motors, capable of controlling dynamically unstable configurations, allows for this and in the case of Dr.One has resulted in a design that consists of only four motors and a foam wing which eliminates the need for such mechanical moving parts as servos and control surfaces.

The result is shown in figure 3.1.

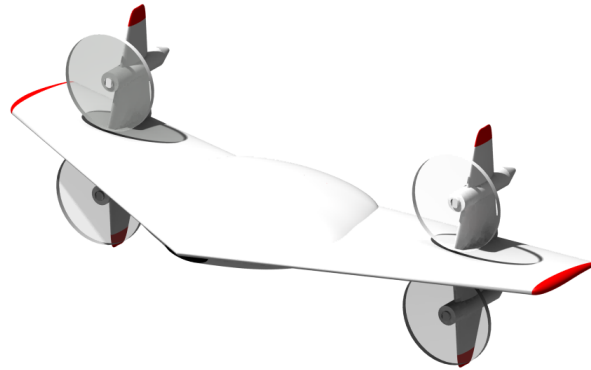


Figure 3.1: Dr. One

Reducing the design to a four motor hybrid flying wing configuration results in a design which is easy to build, assemble and maintain. Therefore minimizing the need for technical expertise and facilities.

3.5 Conclusion

This chapter explained the requirements derived from the used cases defined in section 2.1. The requirements were VTOL, long range and high flight speed. It was established that a new type of UAV was needed to comply with the requirements. This new type of UAV is referred to as a hybrid configuration and combines the VTOL capabilities of a multicopter with the flying performance of a fixed wing aircraft. The design is chosen to be mechanically as simple as possible by minimizing the moving parts. This results in a easy to build, assemble and maintain design.

Chapter 4

Design Tool

The design had to be kept flexible because exact requirements can not be specified. A design tool was developed to accommodate this flexible design as it enables the user to define their own needs and could be generated without technical expertise.

The following sections explain how the design tool that was specially developed for the Dr.One concept, when combined with new production techniques for shaping materials, can be used to create accurately and economically body and wing shapes that result in sophisticated but inexpensive flying vehicles that are suitable for the tasks and conditions they which it will operate. In this chapter the general configuration for Dr.One is described followed by an explanation of the focus points of the design tool together with a description of the design process itself. A detailed elaboration of the sizing process is given in the chapters 5 - 8.

4.1 Main focus points

One principal focus was on the need to be able to design the aircraft around the needs of the payload. The design tool of Dr.One is a specially developed software application allowing rapid design for different payloads. No in depth aerospace knowledge is needed as these decisions are incorporated in the tool. The design tool was developed considering several main focus points, these are:

- Scalability
- Easy to use
- Modular approach
- Affordability

4.1.1 Scalability

The design tool scales the vehicle to the needs of the mission. The actual design is determined by the payload parameters, the range and the flight speed, which can be programmed in.

4.1.2 Easy to use

Ease of use is of paramount importance due to the environment in which it will be operated. Poor underdeveloped areas do not have available expertise so any technical equipment and processes must be autonomous with all technical decisions being made by the design tool itself. The design tool has an easy to use Graphic User Interface (GUI), which allows the user to rapidly create a new design and is not dependent on in-depth knowledge or expertise. All technical decisions are automatically made by the design tool.

4.1.3 Modular Approach

The program has a modular format. So when there is a wish to introduce a new or improved estimation method, technology or material, it can be easily imported into the design tool. The program can be expanded and adapted to include new technology such as solar panels.

4.1.4 Affordability

The design allows the use of off-the-shelf equipment instead of customized products. Low cost and widely available materials can be transformed into wings and fuselages by using 3D milling and hot-wire cutting. Due to (semi)-mass production the prices of electronic devices and electric motors has dropped significantly. The design tool allows the user to select an off-the-shelf motor around which the Dr.One can be designed.

4.2 Design methodology

The design methodology aims to realize a design using the configuration described in section 3.4 that optimizes performance for a chosen payload. It consists of four sequential parts and is schematically illustrated in figure 4.1.

- Body sizing
- Wing sizing
- Motor selection
- Propeller selection

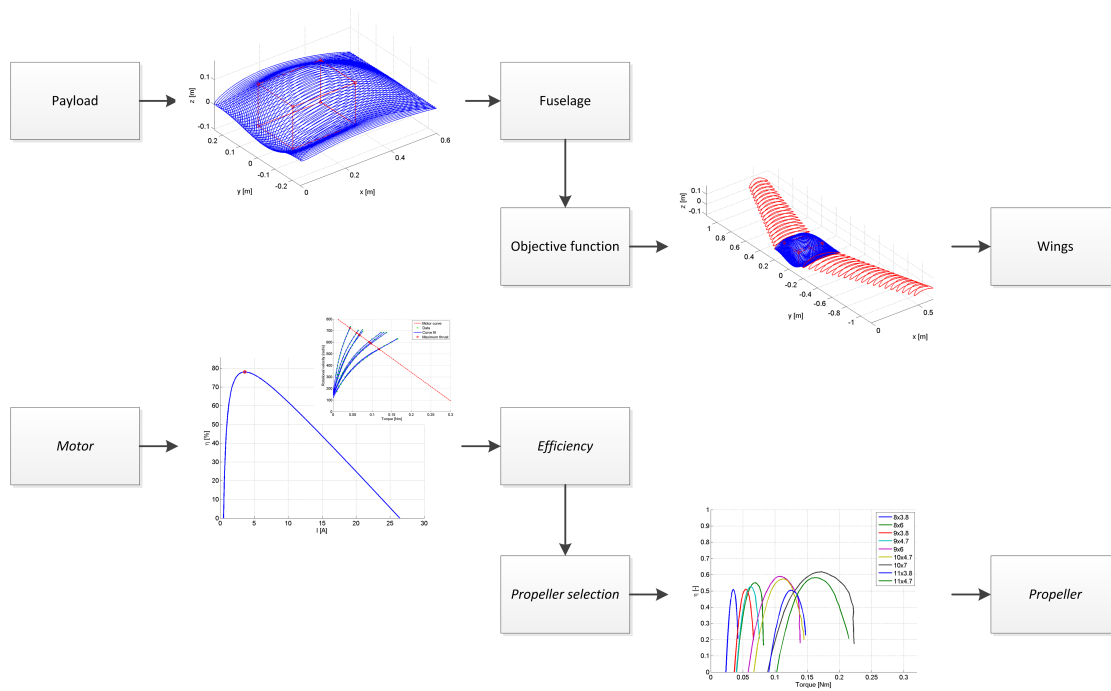


Figure 4.1: Design methodology

The options the user chooses determines the path of the optimization. This is given are schematically given in figure 4.2.

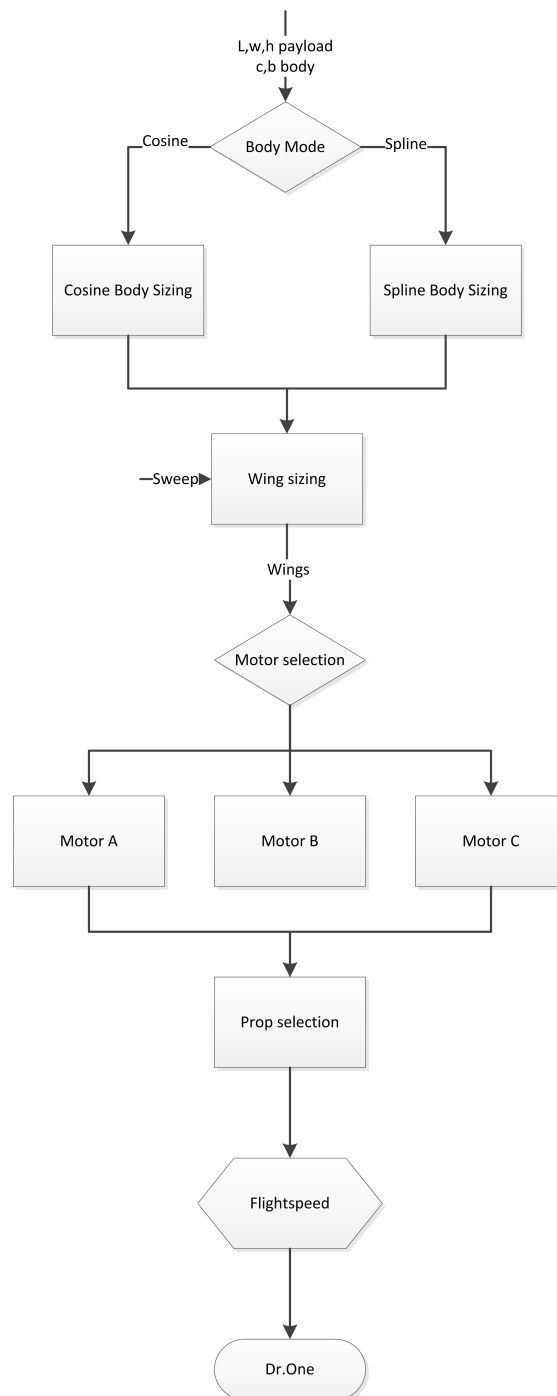


Figure 4.2: Design tool flow chart

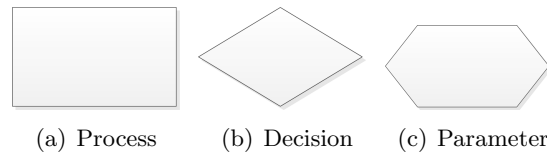


Figure 4.3: Meaning of icons

In figure 4.3 the symbols are explained. Figure 4.3(a) is a process, figure 4.3(b) is a decision that has to be made from a list and figure 4.3(c) means a numerical value can be inserted.

4.2.1 Payload

A detailed description of how the desired shape is achieved is shown in chapter 4. The strength and clear advantages of using the Dr.One design tool is that, contrary to traditional approaches to plane design, the plane does not restrict the capacity of the payload. Using this design tool the plane can be optimally designed around the needs of the payload itself. The design process starts by defining the payload in terms of dimensions and weight. The desired dimensions of the body are inserted after which the body can be sized as can seen in figure 4.4. Different sizing shapes can be chosen, a cosine fit and a spline fit are implemented in the tool, new fit functions can easily be added to the tool. A detailed description of how the desired shape is achieved is shown in chapter 5.

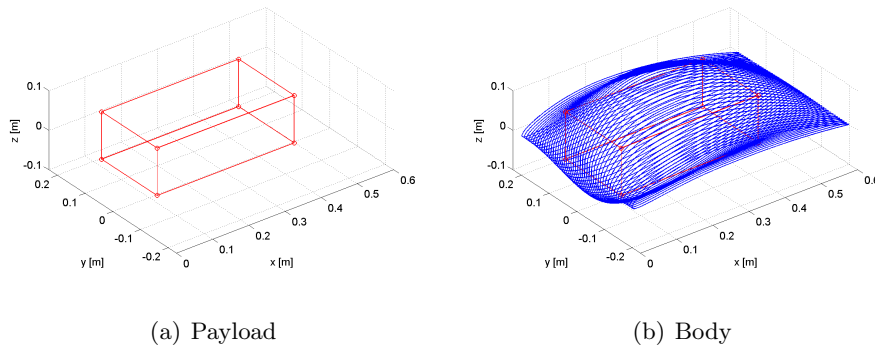


Figure 4.4: Body design

4.2.2 Wing sizing

The wing is parameterized using design variables see section 6.2. The wing is optimized for range where the objective function minimum drag is minimized. When the shape is determined all necessary parameters are then calculated. These consist of drag coefficient and weight estimation. More on the objective function and detailed elaboration on the wing sizing can be found in chapter 6.

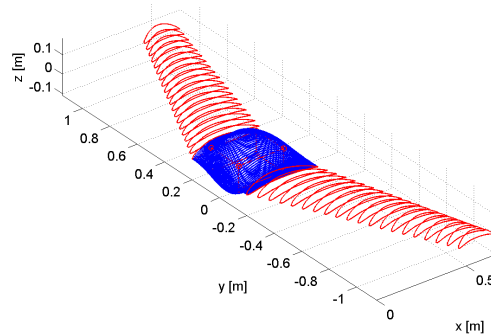


Figure 4.5: Wing design

4.2.3 Motor selection

When the weight and drag are known the propulsion can be selected. The static thrust delivered by all four motors has to exceed the total weight of Dr.One as the motor and propeller combination has to have a capacity for vertical take-off. More on how maximum static thrust is determined can be found in section 8.3.

4.2.4 Propeller selection

The performance of Dr.One is heavily influenced by the characteristics of the motor and propeller combination. Therefore both need to be known. Full explanation on obtaining the motor characteristics can be found in chapter 7 and more on the propeller characteristics can be found in chapter 8.

Range

The design tool matches the thrust needed with each propeller and the selected motor. Then it selects the propeller which draws the least amount of current.

4.3 Production

Making use of new technology such as the hot-wire cutter, 3D Milling and 3D printing techniques allows for inexpensive material such as insulation panels to be transformed into an advanced aircraft shape.

4.3.1 Body

The body is milled using a 3D-milling machine. The top and bottom sections are manufactured as separate parts. This way the inside can be milled out to create space for

the payload and electronic systems.

4.3.2 Wings

The wings are cut with a hot-wire wing cutter. More information can be found in section 6.4. The dimensions calculated in the optimization process can be directly programmed into the machine.

4.4 Conclusion

This design tool allows for a rapid design of a Dr.One around the requirements of a given payload. It sizes the body and wings, optimizing them for chosen performance characteristics and then selects the best propeller match from a list so as to obtain optimum performance. The design can be produced immediately out of insulation panels using a hot-wire cutter and a 3D milling machine.

Its modular approach allows it to be easily improved, upgraded, developed and new technology added.

The following chapters will elaborate the different sequential parts of the design tool.

Chapter 5

Body Sizing

The first step in the design tool is to size the body according to the size of the payload. Based on the length, width and height of the payload the Dr. One design tool sizes the body. To create a 3D body, the payload has to be fitted in two planes, the side and the front. The nose can be modified to reduce the the drag coefficient. This chapter will explain all the steps in the process of creating the 3D body.

5.1 Side-plane

The side-plane of the body is based on a NACA airfoil shape. The thickness of the airfoil can be varied until the dimensions of the payload fit in the body. The payload length and height are the inputs. The shape is based on a 4 digit NACA airfoil cambered airfoil. The definition of the equation can be found in Appendix D.

It calculates the position of the maximum thickness of the airfoil and draws the length of the payload from the upper curve to the lower curve. Then it starts expanding longitudinally in both directions until the required payload specifications are met. Side-plane designs for various dimensions of payloads can be seen in figure 5.1.

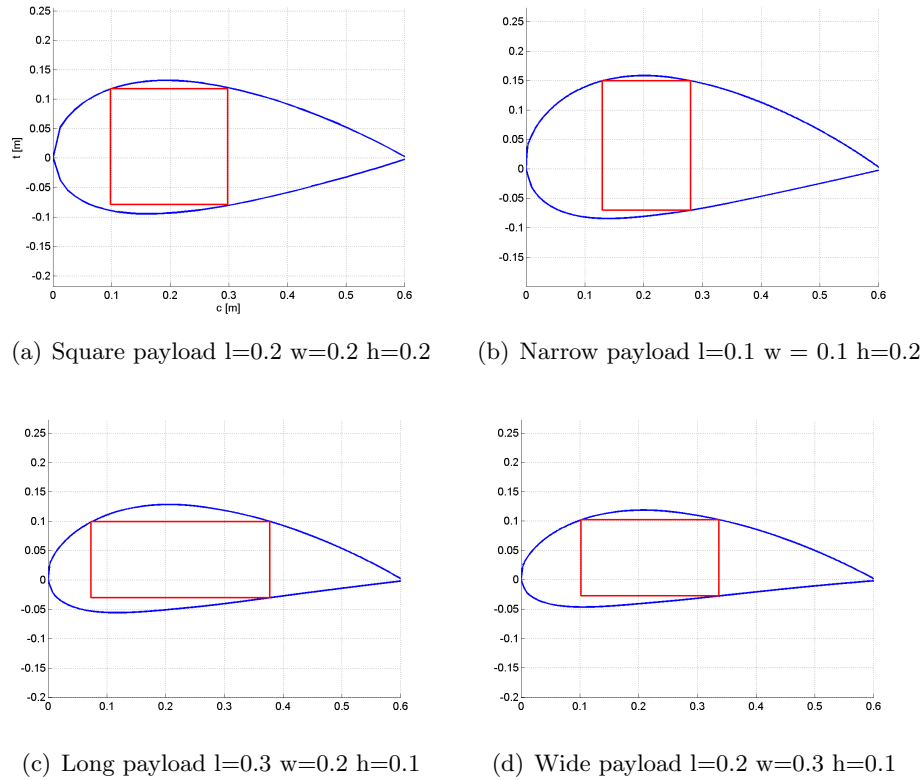


Figure 5.1: Side view of body design generation for different payload dimensions

5.2 Front-plane

The second step is the sizing in the lateral direction. Different shapes can be chosen, a cosine fit and a spline fit are implemented in the model, but more fit functions can easily be added. The input parameters are governed by the payload width and payload height, desired length and the width of the body.

5.2.1 Cosine fit

The cosine fit uses the following expression:

$$y_i = A \cos \left(\frac{c_b}{\pi} \left(t_b + \frac{\pi}{c_b} \right) \right) \quad (5.1)$$

$$c_b = \frac{b_f}{2\pi} \quad (5.2)$$

- A = amplitude of the cosine function
- c_b = resizing coefficient for the desired width of the body

- b_f = width of the body
- c_b = width vector

The amplitude is increased until it can accommodate the payload.

5.2.2 Spline fit

The spline fit utilizes four critical points, starting point at the left side of the body and right side of the body and the corners of the payload.

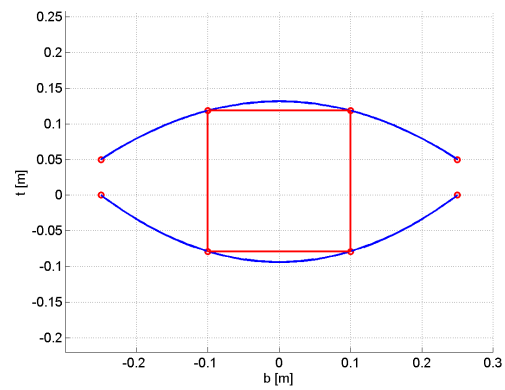


Figure 5.2: Spline fit

Front-plane designs for various payloads are shown in figure 5.3.

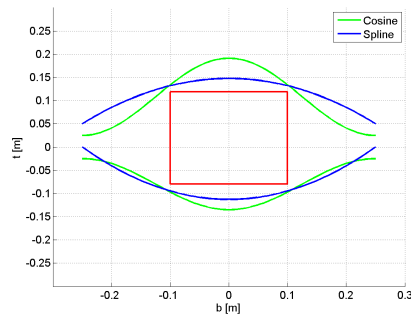
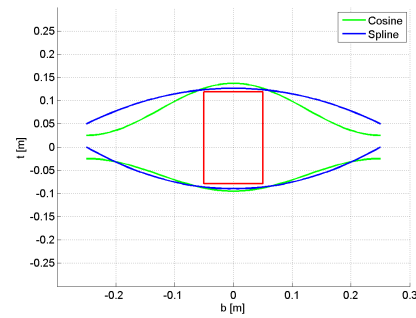
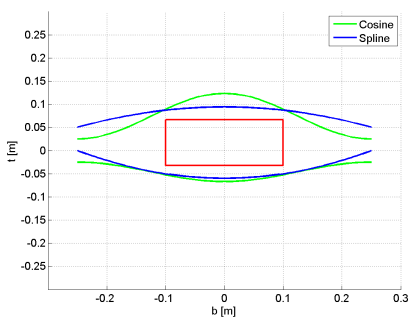
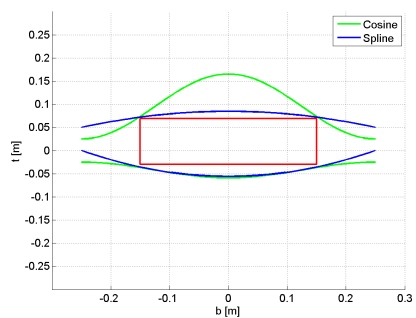
(a) Square payload $l=0.2$ $w=0.2$ $h=0.2$ (b) Narrow payload $l=0.2$ $w = 0.1$ $h=0.2$ (c) Long payload $l=0.3$ $w=0.2$ $h=0.1$ (d) Wide payload $l=0.2$ $w=0.3$ $h=0.1$

Figure 5.3: Front view of body design generation for different payload dimensions using a cosine fit and a spline fit function

5.2.3 Comparison

For weight minimization, the cosine function is better for payloads with a low height and width than the spline function as can be seen in figure 5.3(b). When the payload width becomes larger the spline function fits more efficiently as can be seen in figure 5.3(d).

5.3 3D-Body

Combining the side-plane and the front-plane creates a 3D shape. The airfoil shapes are plotted as ribs in an aircraft structure. The results for various payload dimensions can be seen in figure 5.4.

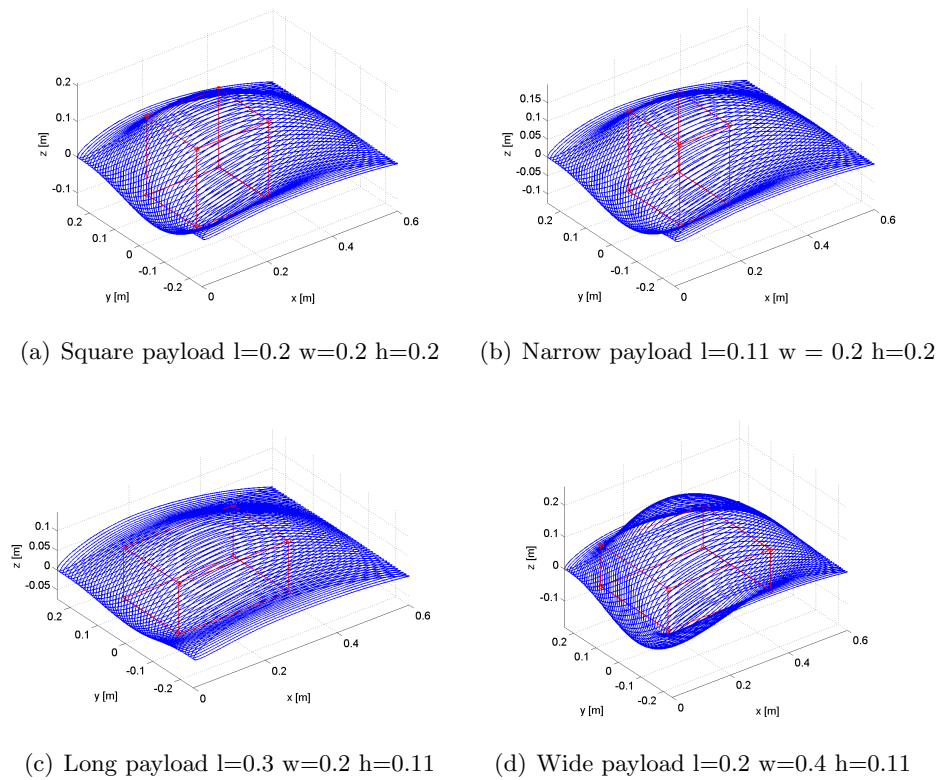


Figure 5.4: Body design generation for different payload dimensions

5.4 Nose

In the design tool the shape of the nose can be modified to decrease the drag coefficient. The modification of the nose is expressed in the variable dc which refers to the extra length added to the chord at the tip of the nose. Increasing this value changes the shape of the body which can be seen in figure 5.5.

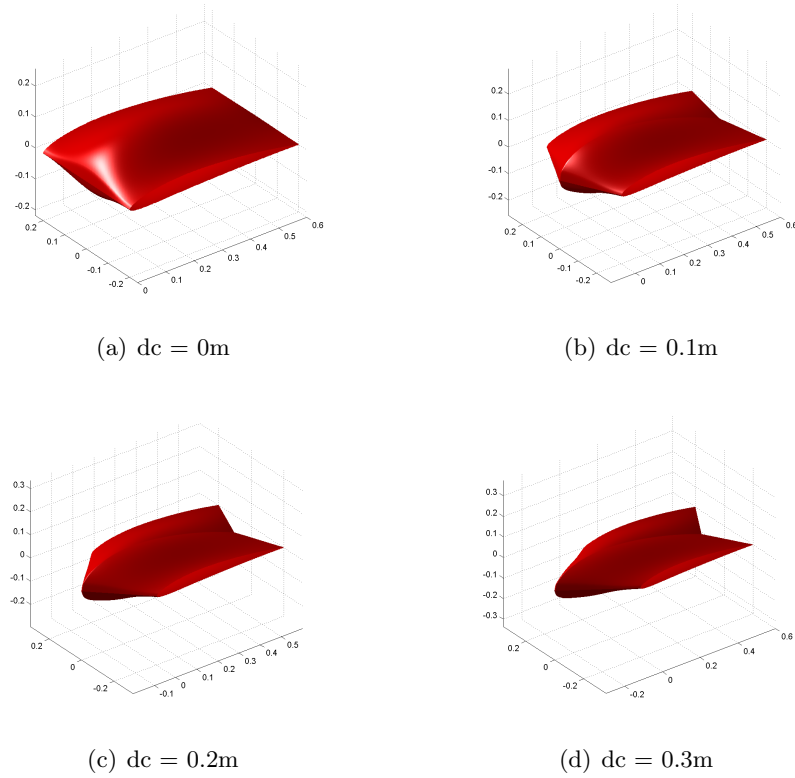


Figure 5.5: Adding the nose onto the body design

Moreover it could result in a reduction of the volume of the body as can be seen in figure 5.6.

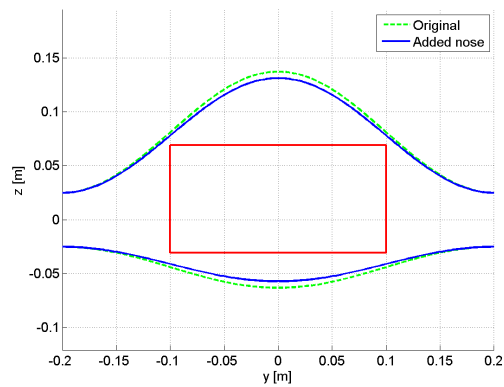


Figure 5.6: Body shaping side with added nose of $dc = 0.1m$

5.5 Body parameters

Once the body shape is defined the drag coefficient (C_{d_f}) and weight are calculated. The drag coefficient is estimated using the formula [11]:

$$C_{d_f} = C_f f_{LD} f_M S_b \quad (5.3)$$

- C_f = Skin friction coefficient
- f_{LD} = Fuselage length ratio coefficient
- f_M = Mach number coefficient
- S_b = Wetted area of the body

For derivation see appendix H.1. The volume of the shape of the body is approximated by numerical integration. For the actual volume of the body, the volume of the payload has to be subtracted. The weight is obtained by multiplying this volume with the density of the material used for the body.

5.6 Manufacturing the body

To create a hollow body, the body is milled in two halves that are joined together. Software called PyCam allows the exported shape to be milled by a 3D milling machine. Detailed elaboration on this process can be found in appendix I.

5.7 Conclusion

This chapter explained the body sizing which is part of the design tool for Dr.One. The body fits the needs of the payload in two planes, the side-plane and front-plane which are combined into a 3D body. The side-plane uses a NACA airfoil varying the thickness, whereas the front-plane uses a cosine or spline function. Furthermore the weight and drag coefficient estimation methods are shown. The body will be manufactured using a 3D milling machine.

Chapter 6

Wing sizing

This section covers wing sizing done by the design tool. The side-plane of the wing is shaped as an airfoil. The other dimensions are determined by the top view. The design is optimized for range by minimizing the minimum drag objective function. Finally the manufacturing is explained.

6.1 Airfoil

To maintain longitudinal stability the aircraft needs a zero or positive pitching moment. Conventional aircraft have a tail to compensate for the negative pitching moment which ensures longitudinal stability. Flying wings do not have a tail, therefore a special type of airfoil was selected for the design of Dr.One to maintain longitudinal stability. The MH60 designed by Martin Hepperle has a slightly positive pitching moment and is shown in figure 6.1

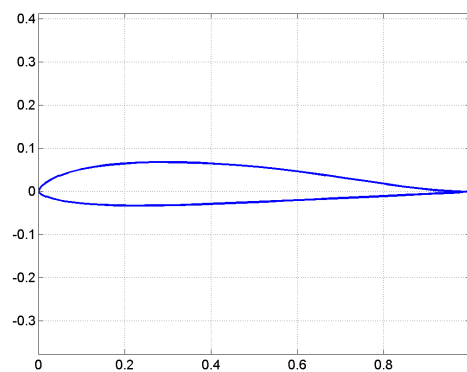


Figure 6.1: MH-60 airfoil

6.2 Parameterization wing

The wing was parameterized as shown in figure 6.2.

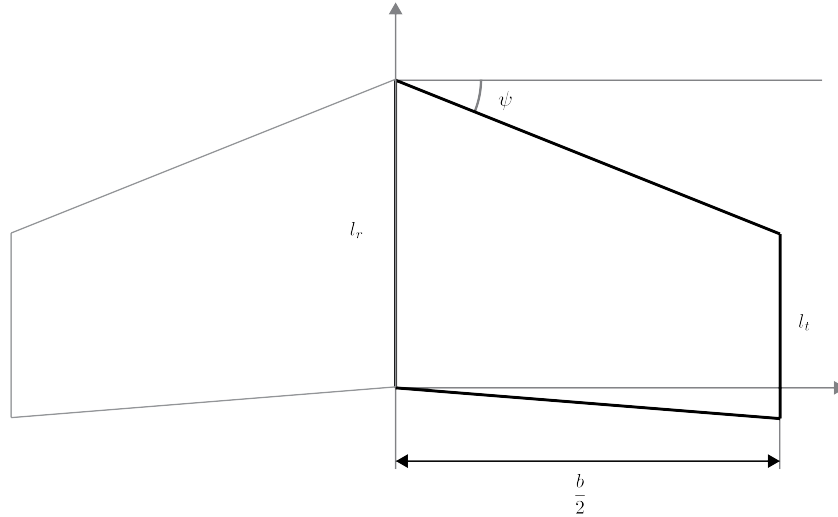


Figure 6.2: Parameterization of the wing

- l_r = chord at the root of the wing
- l_t = chord at trailing edge of the wing
- b = wingspan
- ψ = sweep angle

The first three parameters will be used as design variables and will be optimized. The sweep is used for longitudinal stability.

6.3 Objective function

The objective function is derived from the equilibrium at cruise from the flight condition. The objective function is expressed as a function of the design variables. The optimization tool establishes the values of the variables where the objective function is maximum.

6.3.1 Flight condition

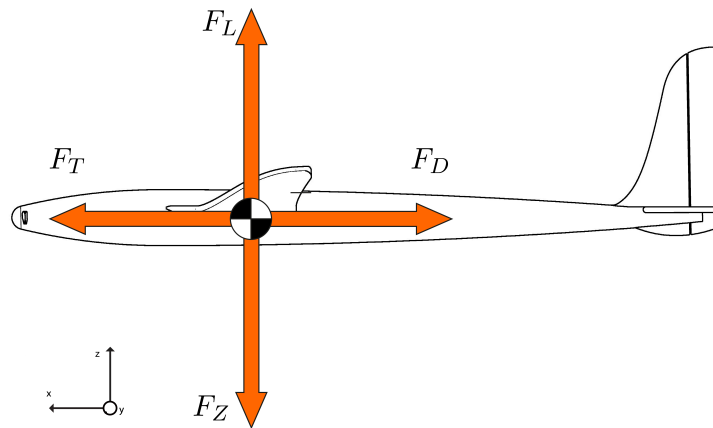


Figure 6.3: Flight condition

The flight condition at cruise is defined as can be seen in figure 6.3, where the angle of attack is zero (ie the plane is flying horizontally). This gives the equilibrium equations:

$$\begin{aligned} \sum F_Z : L &= W \\ \sum F_X : F_T &= D \end{aligned} \tag{6.1}$$

It can be seen that the flight condition consists of these four components:

- L = lift force [N]
- D = drag force [N]

- L = total weight of the aircraft [N]
- F_t = total thrust of the propulsion

Which will be discussed next.

6.3.2 Lift and drag forces

The lift is determined by the expressions [12]:

$$\begin{aligned} L &= \frac{1}{2}\rho V^2 S C_l \\ D &= \frac{1}{2}\rho V^2 S C_d \end{aligned} \quad (6.2)$$

- C_l = lift coefficient [-]
- C_d = drag coefficient [-]
- V = flight speed [m/s]
- S = wing area [m²]
- ρ = density of air [$\frac{\text{kg}}{\text{m}^3}$]

Lift coefficient

Hence the lift coefficient can be determined from the weight estimation:

$$C_l = \frac{W}{\frac{1}{2}\rho V^2 A} \quad (6.3)$$

Drag coefficient

The drag consist of two parts, the induced drag and the pressure drag.

$$C_d = C_{d_i} + C_{d_p} \quad (6.4)$$

The induced drag is expressed as:

$$C_{d_i} = \frac{C_l^2}{\pi A R e} \quad (6.5)$$

- AR = aspect ratio [-]
- e = Oswald factor [-]
- π = ratio of circumference of circle to its diameter [-]

The pressure drag is expressed as:

$$C_{d_p} = C_{d_0} + C_{d_1} C_l \quad (6.6)$$

- C_{d_0} = zero lift drag coefficient [-]
- C_{d_1} = induced drag coefficient [-]

6.3.3 Weight estimation

The weight is estimated using a weight estimation tool which is elaborated in H.0.3.

6.3.4 Maximum range

The maximum range is achieved at the point of minimum drag. Using the flight condition (6.1). Where the weight, W , of the aircraft is calculated with the weight estimation tool described in section H.0.3.

Combining all equations above gives the drag equations.

$$D(lr, lt, b) = \frac{1}{2} \rho V^2 A C_d(Cl(W(lr, lt, b))) \quad (6.7)$$

6.4 Production

The wings made are out of insulation panel and are produced with a hot wire cutter. The hot wire cutter uses the cross section profile at the root chord and at the tip chord. It follows the path of the airfoil profile and creates the wing.

6.5 Conclusion

This chapter derived the wing sizing for Dr.One using an objective function. This objective function was derived from the equilibrium equations during cruise flight. The maximum range is found at the minimum drag, which is found through optimization of the root chord and wing span. The wing is manufactured by using a hot wire cutter and insulation panels.

Chapter 7

Motor selection

The performance of Dr.One heavily depends on the motor and propeller combination. To obtain optimum performance, the performance characteristics of the motor have to be known. This can be acquired by contacting the manufacturer. As it is not always possible to obtain specific performance data from an engine manufacturer two other methods are shown to obtain the data; an online tool and a developed method to determine the performance characteristics experimentally, using only widely available equipment.

7.1 Motor characteristics

In this section the performance of an electric motor is analyzed using three different methods. The methods were applied to a motor selected in section 7.1.1. First the necessary characteristics were assessed step by step using test data acquired from the manufacturer to eventually construct the efficiency curve and determining the optimum point. Then the same curves were obtained using a theoretical tool eCalc. Finally a general method was developed to determine the optimum point of an electric motor experimentally. This method consists of a series of tests done to determine the same characteristics as from the acquired data of the manufacturer. The method was applied to the selected motor and the results were analyzed and compared with those of the other tests.

7.1.1 Selected motor

The ROXXY 2827-34 was selected for the initial design of Dr.One and is shown in figure 7.1. The motor provides propulsion to the Mikro Quad Kopter. The motor was selected for its power and rotation velocities which are in the range of other equipment used for the analysis such as the torque meter.

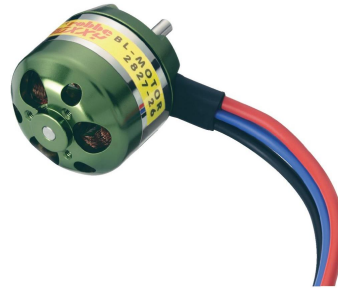


Figure 7.1: Robbe Roxy 2827-34 Outrunner [1]

7.1.2 Performance characteristics using test data from manufacturer

To be able to construct the efficiency curve two linear relations were determined. These relations are the drawn current and the rotational velocity (ω) as a function of the applied torque (Q). The manufacturer was contacted and they released their test results which are shown in figures 7.2. The measured data can be found in appendix G.1

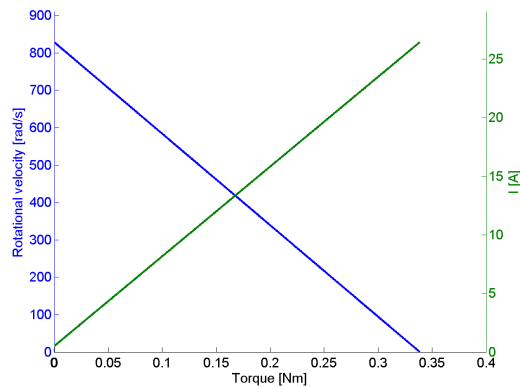


Figure 7.2: Results Robbe 2827 torque vs ω and current from manufacturer

From these two linear relations the power curves were determined. The power curves consist of the power in, P_{elec} and the power out, P_{mech} which are determined by the following expressions:

$$P_{elec} = VI \quad (7.1)$$

$$P_{mech} = \omega T \quad (7.2)$$

- V = Voltage [V] not to be confused with flight speed

- I = current [A]

The results are shown in figure 7.3.

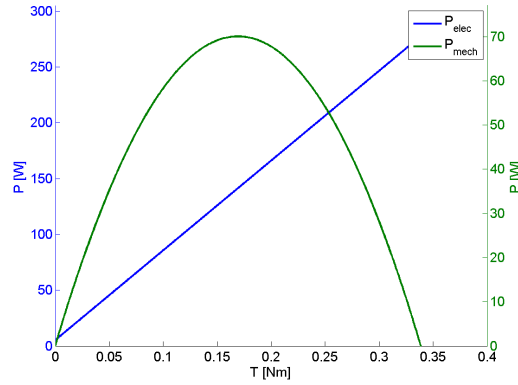


Figure 7.3: Results Robbe 2827 torque vs P_{elec} and P_{mech} from manufacturer

Finally the efficiency (η) curve was constructed by dividing the power in by the power out.

$$\eta = \frac{P_{in}}{P_{out}} = \frac{P_{elec}}{P_{mech}} \quad (7.3)$$

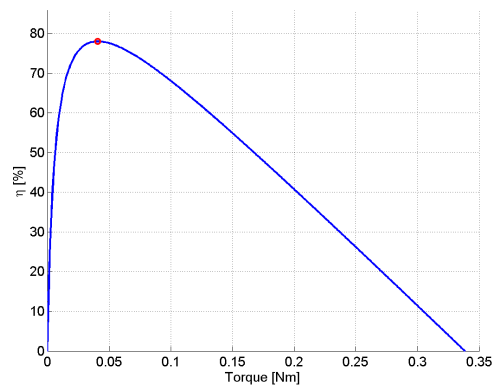


Figure 7.4: Results Robbe2827 torque vs η from manufacturer

Where it can be seen that the maximum efficiency is achieved at:

η	78.0	%
ω	728.4	rad/s
I	3.62	A
Q	0.041	Nm

Table 7.1: Parameters at maximum efficiency

7.1.3 Theoretical tool eCalc

The characteristics of an electric motor could also be obtained using a simulation tool called eCalc. This tool allows for quick analysis of electric motors and is based on a theoretical method. The use of eCalc eliminates the need to acquire test data from the manufacturer. The results of the model for the selected motor are shown in figure 7.5

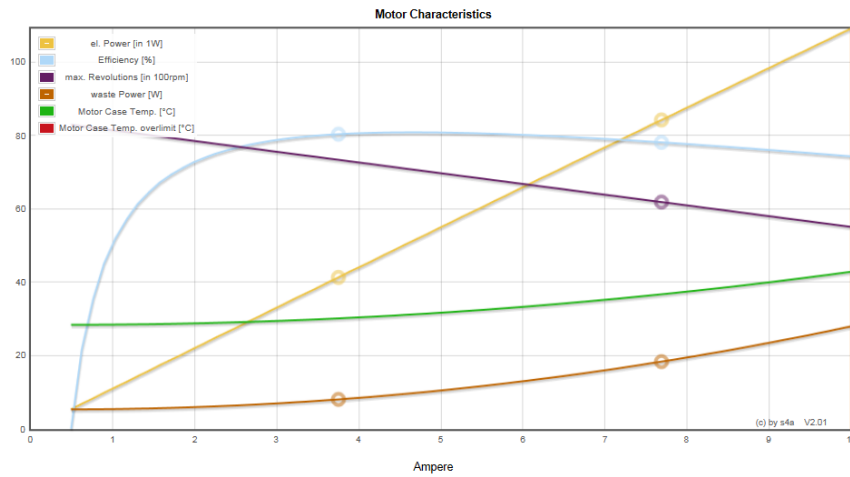


Figure 7.5: eCalc motor characteristics of 2728-34

	Manu	eCalc	
η	78.0	80.9	%
ω	728	635	rad/s
I	3.62	4.53	A
Q	0.041	0.056	Nm

Table 7.2: Parameters at maximum efficiency

7.1.4 Test results

For when there is a need to verify motor characteristics and there is no reliable test data available, an independent, experimental method was created. Considering the conditions it is likely to be used in, a method that required no advanced equipment was devised.

Widely available multimeters, copper wire and a DC motor were sufficient to perform the experiment. Full elaboration on the test setup and the data points can be found in appendix G.2 and G.3 respectively.

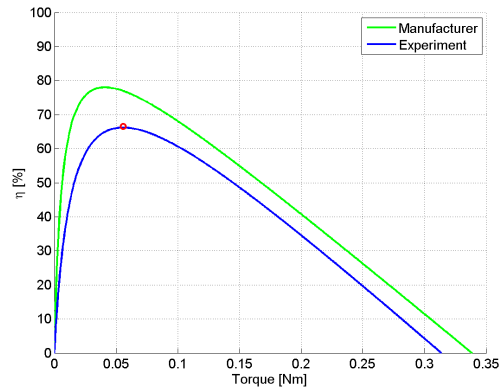


Figure 7.6: Results Robbe2827 torque vs η from test setup

The optimum point is at:

	Manu	eCalc	Exp	
η	78.0	80.9	66.2	%
ω	728	741	735	<i>rad/s</i>
I	3.62	4.53	5.17	A
Q	0.041	0.056	0.056	Nm

Table 7.3: Parameters at maximum efficiency

The rotational velocity at the optimum point is similar for all three methods ranging from 728 until 741 rad/s. The optimums found are in the same region, however the drawn current and efficiency at this point differ from method to method. An explanation for the difference in efficiency could be that a different motor driver was used. This driver might have had a different power consumption and resulting in a different drawn current. Furthermore difference in mechanical losses from the DC motor could contribute to the difference as would in theoretical tool where the modeled mechanical losses might be an approximation.

7.2 Conclusion

The motor characteristics of the selected motor Robbe Roxxy 2827-34 have been determined using three different methods. Using test data from the manufacturer, using an online tool eCalc and using an experimental setup. It can be concluded that the efficiency curves found by the three only differ slightly. Trusting the test data from the

manufacture would give the most accurate results in perfect conditions since they have used tools specifically designed for the purpose. The online tool is systematically too optimistic, but it could be a helpful initial guess. The experimental method provides more realistic but pessimistic results since other losses, such as the speed controller are also incorporated in the result.

7.2.1 Recommendations

For future experiments it is recommended to use a larger DC motor which can slow down the brush less motor more, preferably to a stop. This requires at least the same output power as the brush less motor. In this way a larger part of the spectrum could be covered improving the accuracy of the two linear relations. Even better would be to use a designated torque meter such as a magnetic transducer, which are more accurate but expensive.

Chapter 8

Propeller Performance

The propeller has a strong influence on the performance of the aircraft. Propellers are very sophisticated in terms of aerodynamics. However wind tunnel tests are available which provide accurate experimental data for available propellers [13]. The propellers characteristics are defined by different parameters, the thrust coefficient C_t the power coefficient C_p , the advance ratio J and the efficiency η . The derivation of the these coefficients can be found in appendix F.

For the purpose of Dr.One a small database of propellers was created and the characteristics were imported. A program was created which automatically reads the measured data from the text file and stores it into variables used in the design tool. New propellers can easily be added to the database. The data base consists of 9 propellers:



APC slow flyers

8x3.8

8x6

9x3.8

9x4.7

9x6

10x4.7

10x7

11x3.8

11x4.7

Figure 8.1 & Table 8.1: The selected propellers

First the propellers parameters were examined to understand the effects on the performance. Then the propellers are matched to the motor to obtain the total performance of the propulsion.

8.1 Propellers parameters effects on performance

The propeller's characteristics are defined with three parameters, the diameter d , the pitch β and the rotational velocity ω . First the effect of these parameters on the efficiency is examined respectively.

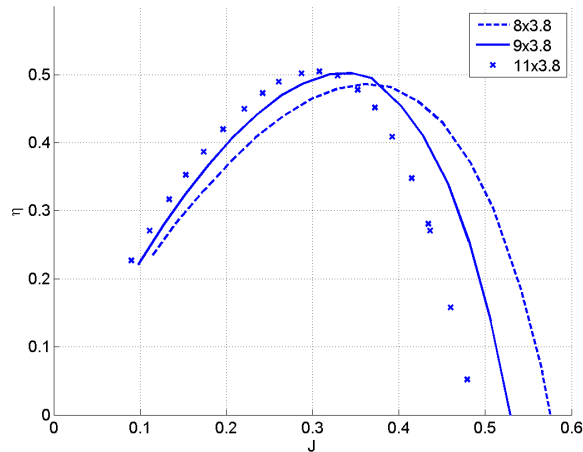


Figure 8.2: Effect of diameter of efficiency

The effect of the diameter is clearly visible in figure 8.2. The maximum efficiency is achieved at a lower advance ratio when the diameter increases. The efficiency increases slightly with increasing diameter.

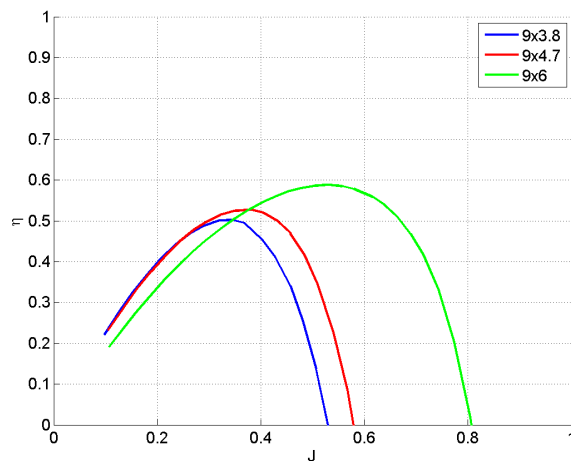


Figure 8.3: Effect of pitch of efficiency

Increasing pitch increases the advance ratio at maximum efficiency, furthermore it increases efficiency as well.

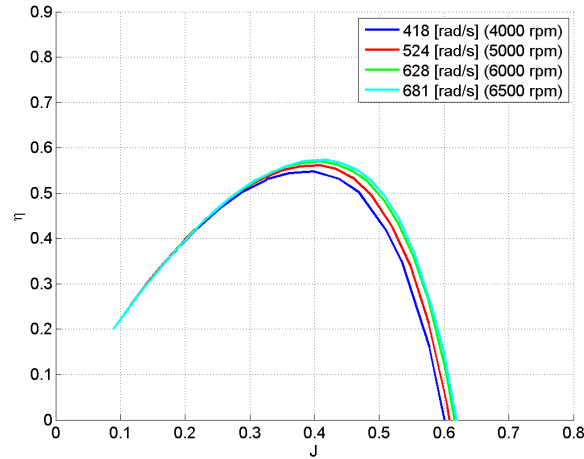
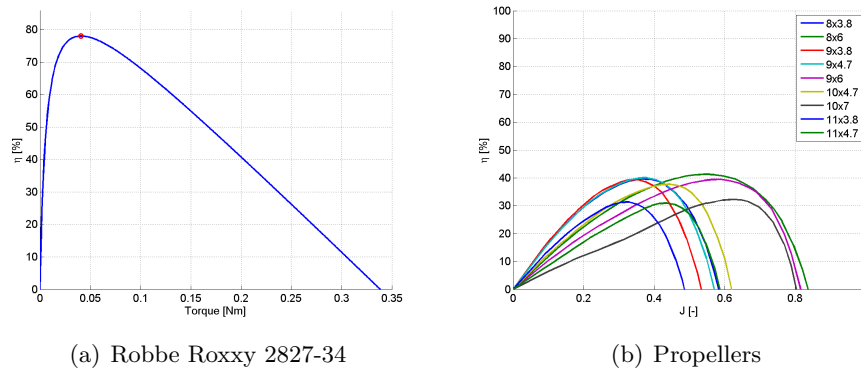


Figure 8.4: Effect of rotational velocity of efficiency, for the 10x4.7 slow flyer

The rotational velocity effects the efficiency only slightly. The according advance ratio increases with increasing rotational velocity. For further analysis the effect of the rotational velocity on the efficiency is omitted.

8.2 Motor and propeller matching

To determine the efficiency of the propulsion, the motor and the propeller performance have to be matched. This requires the efficiency curve of the motor and performance characteristics of the propeller described in section 8. The process is the same for each propeller and motor. The example of motor previously selected, the Robbe Roxxy 2728-34 was selected again. How to obtain the efficiency curve is elaborated in chapter 7.



(a) Robbe Roxxy 2827-34

(b) Propellers

Figure 8.5: Efficiency curves of the motor and propellers

This efficiency curve of the motor is at full throttle. It can be seen that the units on the x-axis are not the same. The motor uses torque whereas the propeller uses J , which is the advance ratio. To make this consistent the motor has to be matched to the propeller. Expressing ω in torque using the power coefficient and recapturing the relation of the ω and the torque from the motor see section 7 give the following expressions:

$$\begin{aligned}
 Q_{prop} &= \frac{C_p}{2\pi} \rho \omega^2 d^5 \\
 Q_m &= -a_\omega \omega + b_\omega
 \end{aligned}
 \tag{8.1}$$

- $-a_\omega$ and b_ω are coefficients of the linear relation ship see figure 7.2

Since the torque of the propeller has to match the torque of the motor, equations 8.1 can be solved for ω for each C_p . For one propeller this is shown in figure 8.6.

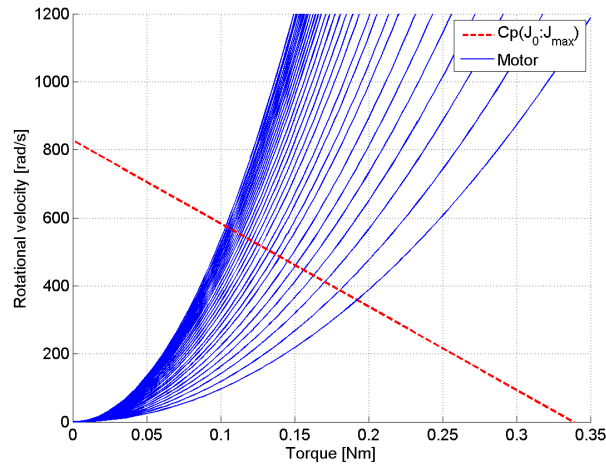
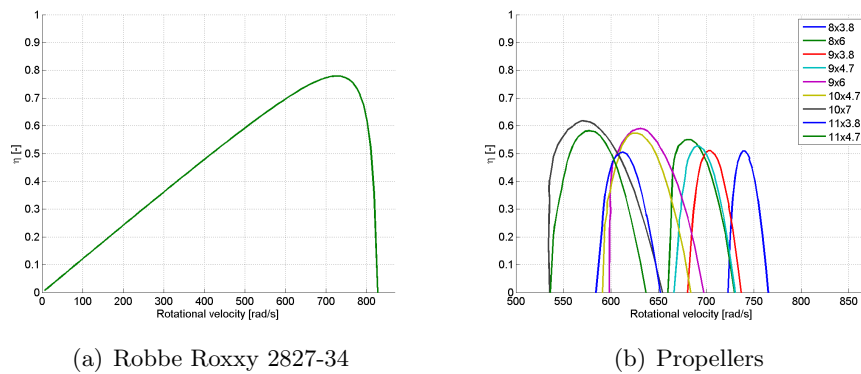


Figure 8.6: Rotational velocity (ω) matching for propeller and motor

After the propeller’s torque and the motor’s torque were matched the efficiency curves were made consistent:



(a) Robbe Roxxy 2827-34

(b) Propellers

Figure 8.7: Efficiency curves

The total efficiency is obtained by multiplication of the efficiency of the motor with the propeller.

$$\eta_{tot} = \eta_m \eta_p \tag{8.2}$$

The efficiency curves are multiplied with the efficiency curve of the motor to obtain the total efficiency.

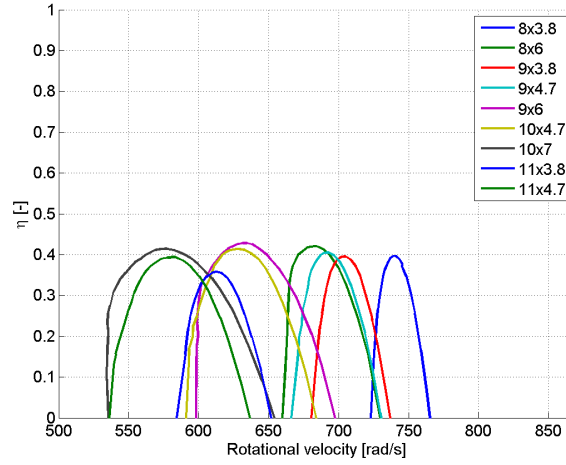


Figure 8.8: Total efficiency curves as a function of torque

It can be seen that the total efficiency is similar for the smaller propellers and decreases for the bigger propellers. Hence for each prop the characteristics at the maximum efficiency point are calculated and shown in table 8.2. This includes the thrust (T) which is calculated expression (8.3) [13].

$$T = C_T \rho \omega^2 d^4 \quad (8.3)$$

prop	η_p [%]	η_m [%]	η_{tot} [%]	Q [Nm]	w [rad/s]	T [N]	I [A]
8x3.8	51	78	40	0.037	739	1.59	3.30
8x6	55	76	42	0.059	683	1.84	5.04
9x3.8	51	78	40	0.050	705	2.01	4.35
9x4.7	53	77	41	0.055	693	2.11	4.73
9x6	59	73	43	0.079	635	2.26	6.56
10x4.7	57	72	41	0.082	628	2.76	6.77
10x7	61	67	41	0.102	577	2.72	8.35
11x3.8	51	71	36	0.088	613	3.26	7.25
11x4.7	58	68	39	0.100	583	3.13	8.17

Table 8.2: Propeller comparison

It can be seen that the larger propellers give more thrust at maximum power of the engine than the smaller propellers. The maximum is obtained with a 11x3.8 prop for the Robbe Roxxy 2827-34 motor. For the larger propellers increasing pitch negatively influences the performance, increasing the drawn power but decreasing the thrust slightly.

8.3 Static Thrust

The static thrust is the thrust which is generated when Dr.One is not moving. The static thrust needs to exceed the total weight of Dr.One by some margin. The static thrust is determined by matching the maximum torque of the motor and the torque required by the propeller.

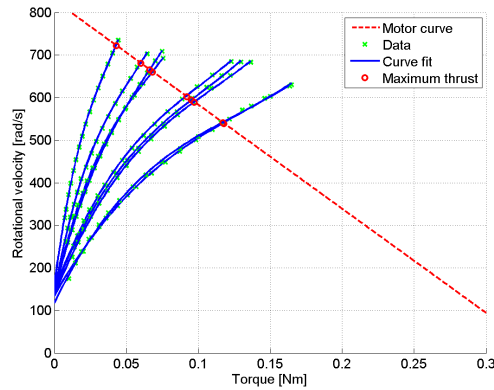


Figure 8.9: Rotational velocity vs Torque for the propeller and Robbe Roxxy 2827-34

The static thrust can be calculated with the according thrust coefficient C_t .

$$T = C_t \rho \omega^2 d^4 \quad (8.4)$$

which results in the following maximum static thrusts:

prop	T [g]	T_{tot} [kg]
8x3.8	281	1.12
8x6	235	0.94
9x3.8	400	1.60
9x4.7	382	1.53
9x6	315	1.26
10x4.7	465	1.86
10x7	385	1.54
11x3.8	673	2.69
11x4.7	568	2.27

Table 8.3: Static thrust with Robbe Roxxy 2827-34

The static thrust of a more powerful motor is also determined and shown in appendix H. The motor curve shifts upwards resulting in a higher static thrust. Dr.One has four motor hence the total thrust is four times the thrust of an individual motor. For the

maximum take-off weight for a design of Dr. One a safety margin has to be considered which is now set to 10% in the design tool.

8.4 Conclusion

In this chapter the performance of propellers was explained. The propeller parameters effects on its performance was shown. The propeller was matched to a motor by matching the torque. From this the efficiency curve of the total propulsion system was determined. The performance at maximum efficiency of the different propellers were compared. In the last section the static thrust is determined, which is a critical factor for the maximum take-off weight.

Chapter 9

Example Design

In this chapter an example design was worked out using the design tool.

This Dr.One will was optimized for range carrying a payload of 0.5kg. A chord of 0.4m and a body span of 0.4m was chosen.

The dimension of the payload were defined and shown in table 9.1

Payload		
l_l	0.2	m
l_w	0.2	m
l_h	0.2	m
w	0.5	kg

Table 9.1: Payload definition

The design tool allows for different payload fitting functions. The cosine fit results a fuselage weight of 0.638kg and the spline fit results in a fuselage weight of 0.550kg, which is a reduction of 13.8%. Adding a nose of 0.1m reduces the drag coefficient, from 0.0303 to 0.0161 which is a reduction of 46.9%.

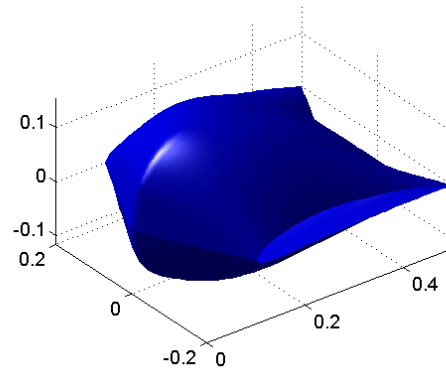


Figure 9.1: 3D body

The parameters of the fuselage are:

Fuselage		
S_f	0.44	m^2
b_f	0.40	m
w	0.55	kg
C_{d_f}	0.0161	-

Table 9.2: Fuselage parameters

Using the optimization tool and optimizing for range gives the dimensions of the wing, which are plotted in figure 9.2 and given in table 9.3.

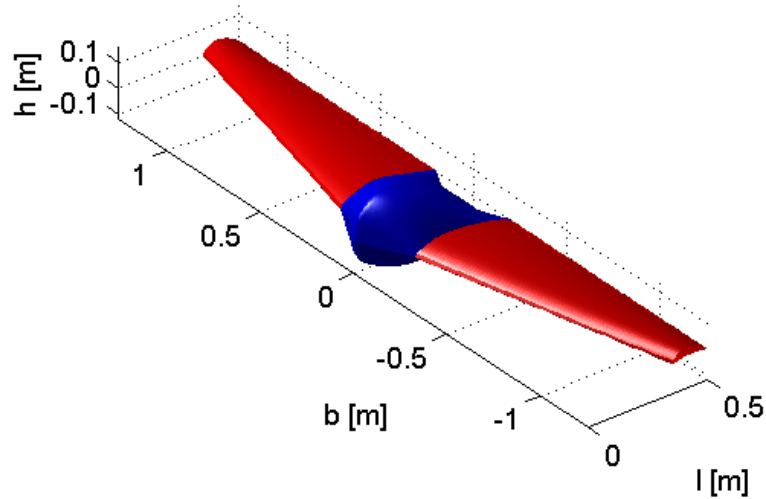


Figure 9.2: Dr.One design

Wing		
l_t	0.15	m^2
b_w	2.13	m
V	20.94	m/s
w	3.81	kg

Table 9.3: Wing parameters

This results in a total weight of the design of 3.37kg. It can be seen that this exceeds the maximum take-off weight produced with the Robbe Roxxy 2827-34 see table 8.3. The design tool will give a notification that the static thrust is not sufficient and a more powerful engine has to be selected. The second motor imported in the design tool is the MK3638. Determining the static thrust is done in the same way as with the Robby Roxxy 2827-34 and can be found in appendix H.

In the final step the propeller was selected. The design tool eliminates the propeller motor combination which do not provide enough static thrust. In this case the 8x3.8 propeller is eliminated. From the remaining propellers the thrust is matched to the drag using the windtunnel data and varying the rotational velocity ω . For each propeller the drawn current for this thrust is calculated and the minimum is selected. In this case the result is the 9x3.8 propeller. The range of this design using a 10Ah battery is 54km flying at the optimum speed of 20.94 m/s.

9.1 Improving the range

For future improvement of the range of this design following options can be considered:

- Solar panels: mounting solar panels on the wings could improve the range. The weight and efficiency is believed to improve drastically with new types of solar cells being developed.
- Powering down motors during cruise: During horizontal flight the aircraft needs significantly less thrust to generate the necessary amount of lift than during hover. For example 2 motors can be used for the propulsion whether the other 2 only have to function as controls. Significantly reducing the power consumption.

Chapter 10

Dynamic Model

In order to design the controls a computer model was used to simulate the dynamics of the aircraft. The model was created using rigid body dynamics [14] [15]. First the state vector and its derivatives were defined, before presenting a more advanced model [16] in which the aerodynamics of the wing and rotors were incorporated.

Notation

For this section the following notations are used:

- regular (ϕ) for a scalar value
- bold (\mathbf{v}) for a vector
- open face (\mathbb{R}_I^B) for a matrix or tensor

10.1 Rigid body dynamics

Dr. One is modeled as a rigid body which has six degrees of freedom, three translations and three rotations. The state vector of the aircraft consists of the velocities and accelerations of these six degrees of freedom and its attitude. The attitude of the aircraft is expressed in Euler angles, ϕ , θ , ψ . and their corresponding velocities, p , q , r .

The equilibrium equations of the x-z plane are shown below.

$$\begin{aligned} \sum F_Z : L &= \cos \alpha W \\ \sum F_X : \sum_i^4 F_{T_i} &= D + \sin \alpha W \end{aligned} \quad (10.1)$$

- L = lift force [N]
- D = drag force [N]
- α = angle of attack [deg]

- W = total weight of the aircraft [N]
- F_{T_i} = thrust of a single motor [N]

The lift and drag force are given using 10.3 where the velocity is a vector \mathbf{v} :

$$\mathbf{v} = \begin{bmatrix} v_x \\ v_y \\ v_z \end{bmatrix} \quad (10.2)$$

$$\begin{aligned} L &= \frac{1}{2} \rho C_l A (\mathbf{v} \cdot \mathbf{v}) \\ D &= \frac{1}{2} \rho C_d A (\mathbf{v} \cdot \mathbf{v}) \end{aligned} \quad (10.3)$$

In the body fixed frame the lift is only generated by the x-component of the velocity vector, v_x .

hence the lift and drag equations become:

$$\begin{aligned} L &= \frac{1}{2} \rho C_l A v_x^2 \\ D &= \frac{1}{2} \rho C_d A v_x^2 \end{aligned} \quad (10.4)$$

The thrust forces in the horizontal flight mode are only in the x-direction of the body fixed frame:

$$\mathbf{F}_{T_i} = \begin{bmatrix} F_{t_i} \\ 0 \\ 0 \end{bmatrix} \quad (10.5)$$

The gravitational force is pointed in the negative z-direction of the inertial frame, hence a transformation matrix is used to transform it into the body-fixed frame.

$$\mathbf{W} = \mathbb{R}_I^B \begin{bmatrix} F_{t_i} \\ 0 \\ 0 \end{bmatrix} \quad (10.6)$$

Where the rotation matrix is inverse of the rotation matrix from [17].

Using Newton's second law:

$$\sum \mathbf{F} = \mathbf{M} \ddot{\mathbf{x}} \quad (10.7)$$

$$\ddot{\mathbf{x}} = \sum \mathbf{F}(\mathbf{M})^{-1} \quad (10.8)$$

The moment $\mathbb{M}_{\mathbb{G}}$ is calculated using:

$$\mathbb{M}_{\mathbb{G}} = \sum_i^4 \mathbf{r}_i \times \mathbf{F}_{\mathbf{T}_i} \quad (10.9)$$

where \mathbf{r}_i is the vector from an individual element to the cog of the aircraft and i is the corresponding index.

Transforming the second order differential equations into a set of first order:

$$\ddot{\mathbf{x}} = \dot{\mathbf{v}} \quad (10.10)$$

$$\dot{\mathbf{x}} = \mathbf{v} \quad (10.11)$$

Euler angles suffer from singularity at angles close to 90 degrees, therefore for the simulation calculations, quaternions, also referred to as Newton Parameters, are used for the attitude. After the simulation the quaternions are transformed back into Euler angles for physical interpretation. Using quaternions gives a vector (\mathbf{q}) with four elements (λ).

$$\mathbf{q} = [\lambda_1 \quad \lambda_2 \quad \lambda_3 \quad \lambda_4] \quad (10.12)$$

Combining the rigid body dynamics in a state vector:

$$\mathbf{Y}_{\text{rb}} = \begin{bmatrix} \mathbf{x} \\ \mathbf{q} \\ \mathbf{v} \\ \omega \end{bmatrix} \quad (10.13)$$

The system of differential equations is set up:

$$\dot{\mathbf{Y}}_{\text{rb}} = \begin{bmatrix} \dot{\mathbf{x}} \\ \dot{\mathbf{q}} \\ \dot{\mathbf{v}} \\ \dot{\omega} \end{bmatrix} \quad (10.14)$$

where:

$$\dot{\mathbf{x}} = \mathbf{v} \quad (10.15)$$

$$\dot{\mathbf{q}} = \frac{1}{2} \begin{bmatrix} \lambda_0 & -\lambda_1 & -\lambda_2 & -\lambda_3 \\ \lambda_1 & \lambda_0 & -\lambda_3 & \lambda_2 \\ \lambda_2 & \lambda_3 & \lambda_0 & -\lambda_1 \\ \lambda_3 & -\lambda_2 & \lambda_1 & \lambda_0 \end{bmatrix} \begin{bmatrix} 0 \\ \omega \end{bmatrix} \quad (10.16)$$

$$\dot{\mathbf{v}} = \sum \mathbf{F}(\mathbb{M})^{-1} \quad (10.17)$$

$$\dot{\omega} = \mathbf{J}^{-1} (\mathbb{M}_{\mathbb{G}} - \omega \times (\mathbf{J} \cdot \omega)) \quad (10.18)$$

Where \mathbf{J} is the inertia tensor.

All the forces and moments are calculated for the fuselage and the individual rotors.

$$\mathbf{Y}_{\mathbf{F}_i} = [F_x F_y F_z] \quad (10.19)$$

$$\mathbf{Y}_{\mathbf{M}_i} = [M_x M_y M_z] \quad (10.20)$$

The i represents the different elements fuselage and the 4 rotors respectively. Finally the RPMs of the individual rotors and the input voltages are logged.

$$\mathbf{Y}_{\text{rpm}_i} \quad (10.21)$$

$$\mathbf{Y}_{\mathbf{V}_i} \quad (10.22)$$

Resulting in the complete state vector \mathbf{Y} :

$$\mathbf{Y} = \begin{bmatrix} \mathbf{Y}_{\text{rb}} \\ \mathbf{Y}_{\mathbf{F}_i} \\ \mathbf{Y}_{\mathbf{M}_i} \\ \mathbf{Y}_{\text{rpm}_i} \\ \mathbf{Y}_{\mathbf{V}_i} \end{bmatrix} \quad (10.23)$$

10.2 Advanced Model

For the real simulation a more advanced model is used [16]. This model includes:

- Aerodynamics of the wing
- Inflow calculations
- Propeller model (Blade Element Method)
- Motor model (including inertia and motor dynamics)

The program is written in the MATLAB environment and contains different elements called `functions`. These functions are subprograms each calculating an output from an input, as the main program does as well. The main program calls the functions in the shown sequence in figure 10.1.

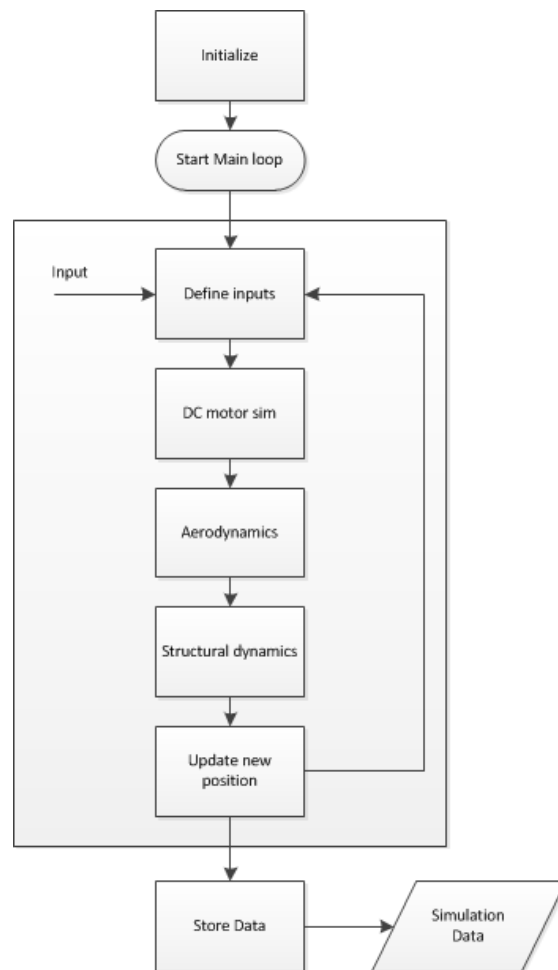


Figure 10.1: Dynamic model calculation sequence

10.2.1 Dr. One representation

In the advanced model Dr. One is modeled as four rotors and a wing. The geometry and the masses are implemented in the model. The propellers coefficients are obtained by the blade element method which are incorporated in the dynamic model. The wing is represented by its geometry and its aerodynamic coefficients calculated in appendix K.

10.3 Dynamic analysis

In this section the dynamics of the system using the dynamic model is analysed. The procedure is shown in figure

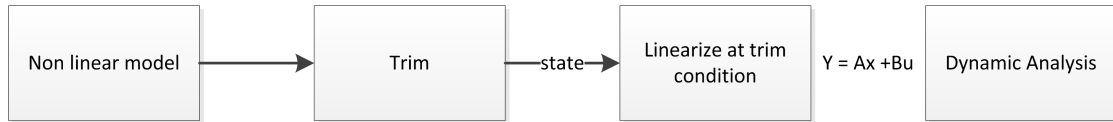


Figure 10.2: Flow chart dynamic analysis

First the non-linear model is trimmed at different trim states. For example the first trim condition is hover, meaning zero velocity in all three directions and zero rotations around the three principle axes. DrOne is trimmed to meet the zero velocity conditions. Other trim conditions are defined varying the velocity in u-direction in the body fixed frame. Then the system is linearized at the trim condition resulting in a system of the following form.

$$\dot{\mathbf{x}} = \mathbf{Ax} + \mathbf{Bu} \quad (10.24)$$

$$\mathbf{y} = \mathbf{Cx} + \mathbf{Du} \quad (10.25)$$

Investigating the eigenvalues of the matrix A, explained in chapter 11 gives an indication of the open loop stability of the system.

10.4 Trim

The non-linear system is trimmed for a range of forward velocities. At each forward velocity the rotational velocities of the propeller and an according pitch angle are found at the equilibrium condition. When the velocity increases the nose starts to pitch down. The plotting of the pitch angle at trimmed condition are shown in figure 10.3.

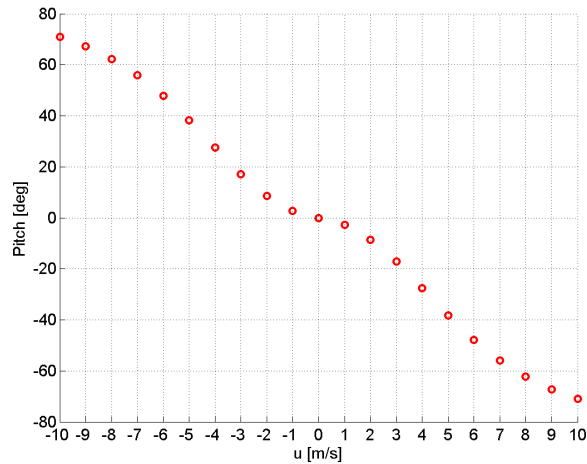


Figure 10.3: Pitch angle at trimmed condition for different velocities u

At each trim condition the stability of the system can be examined by linearizing and examining the eigenvalues of the A matrix.

10.5 Eigenmotions

The dynamic analysis is difficult since most modes are coupled meaning that the pitch, roll and yaw do not show up as independent modes. When the aircraft starts rolling due to generated moments it will also start to yaw and move sideways referred to as side slip. Therefore in classical aircraft design so called eigenmotions [18] are examined. Full elaboration on the dynamic analysis is beyond the scope of this thesis but as a example one eigenmotion is discussed: the Dutch roll.

The Dutch roll is an eigenmotion consist of a yaw-roll coupling and side slip. In other words the ϕ, β, p and r are coupled where β is a parameter considering the side slip:

$$\beta = \sin^{-1} \frac{u}{V} \quad (10.26)$$

Hence a large value of u can be identified as side slip.

When the eigenvectors of a trim condition are examined coupling can be identified as the dutch roll. The according eigenvalue can then be assigned to the dutch roll. The according eigenvalues are plotted in figure 10.4

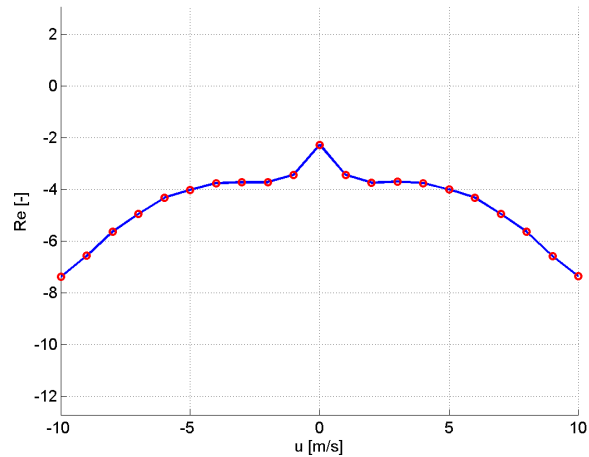


Figure 10.4: Eigenvalues for the Dutch roll for different velocities u

It can be seen that the Dutch roll is stable since the real values are negative and becomes more stable when the forward speed is increasing, the values become more negative. Due to more forward velocity the eigenmotion becomes more stable. You can compare it to riding a bicycle i.e. it is easier to balance when it is moving than when it is standing still.

10.6 Conclusion

This chapter introduced the dynamic model. The rigid body dynamics were derived which resulted in a system of first-order differential equations. A more advanced model was shown which incorporates the aerodynamics of the wing and propellers along with inflow calculations as well a motor model. An eigenmotion, the Dutch roll, has been analyzed. However for collaborate results the model has to be validated first. More on the validation process can be found in chapter 11.

Chapter 11

Control

The control algorithms form the translation from the sensor data, measuring attitude, velocities and accelerations to control inputs to stabilize and control the aircraft. There are many different control algorithms varying from simple proportional controllers to non-linear multi-in multi-out controllers. An open source platform has been chosen where sensors are communicating with the control software and the control inputs are sent to the controls. In this case the rotational velocities of the four motors. In this chapter a first step is taken in the control design using PID controllers and a mathematical model described in the previous section. Since Dr.One is a hybrid configuration the controls consist of two modes instead of one, a vertical mode when flying as a multicopter and a horizontal mode when flying as a fixed wing aircraft. The vertical mode uses the principle of the control system of a quadcopter, whereas the horizontal mode is a new control mode, not been seen before.

11.1 Vertical flight controls

Quad copters are a variation of the helicopter. Instead of having a tail rotor to compensate for the yawing-moment the rotors rotate in pairs in opposite direction. Most quad copters are electrical powered since the thrust of the electrical motors can be rapidly and accurately controlled. Quad copters do not have control surfaces or variable pitch propellers for control. They simply rely on different rotational velocities resulting in different thrusts. The individual maneuvers are shown in figure 11.2.

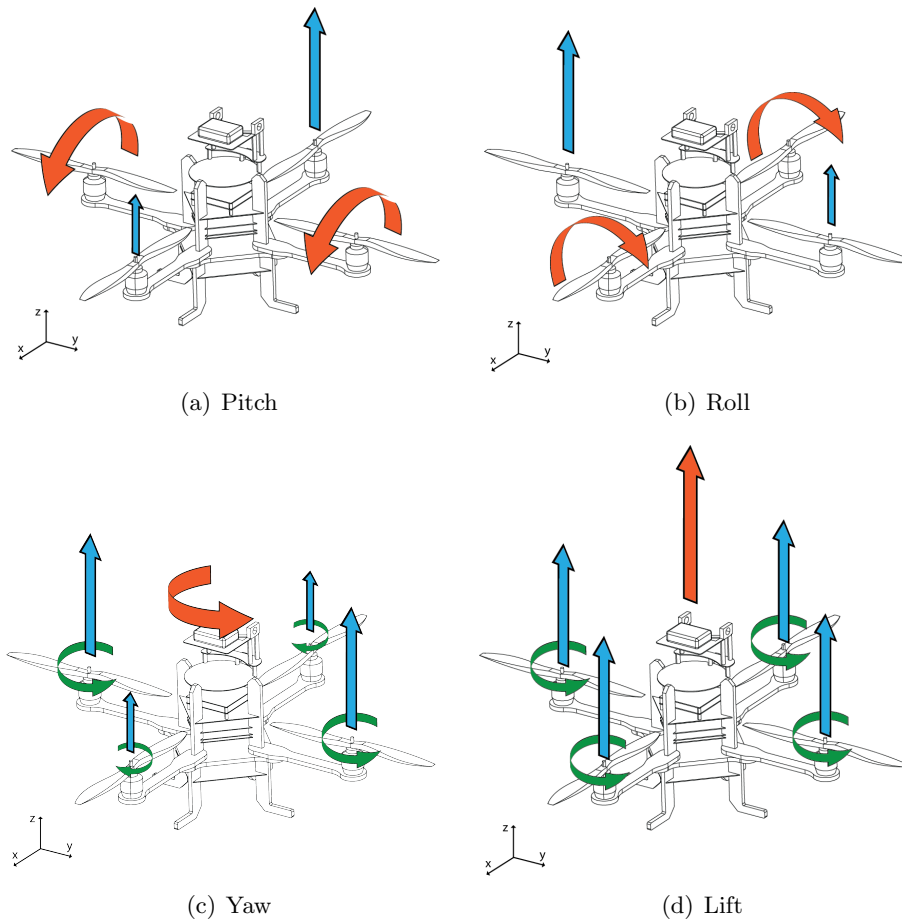


Figure 11.1: Control modes of a quadcopter

- pitch control: by converse change of motors on x-axis, see figure 11.1(a)
- roll control: by converse change of motor y-axis, see figure 11.1(b)
- yaw control: by rotor speed imbalance of motors on x-axis and y-axis, see figure 11.1(c)
- vertical motion: For vertical motion rotor speed of all motors is changed equally, see figure 11.1(d)

11.2 Horizontal flight controls

For horizontal flight Dr.One uses the same control principles as the quad copter. However for horizontal control the pitch is rotated 90 degrees and the yaw controls for vertical flight become the roll controls for horizontal flight and viceversa.

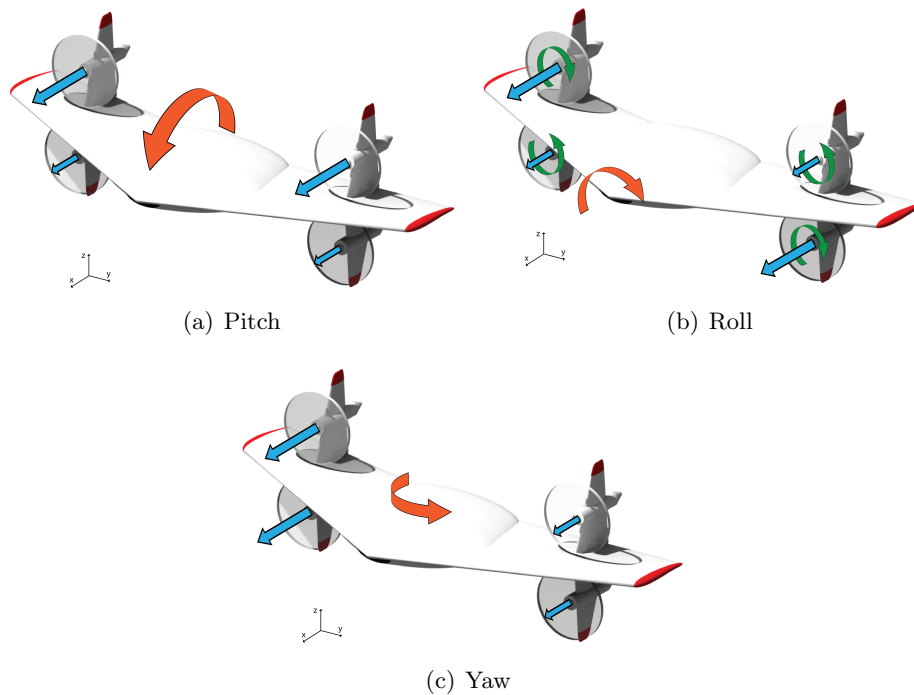


Figure 11.2: Control modes of Dr.One

- pitch control: increasing the rotor speed on the upper side of the wing makes the aircraft pitch downward, see figure 11.2(a)
- roll control: increasing the counter clockwise rotor speed creates a moment around the x-axis resulting in a roll to the left, see figure 11.2(b)
- yaw control: increasing the rotor speed of the motors on the right side results in a yaw to the left, see figure 11.2(c)

11.3 Control design

As mentioned there are many ways to translate the sensor data into control inputs. To design a good performance controller an accurate mathematical model is needed. This mathematical model needs to be validated using flight data. The inputs of the flight data is fed into the model and the model is tuned until the output matches the output of the flight data. To obtain accurate flight data is crucial and therefore a log platform was developed. To capture all the dynamic motions a frequency of 100Hz is necessary. An affordable system was not available hence a log platform had to be developed. Full elaboration on this is found in appendix J. At this stage the model has not yet been validated, however the design scheme of the control is presented and generally verified on a non-validated model in the following sections to illustrate the feasibility. When the model is validated the design scheme can be initiated and the controls can be designed and verified using the prototype.

By linearizing the model at the trim conditions, as described in section 10.3, and by analyzing the eigenvalues we can obtain the information to design an optimized controller. For the initial design of Dr.One it was chosen to use a proportional feed-forward and PID (Proportional Integral Differential) feedback control for each of the attitude angles (ϕ, θ, ψ) , since these are widely used in these applications. An off-the-shelf autopilot, the Lisa M [19] is installed on the first prototype, which comes with the feed-forward and PID feedback control installed. For further optimization of the performance, more complicated controllers such as multi-in multi out non-linear controllers can be implemented, but this is beyond of the scope of this thesis.

The optimum gains of the controllers can be calculated using the linearized system.

The design of the controls is done in different steps. First the optimum controllers are designed on the linearized system. Then the controllers can be verified in the non-linear model. Finally the controls can be programmed in the autopilot, see appendix L and can be tested on the prototype. The scheme is shown in figure 11.3.

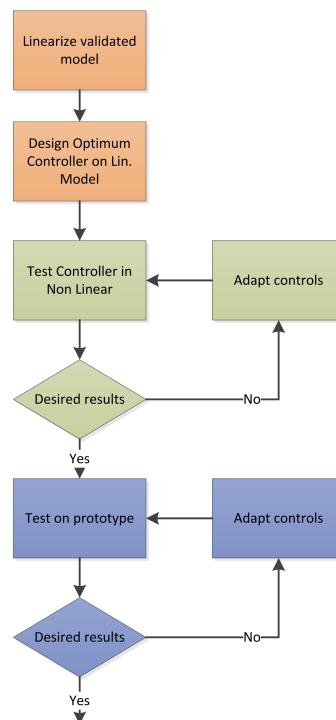


Figure 11.3: Control design scheme, the different colors represent the different models, linear, non-linear, real flight respectively

11.4 Control on linearized system

The control system uses four inputs, namely the rotational velocity of each of the four different motors. The linearized system is defined in the state-space, as shown in equation 10.24. The full system is a MIMU (Multi-In Multi-Out) system and consists of 12 states and four inputs resulting in:

$$A = [12 \times 12] \quad (11.1)$$

$$B = [12 \times 4] \quad (11.2)$$

$$C = [12 \times 12]I \quad (11.3)$$

$$D = [12 \times 4][0] \quad (11.4)$$

For the controller design the system is split up into four SISO (Single-In Single-out) systems. One SISO system becomes:

$$A = [12 \times 12] \quad (11.5)$$

$$B = [12 \times 1] \quad (11.6)$$

$$C = [1 \times 12] \quad (11.7)$$

$$D = [12 \times 1][0] \quad (11.8)$$

Where the C matrix the control mode matrix, and consists of an array of zeros and a one for the state that wants to be controlled. The array corresponds to the state vector described in chapter 10. For example for the pitch (θ) the 11th entry of C becomes one. Using the PID-tuning algorithms of MATLAB the gains of the PID controllers, Kp, Kd and Ki, are tuned.

- Kp = proportional gain
- Kd = differential gain
- Ki = integral gain

11.5 Pitch control

The configuration is shown in figure 11.4.

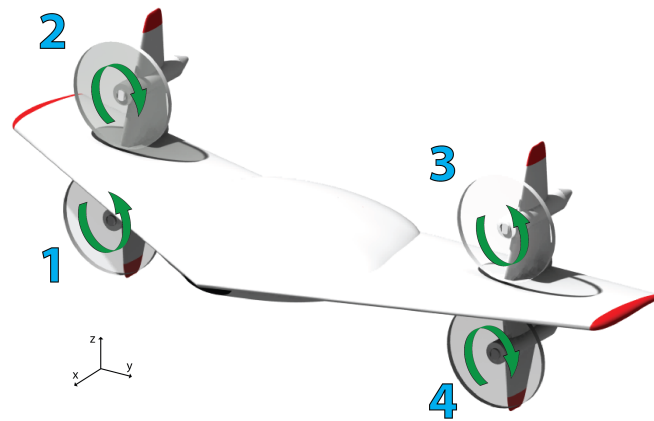


Figure 11.4: DrOne configuration of the motors

For pitch control it is expected that the controllers for motor 1 and 4 have similar values as for motors 2 and 3. More over it is expected that motors 1 and 4 have opposite sign compared to motors 2 and 3.

11.5.1 Linear system

The linearized system is used to run PID control algorithms.

Plotting the proportional gains give:

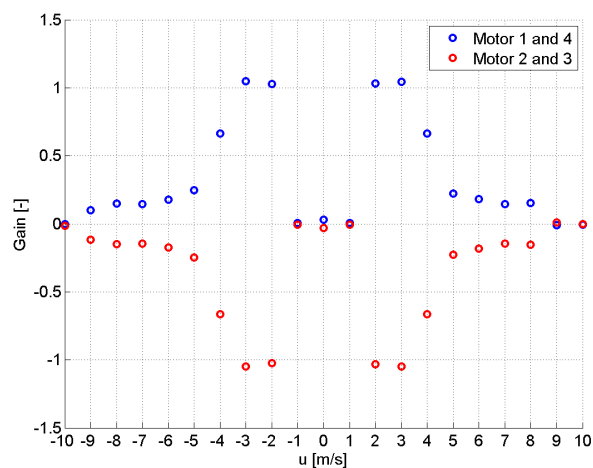


Figure 11.5: K_p for different trimmed velocities u

Figure 11.5 confirms the expectations. This allows the plotting of the controller of one motor since the others are the same or opposite sign. This is verified for the K_i and

Kd as well.

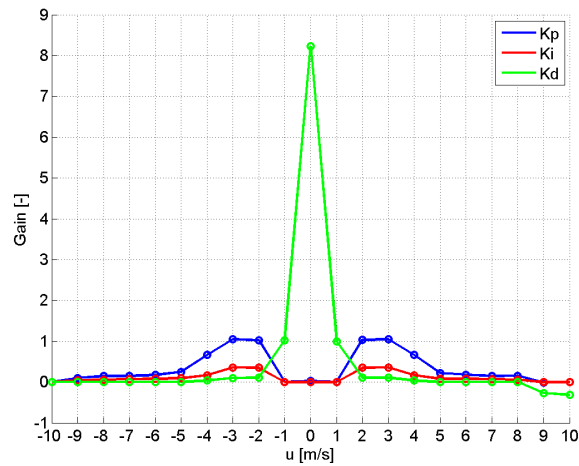


Figure 11.6: K_p, K_i, K_d for different trimmed velocities u

Figure 11.6 shows three regions with different gains, hover ($< 2\text{m/s}$), low velocities ($2\text{-}5\text{m/s}$) and higher velocities ($> 5\text{m/s}$).

At velocity is 0m/s there was a large peak in the K_d gain, which is generally not a good sign. A closer look revealed that at this velocity the algorithms cannot find an optimum controller. The differential gain was omitted for hover and will be tuned manually.

11.5.2 Non-linear system

For the pitch, the algorithm was adapted to ignore the differential gain, in other words design a PI controller instead.

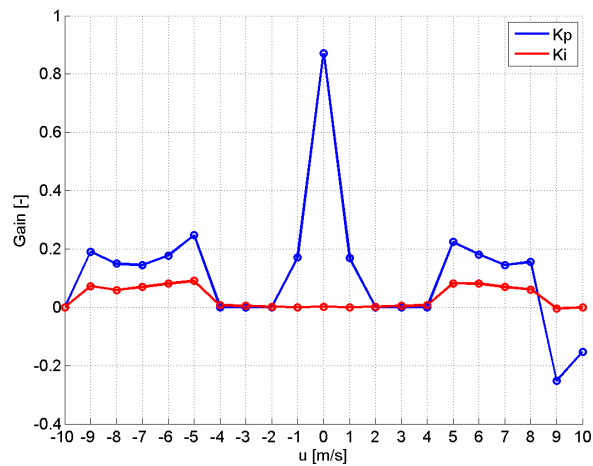


Figure 11.7: K_p, K_i for different trimmed velocities u

The non-linear simulation ran for 4 seconds and had an initial angle of 10 degrees. The control was set to the trim pitch, which at hover is zero.

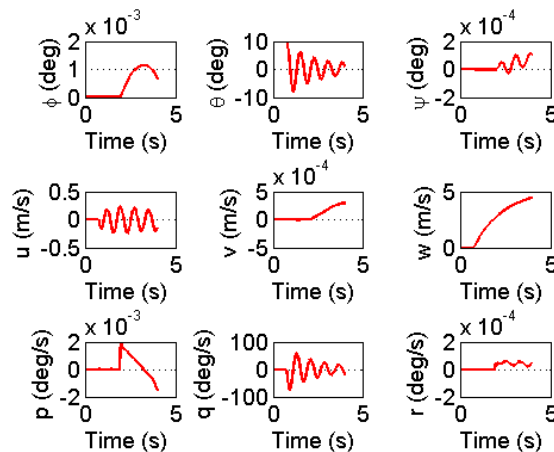


Figure 11.8: Non-linear simulation at hover ($u=[0 \ 0 \ 0]$) using a PI controller

It can be seen that due to the absence of the differential gain it oscillates around the equilibrium condition. Introducing differential gain of -0.2 is shown in figure 11.9.

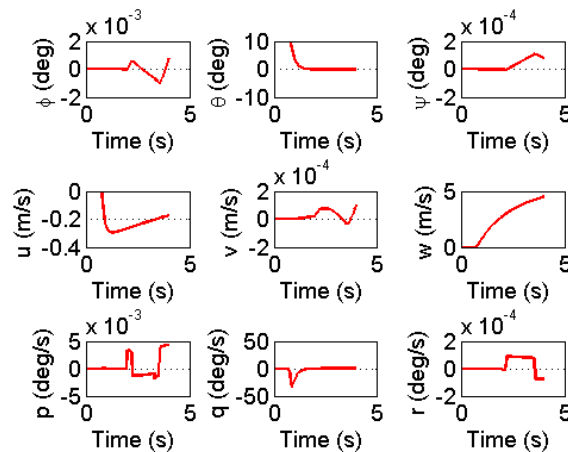


Figure 11.9: Non-linear simulation at hover ($u=[0\ 0\ 0]$) using a PID controller

This is the more desired result. Dr.One nicely goes from 10 degrees positive to its trim position without any overshoot.

11.6 Roll and yaw control

The roll and yaw controls are done in a similar way as the pitch control. First the gains were determined using the linear system and verified with the expectations.

- horizontal roll (vertical yaw) negative gain for motors 1 and 3 and positive gain for 2 and 4
- horizontal yaw (vertical roll) negative gain for motor 1 and 2 and positive gain for 3 and 4

It can be concluded that the dynamic system behaves as expected.

When implementing the controls it was observed that the controls have coupling effects. When the pitch control is tuned, as done in the previous section and the roll control is added, the pitch control is affected. This tuning process is time consuming and therefore costly. It was found that the dynamics of a hybrid system such as Dr.One are very sensitive. A minor shift in center of gravity, propeller dimensions, or position of the motors have a great influence on the behavior. Therefore analysis should be done only on a validated model. At this stage the model is not yet validated hence further tuning of the controls has been postponed.

11.7 Vertical and horizontal flight controls

Hence the system behaves as expected in vertical flight mode, the question is, how will it behave when the system's forward velocity is increased until it reaches horizontal flight?

It is expected to see a change in the controls, namely:

- pitch control remains the same: motors 1 and 4 differ sign from motors 2 and 3
- roll control becomes yaw control: motors 1 and 3 differ sign from motors 2 and 4
- yaw control becomes roll control: motors 1 and 2 differ sign from motors 3 and 4

Capturing the gains for the controls at zero m/s flight speed which corresponds with zero pitch and 10 m/s which corresponds with -71 degrees give:

V [m/s]	0				10			
pitch	+	-	-	+	-	+	+	-
roll	-	-	+	+	-	-	+	+
yaw	+	-	+	-	-	-	+	+

Table 11.1: Gains at vertical and horizontal flight

From table 11.1 it can be seen that the pitch controls are the same (but opposite sign) and the yaw becomes the roll. The roll however does not appear to transform into the yaw control. When inspecting the values it was found that the second and third, made red in the table are much larger than the first and the fourth, hence dominating the control. The second and the third do correspond to the yaw controls at vertical flight. It can be concluded that the dynamic model and control design on the linearized model in general works as expected.

11.8 Model validation

In order to properly design the controls, the model has to be validated with experimental flight data. With this flight data the model can be tuned to match the real life situation. With this validated model the controls can be designed using the methods explained in the previous sections. To obtain the flight data a series of tests have to be performed.

11.9 Flight Tests

To obtain proper measurements the sensors have to be carefully checked. The sensors are highly sensitive to magnetic fields generated by the motors and the current through the power cables. Therefore a checklist has been created to ensure a successful measurement, it can be found in appendix O.

Several differences have been discovered between the 'train' test, performed in section J.2.6, and the flight test. First of all the train test is a rather stationary platform. Dr.One is a very agile platform, with aggressive accelerations. This had several consequences for the measurements and the settings had to be adapted. First the EKF filter had to be changed to lower values as explained in section J.2.4. Furthermore the sequence of filtering the quaternions first and then transform them back into Euler angles did not seem

to give accurate results. For the flight tests the measured quaternions are converted into Euler angles directly before other data processing is done.

11.9.1 Verification sensors

To verify the IMU a flight test was recorded on video and a visualization was recreated with the measured data obtained from the log platform. In order to recreate the flight the data needs to be processed. First the time has to match the recorded video therefore the data has to be resampled to the sampling frequency of the video. Furthermore the data has to be smoothed to eliminate shocks in the video. This needs to be done carefully since low-pass filters cause phase lag and peaks can be reduced.

Verification of the RPM sensors are validated in appendix J.6.

11.9.2 Test maneuvers for model validation

First four different channels are introduced and for each a series of tests will be performed. The channels are, pitch, roll, yaw and heave. The different tests are:

- Sweep: flying Dr.One with sweeps with increasing frequency.
- Step: start from hover, give a maximum positive input quickly and holding as long as possible
- Doublet: starts from hover, give a large positive input followed by a large negative input

For the validation of the model several tests will be performed on each channel.

The first prototype of Dr.One has been fitted with an autopilot and is in testing phase. The flight data from the first test flights can be found in appendix M.

11.10 Validation of log platform

Flight tests were performed using a off-the-shelve quad copter autopilot. A test flight covering different maneuvers was recorded on video. From the measured flight data the flight was reconstructed using a 3D CAD model and compared with the original. It could be concluded that the sensors were working accurately.

11.11 Future

At this stage the first Dr.One prototype has been fitted with a programmable autopilot and is in the configuration phase. When the prototype is robust enough the configuration will be frozen, meaning that no changes are made to the prototype that can effect the dynamics. Then the model can be validated and the process described in figure 11.3 can be followed.

11.12 Conclusion

The lay-out of the complete control design was shown. The tuning process was shown and illustrated for pitch control. Since the tuning process is a time consuming and costly process the model has to be validated first to ensure collaborated results.

The gains found by the gain tuning algorithms match the expected results i.e. the combination of motors responsible for the different attitudes, pitch, roll and yaw, in vertical and horizontal flight complied with the expected results.

The measurements done by the log platform were validated with a flight test. After proper calibration, the results of the log platform were accurate. The general results of vertical to horizontal flight controls were checked and the model outputs complied with expected results. At this stage the prototype is fitted with a programmable autopilot and is in the configuration phase. When this stage is completed the model will be validated and the controls can be designed.

Chapter 12

Conclusion

Dr.One has the potential to have an impact on facilitating health care in Africa. The use of Dr.One can save many lives by transporting blood packs to patients, dealing with epidemics and supplying local health posts.

This thesis describes how the Dr One concept meets the requirements for operating in the difficult environments for which it was conceived and could therefore be an invaluable aid in the distribution of health care products in countries such as Africa.

It describes the development of a new type of hybrid UAV which uses no control surfaces or mechanical moving parts and uses automatic guidance systems so requires no pilot.

It is not expensive to build and is not expensive to operate and its flexibility allows it to be tailor-made for purpose and when required new technologies can be added to the design.

It explains how Dr One, by using new production techniques, can be easily built and maintained locally from readily available materials and does not rely on specialist knowledge to construct as it uses automated processes driven by a specially developed design tool. The design tool sizes the body to the needs of the payload and sizes the wings to maximize performance. In order to calculate the performance the performance characteristics of the motor has to be determined, three different methods are shown using acquired data from the manufacturer, an online tool eCalc and a developed set up to determine the characteristics experimentally. The performance characteristics of the propellers have been obtained from wind tunnel tests. The motor and propeller have been coupled by matching the torque resulting in the performance characteristics of the full propulsion system. The design tool selects the best propeller motor combination for its designated Dr.One design. To establish the feasibility of the concept, a mathematical model of Dr.One was created to simulate its dynamics. Using this mathematical model a systematic approach for designing the controls has been described along with a detailed description of the procedure of the complete control design. The non-validated model has been used to test the gain tuning algorithms. The gains found were consistent with expected results. In order to successfully design the controls the model has to be validated. To validate the model flight data at high frequencies has to be obtained. To obtain this flight data a log platform has been developed and tested successfully. A

prototype has been built and fitted with a programmable autopilot and flight tests are being carried out. When the configuration stage has been completed the model can be validated and the controls can be designed using the presented control scheme.

Appendix A

Existing UAV

Mainly two types of UAVs will be discussed: Multicopters and fixed wing UAVs. The main driving requirements are take-off and landing without a prepared runway. This requirement will make vertical take-off and landing (VTOL) a requisite. Therefore multicopters are a good candidate. Furthermore the mostly applied fixed wing configurations will be discussed, since they will most likely have good performance in flight. First the principle of the aircraft is briefly discussed. Then the performance of the different configurations was examined focusing on payload, range and flight speed.

A.1 Multitrotor systems

Multitrotor systems are nowadays widely applied for many different applications. These multicopters are a differentiation of the known helicopter. Multicopters are capable of vertical take-off and landing and come in different versions, quad, hexa, octo, with the according number of rotors 4, 6 and 8 as can be seen in figure A.1. The more rotors you have the larger they are and the more payload capacity they have. The costs are also proportionally higher. Police and security forces deploy them for surveillance missions, farmers use them to monitor their land and the forestry commission uses them for wild-life monitoring. Furthermore they are widely available on the consumer market in off-the-shelf packages which can be purchased for a few hundred euros.



Figure A.1: Different multirotor configurations [2][3][4]

A.1.1 Principle

Multicopters are a variation to the helicopter. Instead of having a tail rotor to compensate for the yawing-moment the rotors rotate in pairs in opposite direction. Most Multicopters are electrical powered since the thrust of the electrical motors can be rapidly and accurately controlled. Multirotors do not have control surfaces or variable pitch propellers for control. They simply rely on applying different thrusts on the different motors. Further elaboration on the control system is given in chapter 11.

A.1.2 Payload

The maximum payload of a multicopter is taken fully by the thrust of the motors also referred to as hover flight mode. To determine the maximum payload the maximum take off weight has to be determined first.

A.1.3 Flight velocity

The flight velocity depends mainly on the aerodynamic design and the available thrust of the engines. However bigger engines might result in higher power consumption. Equally the battery capacity can be expanded, however this will add extra weight to the aircraft which will then require more necessary lift, which can then effect the flight range. A careful examination of the components and test have to be carried out to determine the optimum configuration for maximum range. The range of existing multicopter aircraft are shown in figure A.2(b).

A.2 Fixed wing systems

There are many fixed wing UAVs in all sizes and shapes. The focus will be put on electric driven designs.

A.2.1 Principle

The principle of a fixed wing UAV is using a fixed wing with a certain angle of attack rather than a rotor. The shape of the airfoil and the angle of attack of the wing generates a pressure difference between the air above and the air under the wing. Due to this pressure difference the wing is drawn up to fill the space allowing the aircraft to literally hang in the air.

A.2.2 Payload

The payload of a fixed wing aircraft is determined by the lift it can generate with the wing at take-off. Opposed to multicopters fixed wing aircraft are not carried entirely by the thrust generated by the propellers but by the lift force generated with the wing.

A.2.3 Flight velocity

The flight velocity of a fixed wing aircraft is much faster than that of a multicopter. Since the thrust of the motors is in the direction of the flight. Therefore the thrust is more used for forward motions rather than lift.

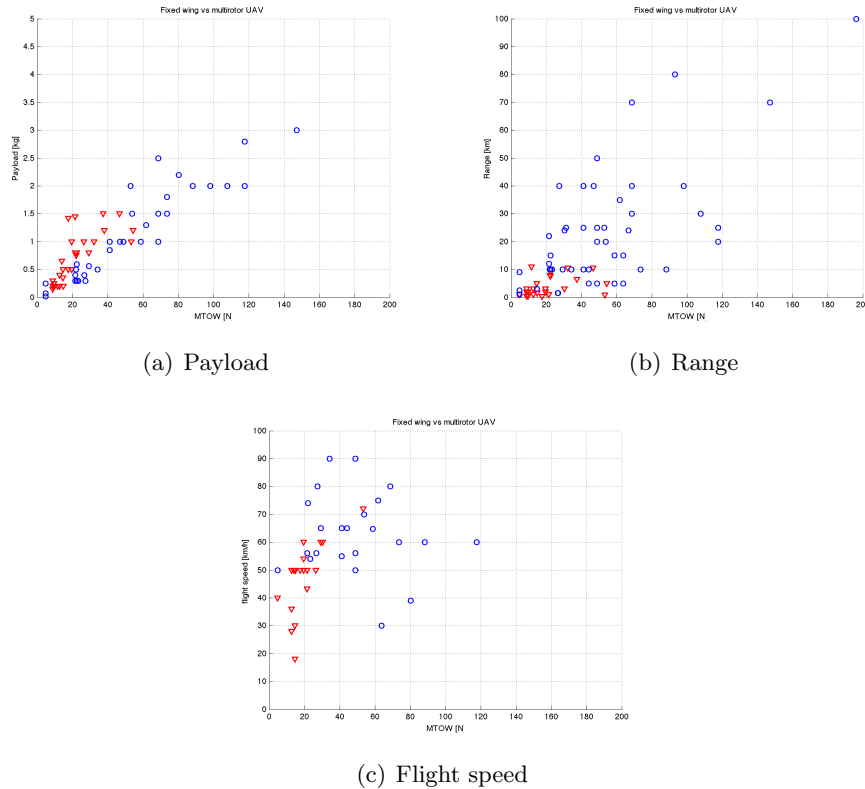


Figure A.2: Performance comparison multicopters and fixed wing aircraft

A database on UAS has been created by Jeroen Veerman. From this database the electrical UAVs have been selected. All three parameters are plotted against the Maximum Take Off Weight (MTOW). From figure A.2(a) it can be seen that the maximum payload an existing multicopter can carry is just under 1.5 kg.

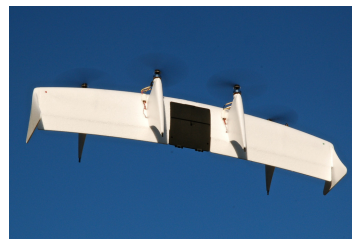
Most electric fixed wing aircraft are not yet designed to carry a payload of over 5 kg. However increasing the size will most definitely enable it to carry bigger payloads. From figure A.2(b) it can be seen that the range of multicopters is far below the target range of 100 km. The range of fixed wing aircraft is significantly higher than for that of multicopters, this is due to the thrust that is needed to generate the lift. Which is much lower for a fixed wing aircraft since it uses the lift characteristics of the wing, rather than relying fully on the thrust of the motors. There are UAVs with a MTOW of 200 N which have a range of 70 km, therefore it looks like a convenient configuration for Dr. One considering range.

A.2.4 Conclusion

Vertical take-off and landing is crucial for Dr.One, pointing towards multicopters. However the flight characteristics of the fixed wing are much better. Therefore the best of both worlds is needed. A new type of aircraft is required, these types of aircraft are referred to as hybrid or convertible aircraft.

A.3 Hybrid UAVs

A different approach is necessary to combine the VTOL capabilities and the high flight speed and range performance. This new type of aircraft called hybrids or convertible aircraft and consist of a wing for forward flight and multiple powerful engines for hover and VTOL. A hybrid UAV will take off like a multicopter using the thrust of the different engines directly. Then a transition takes place rotating the aircraft 90 degrees turning the rotors into forward propulsion. In this way the characteristics of the fixed wing are combined with hover and VTOL capabilities of multirotors. Two of these concepts already exist, namely Quadshot [20] and ATMOS [21]. The concepts are shown in figure A.3.



(a) Quadshot



(b) ATMOS

Figure A.3: Hybrid UAVs [5] [6]

Since the aircraft rotates throughout its mission a definition of the body-fixed coordinate system has to be defined. The body-fixed reference frame is used from the forward flight phase. Meaning the rotors are directed in the direction of flight and the wing has a top and a bottom rather than two sides.

A.4 Quadshot

The Quadshot is a radio controlled model aircraft developed by Transition Robotics. It has four equal engines. Under the wing the two motors are off-set close to the end of the wing whereas on top of the wing the motors are placed more together. It has winglets which functions as the landing gear. Furthermore in horizontal mode it flies like an ordinary aircraft, using elevons for control. Dr.One on the other hand will rely on control by just the motors eliminating the need for elevons.

A.5 ATMOS

ATMOS has been developed at the faculty of aerospace engineering at the TU Delft and is based on the quadshot .

The ATMOS UAV has applied several modifications to the Quadshot design. It has 2 motors for forward flight and 2 motors which are only used with hover. In forward flight 2 motors are shutdown and the propellers fold in. Therefore in forward flight it only flies on the two motors. The ATMOS is symmetric therefore there is no difference between the top or bottom of the wing.

Appendix B

Flight scenario

In this section the flight scenario is assessed. The flight scenario is a chain of events and checks ensuring success and safety of every mission. This chain of events will be processed every flight, hence for a return flight it will run through the chain of events twice. Some processes are done before flight some can be skipped and some will be performed after flight.

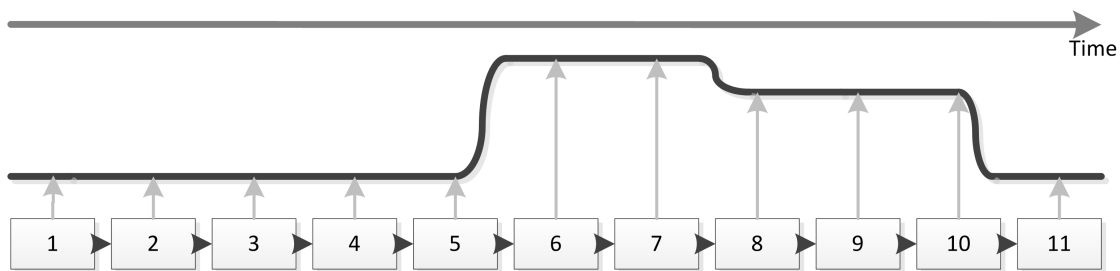


Figure B.1: Time line mission for Dr.One

- 1: Activation signal
- 2: Planning
- 3: Mission Authorization
- 4: Preparation of Dr.One
- 5: Take off
- 6: ETA estimation
- 7: Cruise
- 8: loiter
- 9: Landing Authorization
- 10: landing
- 11: Removal insert payload

Figure B.2 shows the chain of events with respect to the time line of a flight. It can be seen that events 1 until 5 are performed before flight, 6 until ten during flight and 11

after landing.

1: Activation signal

The caller sends information regarding, location, time window, fallback locations in case of failure.

2: Planning

The mission will be planned at the ground station. Flight plan will be developed taking into account:

- flightpath under 400ft due to regulations
- obstacle avoidance using heightmaps and 3D static obstacle mapping
- weather conditions
- determine safe fallback locations
- planning of return flight
- possibility of recharging at site
- inform destination

3: Mission Authorization

The mission will be checked on its feasibility and safety, considering the elements from 2.

4: Preparation of Dr.One

Then Dr.One is prepared for its mission. The lipo batteries are installed, equipped with payload, and autopilot is programmed.

5: Take off Authorization

This consists of checks to determine if it safe for Dr.One to take off. This includes the the aircraft:

- payload
- aircraft systems activated
- battery check
- autopilot configuration

And the take off location,

- no human or animal too close to take off site

- no obstacles above aircraft
- battery check
- autopilot configuration

This will be done autonomously using the preprogrammed flight path in the autopilot. Dr.one will take-off and climb to the cruise altitude.

6: ETA estimation

The estimated time of arrival is determined and communicated to the contact person at the target location.

7: Cruise

The autopilot will fly at optimum conditions, considering using power, flight speed etc.

8: loiter

When Dr.One arrives at the target location, it will loiter until the landing authorization signal is received.

9: Landing Authorization

The landing authorization similar to the take off authorization where it now checks the landing site and aircraft condition to ensure safety.

10: landing

The landing authorization process is similar to the take off authorization. It checks the landing site and aircraft condition to ensure safety.

11: Removal insert payload

The payload is removed when it reaches its destination or loaded for transportation back to base.

During the flight the ground station is constantly updated on Dr.Ones location.

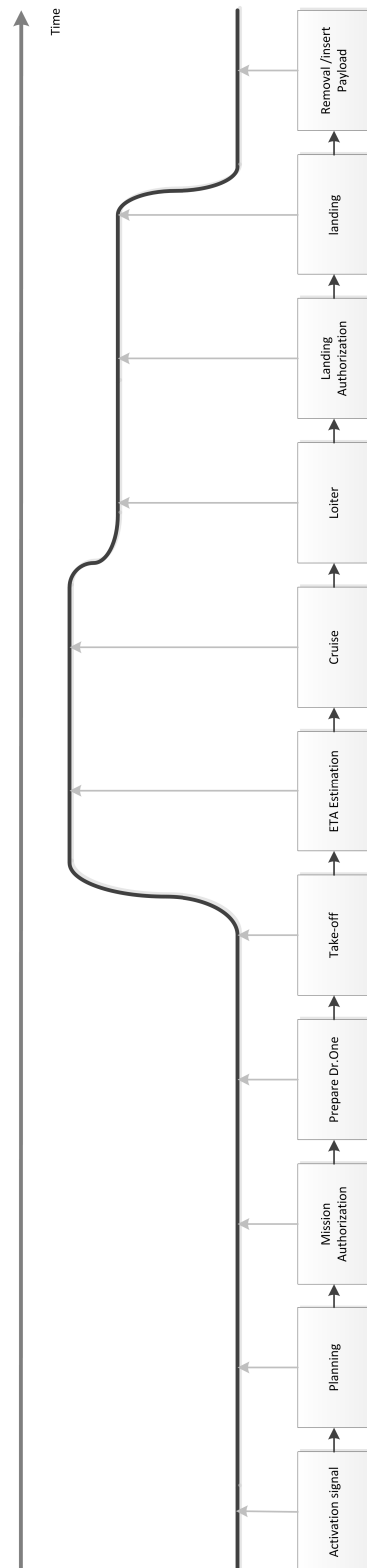


Figure B.2: Time line mission for Dr. One

Appendix C

Development master schedule



Figure C.1: TRL I-IV

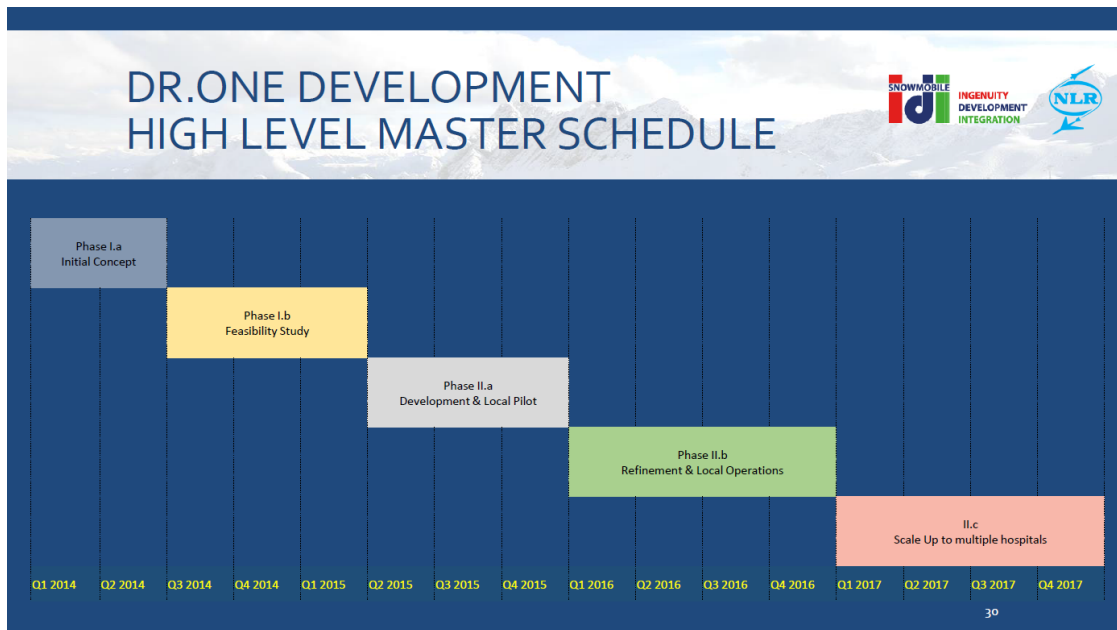



Figure C.2: Planning TRL I-II



Figure C.3: TRL IA

PHASE IB FEASIBILITY STUDY



- Takes place in both Ghana and the Netherland
- Ghana Upper East HS on-board
- Expected cost: 300 k€

Situation Analysis and Use Case Refinement (30 k€)
 Expanded Stakeholder engagement (30k€)
 Development of detailed business plans (50 k€)
 Development of prototypes (TRL 5-6) (130k€)
 Communications/ Marketing/ Fundraising (30 k€)
 Program outline, organisational refinement and Management (30 k€)

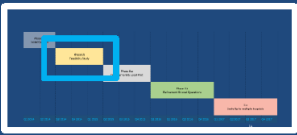


Figure C.4: TRL IB

PHASE II.A PILOT BOLGATANGA



- Local Pilot in Bolgatanga
- Operate 1 Dr.One system between Bolgatanga district hospital and 1 CHPS
- Expected cost: 1750 k€

• System development (TRL 6)
 • Setup Local Pilot environment
 • Prototype testing in region
 • Develop logistics & training
 • Business Case Development
 • Technical risk mitigation (TRL6)
 • Financing and Local Teaming
 • Setup outlines of Dr.One program office
 • Communications/ Marketing/ Fundraising
 • Project/Financial management



Figure C.5: TRL IIA



Figure C.6: TRL IIB

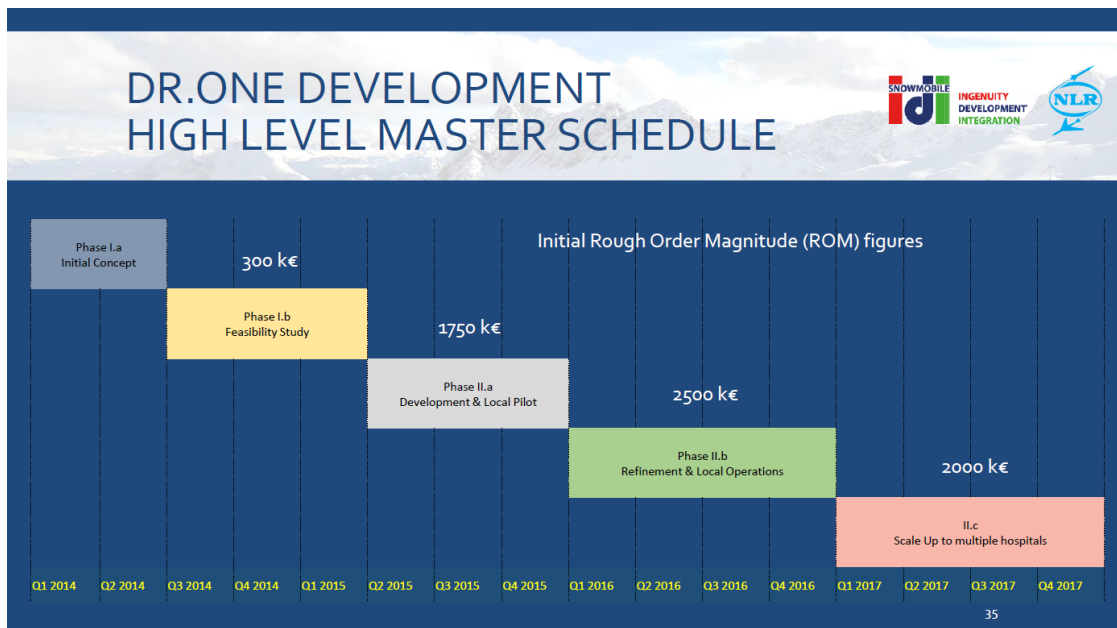


Figure C.7: TRL cost estimation

Appendix D

Naca 4 digit airfoil shape

A four digit Naca airfoil is calculated in three different steps [22]. The first step is to determine the thickness. This is done by the following equation:

$$\frac{t}{2}c \left[0.2969\sqrt{\frac{x}{c}} - 0.1260\left(\frac{x}{c}\right) - 0.3516\left(\frac{x}{c}\right)^2 + 0.2843\left(\frac{x}{c}\right)^3 - 0.1015\left(\frac{x}{c}\right)^4 \right] \quad (\text{D.1})$$

- c = chord of the airfoil [m]

The second step is to determine the camberline:

$$y_c = \begin{cases} m \frac{x}{p^2} \left(2p - \frac{x}{c} \right), & 0 \leq x \leq pc \\ m \frac{c-x}{(1-p)^2} \left(1 + \frac{x}{c} - 2p \right), & pc \leq x \leq c \end{cases} \quad (\text{D.2})$$

- m = maximum camberline [m]
- p = location of maximum camber [m]

The third and final step is to calculate the upper and lower curve:

$$\begin{aligned} x_u &= x - y_t \sin \theta & y_u &= y_c + y_t \cos \theta \\ x_l &= x + y_t \sin \theta & y_l &= y_c - y_t \cos \theta \end{aligned} \quad (\text{D.3})$$

where,

$$\theta = \arctan \left(\frac{dy_c}{dx} \right) \quad (\text{D.4})$$

and

$$\frac{dy_c}{dx} = \begin{cases} \frac{2m}{p^2} \left(p - \frac{x}{c} \right), & 0 \leq x \leq pc \\ \frac{2m}{(1-p)^2} \left(p - \frac{x}{c} \right), & pc \leq x \leq c \end{cases} \quad (\text{D.5})$$

Appendix E

Analyzing design variables

Now it is time to see how the design variables effect the range.

E.1 Wingspan and flight speed on minimum drag

Since the drag consists of two parts, the induced drag and the pressure drag, there exist a flight speed for which the drag is minimal for every wingspan. To give an indication the wingspan and flight speed are plotted against the drag, using the brute force method shown in appendix E.2.

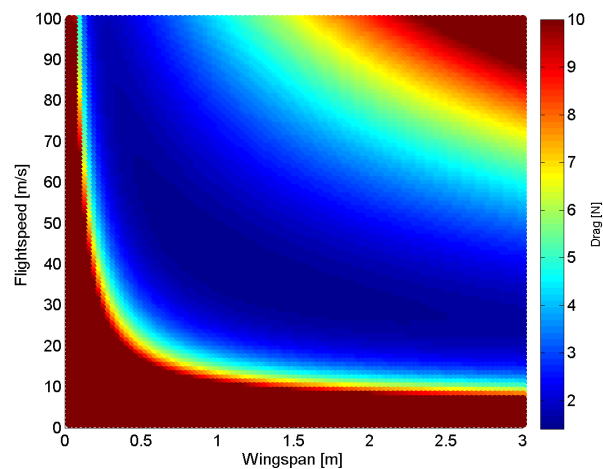


Figure E.1: Wingspan and flight speed against drag

Setting the wingspan at 0.8 meter as an initial design.

This allows the drag curve to be plotted against the flight speed.

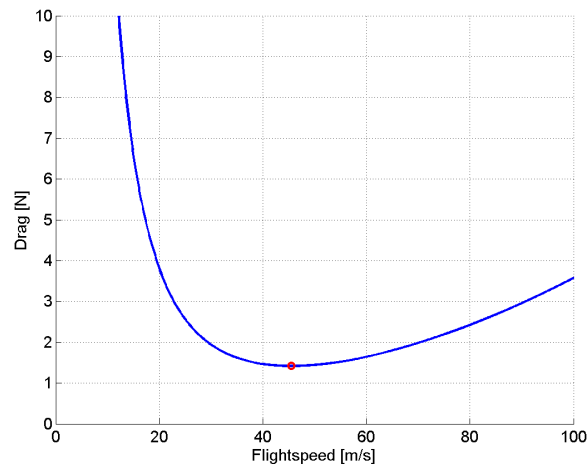
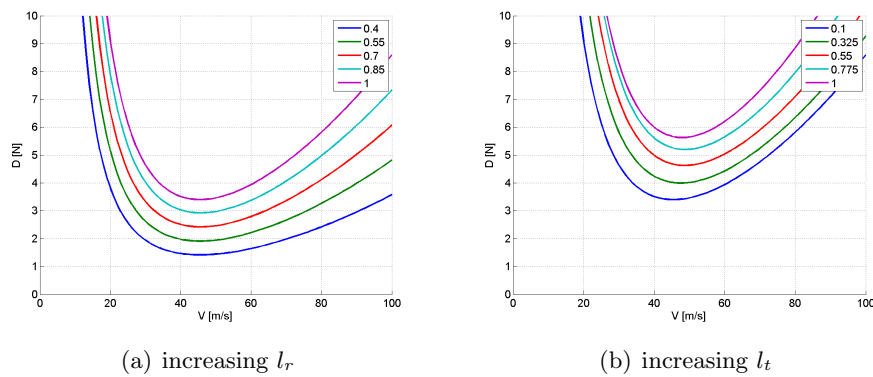


Figure E.2: Drag curve for $b = 0.8\text{m}$

The root chord and tip chord contribute directly to the wing surface which increases the drag. Varying the root chord results in increasing drag curves.



(a) increasing l_r

(b) increasing l_t

Figure E.3: Drag curves for increasing wing geometry

The root and tip chord should be chosen so that the minimum drag matches the thrust generated at the optimum point.

It can be seen that the drag increases linearly when the geometry is increased.

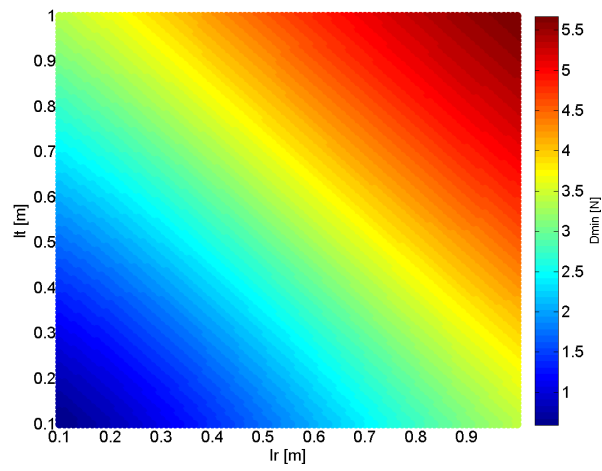


Figure E.4: D_{min} for different root chord and tip chord

Using figure E.4 gives:

parameter	value
l_r	0.4m
l_t	0.2m
b	0.8m

Table E.1: Wing parameters initial design

Adding 30 degrees of sweep to put back the neutral point gives the first wing design.

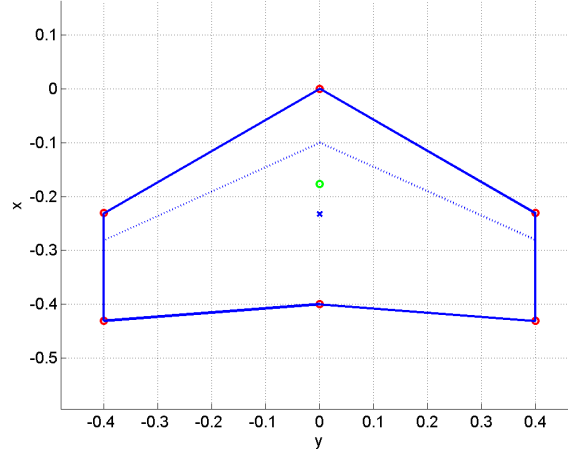


Figure E.5: Wing geometry initial design

E.2 Brute force method

To get a better insight the objective function is plotted for every possible combination of the variables. This is referred to as the 'Brute Force' method. A grid is created between the lower bound and the upper bound of each variable using:

$$x_i = l_b + (n - 1) \frac{l_u - l_b}{(n_{tot} - 1)} \quad (\text{E.1})$$

- x_i = the design variable vector
- i = index for the different design variables
- l_b = lower bound of the design variable
- l_u = upper bound of the design variable
- n = index of the number of steps
- n_{tot} = total number of steps

The number of possible combinations are given by:

$$n_{com} = (n_{des})^{n_{tot}} \quad (\text{E.2})$$

- n_{des} = number of design variables

A combination matrix is established in the following way:

The first variable x_1 is iterated through its steps:

$$x_1 = [x_{1_1} \cdots x_{1_n}, x_{1_1} \cdots x_{1_n}]^T \quad (\text{E.3})$$

The second variable is iterated but it repeats each value n times.

$$x_2 = [x_{2_1} \ x_{2_1} \ \cdots \ x_{2_n} \ x_{2_n}, x_{2_1} \ x_{2_1} \ \cdots \ x_{2_n} \ x_{2_n}]^T \quad (\text{E.4})$$

The third variable is iterated but repeats each value n^2 times. The fourth variable $n^4 = 8$ times. The m th variable repeats its value n^{m-1} times.

This method calculates all possible combinations and resulting in long computational time. For example with 4 variables and 10 steps the method requires the computation of the objective function $10^4 = 10000$ times.

Appendix F

Thrust and Power coefficients

F.1 Thrust coefficient

The propeller thrust is given by:

$$F_T = \frac{dm}{dt}v \quad (\text{F.1})$$

- F_T = thrust [N]
- $\frac{dm}{dt}$ = mass flow rate of exhaust [N]
- v = relative velocity of the air with respect to the exhaust [m/s]

Assuming uniform flow:

$$\frac{dm}{dt} = \rho Av \quad (\text{F.2})$$

- ρ = density of air [kg/m³]
- A = Area of propelled air [m²]

Defining the area of the propeller:

$$A = \pi \frac{d^2}{4} \quad (\text{F.3})$$

- d = diameter of the propeller [m]

Relating the v to the rotational speed of the propeller:

$$v = \omega \frac{d}{2} \quad (\text{F.4})$$

Substituting (F.2), (F.3) and (F.4) in (F.1) gives:

$$F_T = \frac{\pi}{16} \rho \omega^2 d^4 \quad (\text{F.5})$$

Introducing the thrust coefficient incorporating additional aerodynamic effects. The thrust coefficient is determined experimentally in wind tunnel tests.

$$F_T = C_T \rho \omega^2 d^4 \quad (\text{F.6})$$

Hence by measuring the rotational speed, and the thrust the thrust coefficient can be determined.

F.2 Power coefficient

The power can be expressed as a function of the propeller torque.

$$P = 2\pi\omega Q \quad (\text{F.7})$$

where Q is the propeller torque is expressed as a function of the torque coefficient rotational velocity and diameter of the propeller.

$$Q = C_Q \rho \omega^2 d^5 \quad (\text{F.8})$$

inserting (F.8) in (F.7) gives:

$$P = 2\pi C_Q \rho \omega^3 d^5 \quad (\text{F.9})$$

Defining the power coefficient:

$$C_P = 2\pi C_Q \quad (\text{F.10})$$

gives:

$$P = C_P \rho \omega^3 d^5 \quad (\text{F.11})$$

The efficiency of the propeller is defined as:

$$\eta_{prop} = J \left(\frac{C_T}{C_P} \right) \quad (\text{F.12})$$

where J is the advance ratio defined as:

$$J = \frac{V}{\omega d} \quad (\text{F.13})$$

- V = flight speed [m/s]
- ω = rotational velocity of the propeller rad/s]
- d = diameter of the propeller [m]

Appendix G

Motor Test

G.1 Data of manufacturer

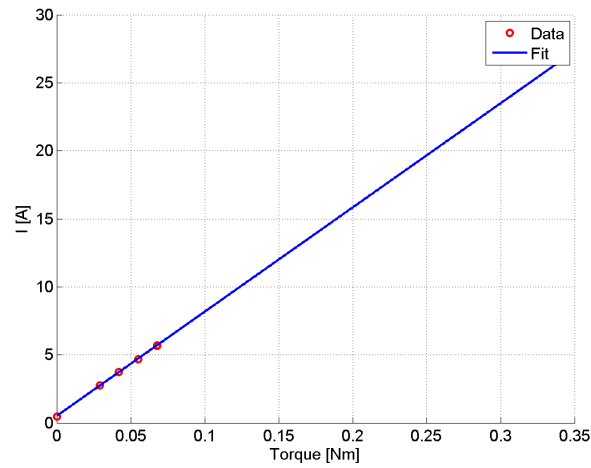


Figure G.1: Results Robbe 2827 torque vs current from manufacturer

This figure shows the drawn current as a function of the applied torque, which are linearly related. In figure G.1 the data points and the curve fitting can be seen.

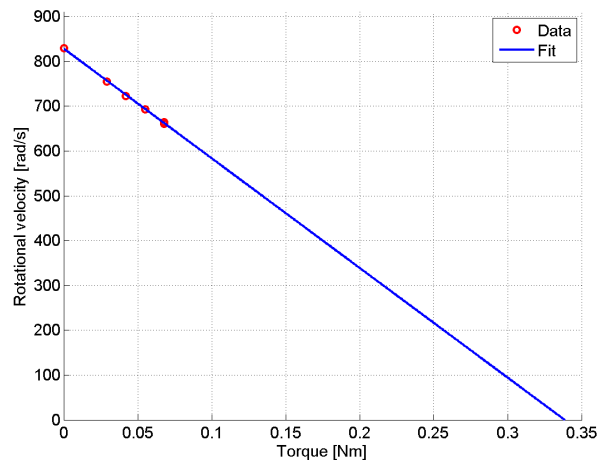


Figure G.2: Results Robbe 2827 torque vs ω from manufacturer

This figure shows the rotational velocity as a function of the applied torque.

G.2 Set up

In order to determine the characteristics of the motor different parameters were be measured. These include, the rotational velocity ω , current I and voltage V and torque of the electric motor. As shown in schematic in figure G.3.

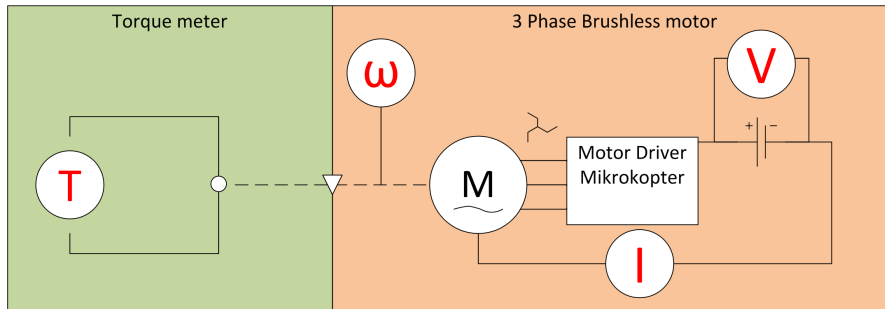


Figure G.3: Setup for motor characteristics

G.2.1 DC motor as torque meter

Since torque meters are very expensive and were not available at the NLR an alternative method had to be devised to measure the torque. A separate DC motor with known characteristics was used as a torque meter. The applied torque was calculated through the relation of the DC motor's current and torque. The DC motor's current is linear with its torque through the torque constant:

$$T = k_T I \quad (\text{G.1})$$

- T = torque [Nm]
- k_T = torque constant [N/A]
- I = current [A]

where the torque constant of the DC motor has to be determined.

The torque constant k_T is related to the voltage constant, however using different units:

$$T = k_T I \quad (\text{G.2})$$

$$E = k_V \omega \quad (\text{G.3})$$

- E = back EMF voltage [V]
- k_V = voltage constant [rad/s/V]
- ω = rotational velocity [rad/s]

where k_T and k_V are the same magnitude but in [N/A] and [rad/s/V] respectively.

The voltage constant is easier to determine experimentally [23] than the torque constant. Two tests were performed. First the motor was driven by another motor and the induced voltage was measured along with the rotational velocity allowing the calculation of the value of the speed constant k_V . The speed constant is related through its inverse with the torque constant:

$$k_T = \frac{1}{k_V} \quad (\text{G.4})$$

A schematic of the setup is given in figure G.4.

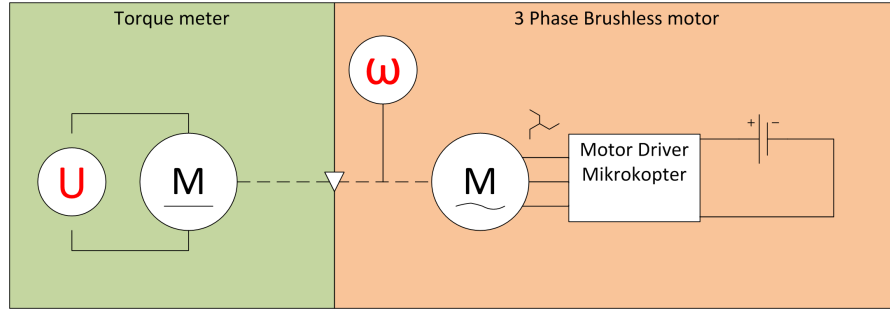


Figure G.4: Setup for measuring k_V

In this test only the induced voltage was measured since no current flowed through the motor, resulting:

$$E_{induced} = k_V \omega \quad (\text{G.5})$$

Secondly the motor was powered using a power source and the voltage and current are recorded along with the rotational velocity. The setup is shown in figure G.5.

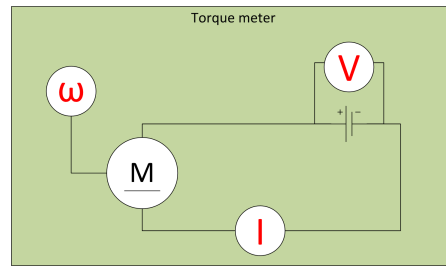


Figure G.5: Setup for measuring k_V

The voltage of the power source is expressed as:

$$E_{bat} = k_V \omega + IR_{armature} \quad (\text{G.6})$$

It can be seen that the internal resistance shows up in the test since a current flows through the motor.

The results of both tests are shown in figure G.6

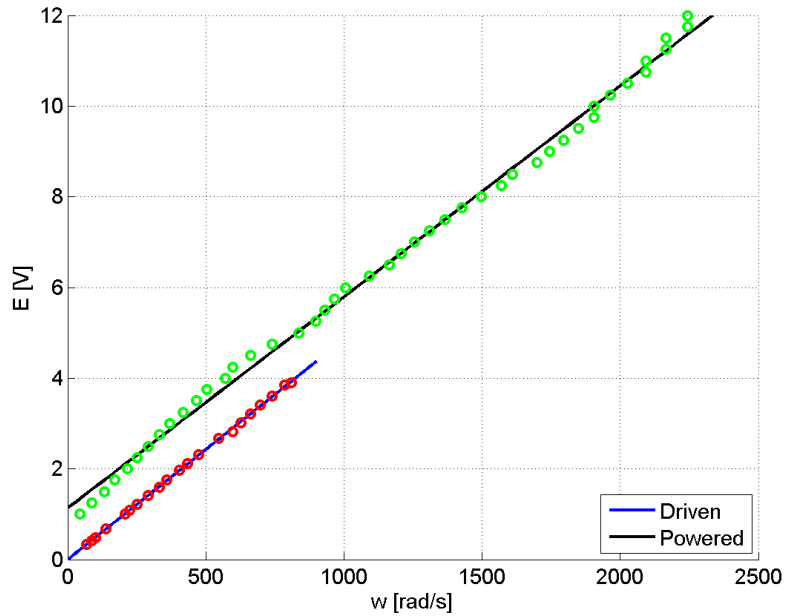


Figure G.6: measuring K_V for powered and driven tests

It can be seen that the slopes differ slightly resulting in

$$k_{V_{powered}} = 0.0055 \quad (\text{G.7})$$

$$k_{V_{driven}} = 0.0049 \quad (\text{G.8})$$

The offset is the armature resistance multiplied by the current from (G.6). In this way the armature resistance can be determined, but for this purpose, functioning as a torque meter, it is not relevant.

The numerical values of the measurements can be found in appendix G.4.

Measuring the drawn current from the DC motor and multiplying with the torque constant will give the applied torque, the DC motor now functions as a torque meter.

G.2.2 Torque measurements

The brush less motor was mechanically connected and powered using a lab power source keeping a constant voltage as shown in figure G.7. To be able to control the applied torque the DC motor was placed in series with a variable resistor. This regulated the amount of torque applied on the motor shaft. When the resistor is set to maximum the

torque applied will be minimal resulting in a very low current through the DC motor. When the resistor is set to minimum, the DC motor is short circuited and therefore maximum torque is applied on the shaft, resulting in high current. The setup is shown in figure G.7.

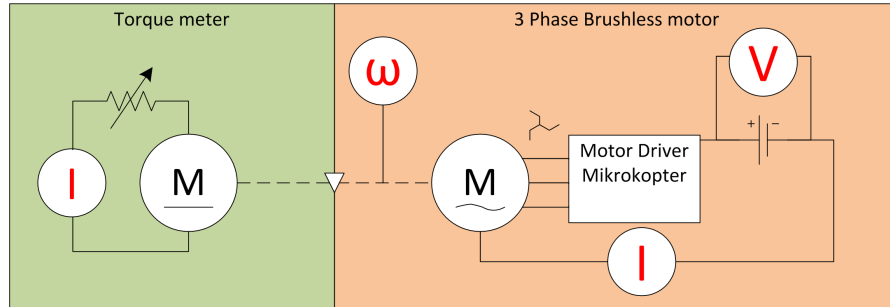


Figure G.7: Setup for measuring motor characteristics

During the test the applied torque was varied using the variable resistor. Then the drawn current I of the lab power source and the rotational velocity ω were measured.

Measuring the drawn current over a brush less AC motor results in practical problems. First of all the drawn current exceeded the fuse limit of 10A of the multimeter.

Therefore an alternative method had to be applied. Using Ohm's law, measuring the voltage and determining its resistance allowed the calculation of the current. To accurately measure this a very low resistance is needed. In this case a cable was taken and the resistance was determined using the reverse method and a lab power source. It resulted in $39\text{m}\Omega$. The final setup used is shown in figure G.8

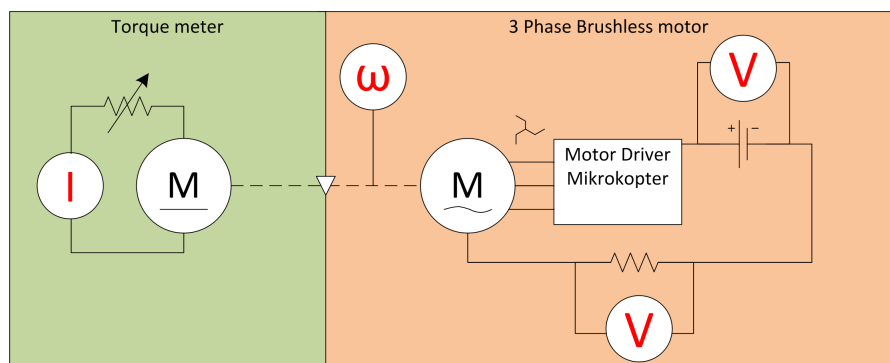


Figure G.8: Final setup for measuring motor characteristics

G.3 Test results

The test results showing the data points and the curve fitting of the two linear relations are shown in figures G.9 and G.10.

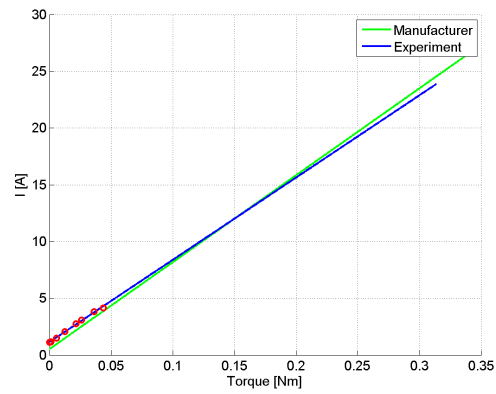


Figure G.9: Results Robbe 2827 torque vs current from test setup

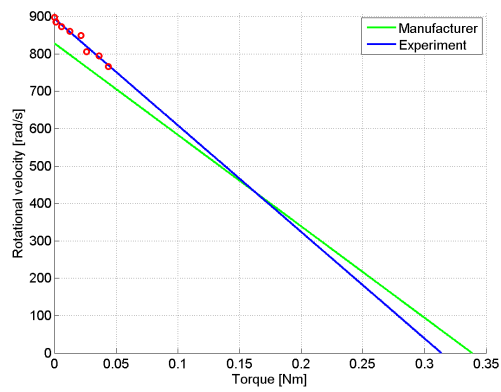


Figure G.10: Results Robbe 2827 torque vs ω from test setup

G.4 Motortest measurements

G.4.1 K_{Tdc}

$E_{induced}$ [V]	ω [rad/s]	I [A]	$E_{induced}$ [V]	ω [rad/s]	I [A]
1	43	0.70	6.75	1208	1.56
1.25	87	0.75	7	1257	1.60
1.5	132	0.78	7.25	1309	1.66
1.75	170	0.80	7.5	1366	1.70
2	217	0.85	7.75	1428	1.68
2.25	251	0.87	8	1496	1.70
2.5	292	0.92	8.25	1571	1.77
2.75	331	0.94	8.5	1611	1.83
3	370	0.99	8.75	1698	1.80
3.25	419	1.02	9	1745	1.83
3.5	465	1.06	9.25	1795	1.80
3.75	503	1.10	9.5	1848	1.80
4	571	1.14	9.75	1904	1.76
4.25	598	1.28	10	1904	1.80
4.5	661	1.21	10.25	1963	1.75
4.75	739	1.31	10.5	2027	1.82
5	838	1.39	10.75	2094	1.80
5.25	898	1.37	11	2094	1.85
5.5	931	1.38	11.25	2167	1.87
5.75	967	1.38	11.5	2167	1.89
6	1005	1.40	11.75	2244	1.90
6.25	1093	1.44	12	2244	1.85
6.5	1164	1.55			

Table G.1: Powered test DC motor

$E_{induced}$ [V]	ω [rad/s]	$E_{induced}$ [V]	ω [rad/s]
0.03	70	2.12	433
0.04	87	2.31	474
0.05	101	2.67	546
0.07	140	2.82	598
1.01	209	3.01	628
1.08	224	3.22	661
1.21	251	3.41	698
1.41	292	3.60	739
1.59	331	3.85	785
1.75	359	3.90	811
1.97	405		

Table G.2: Driven DC motor test for determination of torque constant $K_{T_{dc}}$

G.4.2 Motortest

I_{ac} [A]	ω [rad/s]	I_{dc} [A]	T [Nm]
1.12	898	0	0
1.18	885	0.31	0.0015
1.50	873	1.18	0.0058
2.05	861	2.60	0.0127
2.74	849	4.40	0.0216
3.07	806	5.30	0.0260
3.81	795	7.40	0.0363
4.16	766	8.90	0.0436

Table G.3: Motor characteristics test Roxxy 2827-34 at 12V

Appendix H

Static Thrust MK3638

In this chapter the static thrust is determined for the MK3638 motor. The plotting of the efficiency curve of the MK3638 together with the Robbe Roxxy 2827-34 is shown in figure H.1.

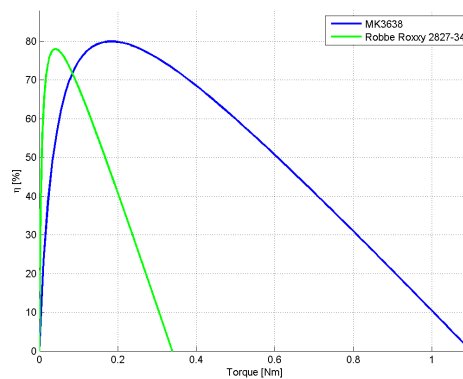


Figure H.1: Efficiency curve for MK3638 and Robbe Roxxy 2827-34

From figure H.1 it can be easily seen that the MK3638 has more power considering applicable torque.

The test data of the propellers [13] covered a maximum rotational velocity of around 628 rad/s (6000 RPM) whereas the MK3638 can reach higher rotational velocities. Investigating the propellers behavior at static suggests that extrapolation is possible. However experiments with higher rotational velocities will have to verify this

The extrapolated coefficients allow for matching the MK3638's torque with the propeller's torque.

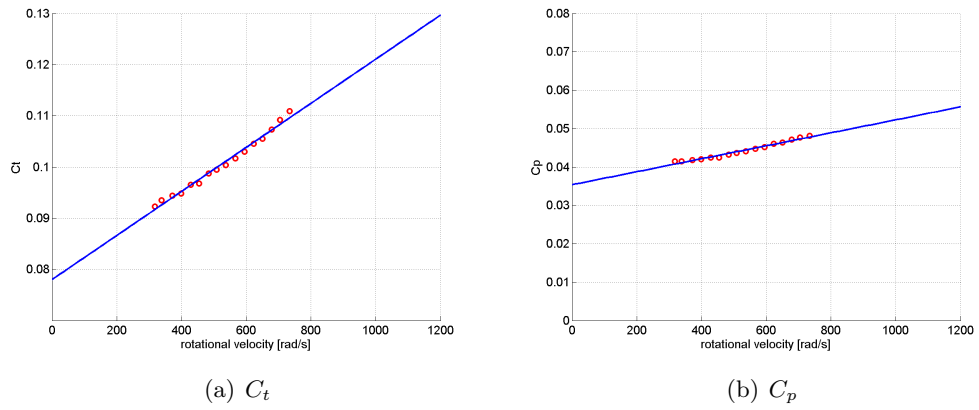


Figure H.2: Extrapolation of C_t and C_p

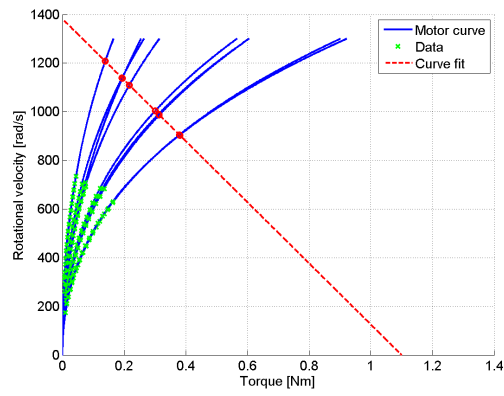


Figure H.3: Static thrust for MK3638

Which result in the following static thrusts:

prop	T [g]
8x3.8	786
8x6	664
9x3.8	1120
9x4.7	1119
9x6	870
10x4.7	1289
10x7	1077
11x3.8	1881
11x4.7	1570

Table H.1: Static thrust with MK3638

H.0.3 Weight estimation

In this section the weight estimation is performed.

The weight of the aircraft consists of different parts:

- W_{struct} = structural weight sometimes referred to as empty weight
- W_p = payload weight
- W_{prop} = propulsion weight
- W_{bat} = battery weight
- W_{sys} = aircraft systems weight

Center of gravity of the plane

The center of gravity of the plane is determined by summing over all the weights of the elements multiplied with their position to a reference point divided over the total weight as can be seen in equation (H.1).

$$\bar{X}_{cog} = \frac{\sum_i^n \bar{X}_i W_i}{\sum_i^n W_i} \quad (\text{H.1})$$

Initial estimation structural weight

The wing is defined as a polygon. The centroid of this polygon is considered the initial estimation of the center of gravity of the empty weight. To determine the centroid of the polygon first the elements are expressed in vectors.

$$X = \begin{bmatrix} x_i & y_i \\ x_{i+1} & y_{i+1} \\ \vdots & \vdots \\ x_{n-1} & y_{n-1} \end{bmatrix} \quad (\text{H.2})$$

Where i is the number of element of the wing. The wing area is estimated using:

$$A = \sum_i^{n-1} (x_i y_{i+1} - x_{i+1} y_i) \quad (\text{H.3})$$

And the centroid is calculated using:

$$x_{cog} = \frac{1}{6A} \sum_i^{n-1} (x_i + x_{i+1}) (x_i y_{i+1} - x_{i+1} y_i) \quad (\text{H.4})$$

$$y_{cog} = \frac{1}{6A} \sum_i^{n-1} (y_i + y_{i+1}) (x_i y_{i+1} - x_{i+1} y_i) \quad (\text{H.5})$$

The wingdesign is taken from the wing optimizer. Since the aircraft is symmetric the value of y_{cog} should be zero. With zero sweep the centroid should be in the middle.

H.1 Drag estimation body

The drag of the body is estimated using the following expression [11]:

$$C_{d_f} = C_f f_{LD} f_M S_b \quad (\text{H.6})$$

- C_f = Skin friction coefficient
- f_{LD} = Fuselage length ratio coefficient
- f_M = Mach number coefficient
- S_b = Wetted area of the body

$$C_f = \frac{1.327}{\sqrt{Re}} \quad (\text{H.7})$$

$$f_{LD} = 1 + 60 \left(\frac{L}{D} \right)^3 + 0.0025 \frac{L}{D} \quad (\text{H.8})$$

$$f_M = 1 - 0.08M^{1.45} \quad (\text{H.9})$$

The wetted area is estimated using the geometry of the body. The length of the arcs of the upper side of the airfoil are multiplied with the spacing between each arc and summed up over the entire wing span. Same is done for the lower side and added to obtain the total wetted area.

- Re = Reynolds number
- L = length of the body
- D = width of the body
- M = Mach number

The Reynolds number is estimated using the following expression:

$$Re = \frac{\rho V L}{\mu} \quad (\text{H.10})$$

$$(\text{H.11})$$

- ρ = density
- V = flight speed
- μ = viscosity

The flight speed has been set to an initial value of 30m/s.

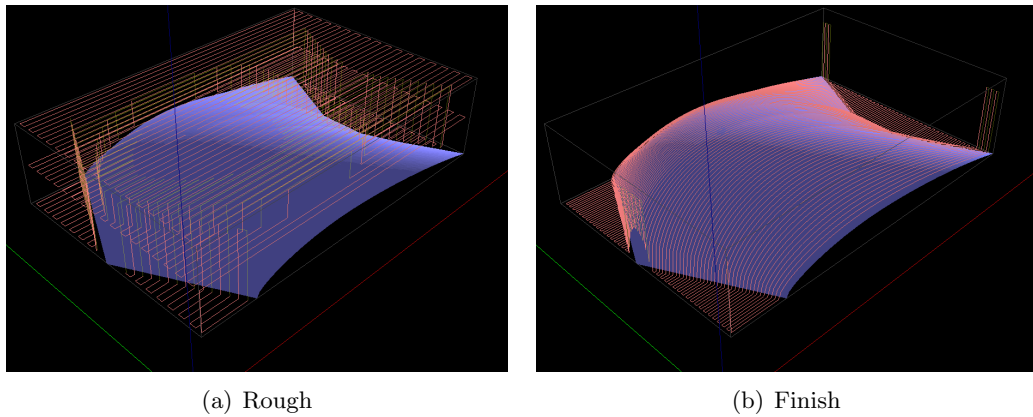


Figure I.2: Tool path for rough and finish milling of the body

In this case the milling process took a long time. Close examine of the g-code revealed that the machines first mills a layer off the complete surface, equaling out the material. However this step is not necessary. Deleting the g-code coordinates for this first layer would significantly reduces the time to produce the rough version.

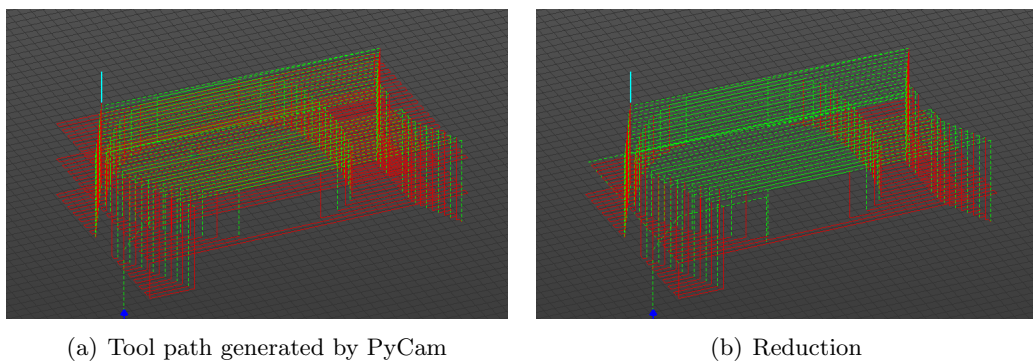


Figure I.3: Tool path reduction

In figure I.3 it can be seen that the top tool path layer is deleted (in red) therefor significantly reducing the duration of the milling.

Appendix J

Log Platform (Flight recorder)

In order to validate the dynamic model experiments have to be carried out. From these experiments flight data is required at high frequencies to cover all the dynamic effects. Think of it as being the 'black box' or flight recorder used in manned aircraft. The manufacturers supply their equipment with tools to log data however it is mostly not possible to use them in flight, or with a cable and do not reach sufficient high logging rates and accuracy. Therefore a platform has to be developed which can do this. After consulting experts, Harm van Gilst and Martijn Roelofs from the aircraft system department (ASAS) it was decided to design a very light separate system which is mounted on the aircraft. This section discusses the design decisions and the interface of this measuring platform. Firstly the appropriate sensors discussed, then the interface and connections are explained.

J.1 Required data

To be able to fully describe the dynamic behavior of the aircraft the following parameters have to be measured.

- Attitude of the aircraft
- position and velocities
- trust of the motors

The attitude of the aircraft will be obtained using an Inertial measurement unit (IMU). This device uses three different sensors to obtain the attitude as well as the angular velocities and body accelerations and is discussed in section J.2. The rotational speed of the rotors are directly linked to the thrust of the aircraft. Finally the barometer gives an indication of the height of the aircraft.

These devices will be discussed in the following sections.

J.2 IMU



Figure J.1: CH Robotics CHR-UM6 IMU

To cover all the dynamics encountered in flight a high update rate of 100Hz has to be maintained. In consultation with the department of aircraft systems ASAS the CHR-UM6 has been chosen and shown in figure J.1. The maximum broadcast rate is 300Hz which is more than enough. The CHR-UM6 contains three different sensors [24].

- Accelerometers
- Magnetometers
- Rate Gyro meters

With these sensors the following parameters can be logged.

- \ddot{X} = accelerations
- Φ = the attitude expressed in euler angles
- $\dot{\Phi}$ = the angular velocities
- Q = the attitude expressed in quaternions

The accelerometers measure the accelerations in the three axis of the body-fixed coordinate system.

$$\ddot{X} = \begin{bmatrix} \ddot{x} \\ \ddot{y} \\ \ddot{z} \end{bmatrix} \quad (\text{J.1})$$

The magnetometers determine the heading with respect to the Earth's magnetic field. It measures the strength of the magnetic field in the three directions. Combined with the other sensors the attitude can be determined accurately.

The gyro meters determine the angular velocities in euler angles.

$$\dot{\Phi} = \begin{bmatrix} \dot{\phi} \\ \dot{\theta} \\ \dot{\psi} \end{bmatrix} \quad (\text{J.2})$$

Combining these three sensors together, the attitude of the aircraft can be obtained in Euler angles and in quaternions. Euler angles are physically easy to interpret whereas quaternions will have mathematical advantages which will become clear in section J.2.6.

$$\Phi = \begin{bmatrix} \phi \\ \theta \\ \psi \end{bmatrix}, Q = \begin{bmatrix} q_1 \\ q_2 \\ q_3 \\ q_4 \end{bmatrix} \quad (\text{J.3})$$

J.2.1 Communication setup

The sensor has to be configured so it broadcasts the desired data and omits sending data which is not required for the attitude determination. The IMU is equipped with a serial interface, referred to as the CH Robotics Interface v2.2.0. This interface is used to configure the IMU. In this interface there is a menu for the configuration of the communication.

The critical points are defined below:

- The broadcast rate is enabled to take advantage of the accurate internal clock of the IMU sending the data at fixed intervals.
- The broadcast rate is set to 73 to match the desired 100Hz update frequency.
- The baud rate is set to its maximum, to ensure the data stream.
- The raw magnetic output is enabled for the magnetometer calibration.
- The processed gyro, accelerations, and magnetometers are enabled.
- Euler angle output and quaternion output is enabled.
- All other outputs are disabled.

The remainder of the communication settings are shown in table J.1.

Communication	value
Broadcast Enabled	1
Broadcast Rate	73
Baud Rate	5
Raw Gyro Output Enabled	0
Raw Accel Output Enabled	0
Raw Mag Output Enabled	0
Processed Gyro Output Enabled	1
Processed Accel Output Enabled	1
Processed Mag Output Enabled	1
Quaternion Output Enabled	1
Euler Output Enabled	1
Covariance Output Enabled	0
Temperature Output Enabled	0
GPS Position Enabled	0
GPS Relative Position Enabled	0
GPS Course/Speed Enabled	0
GPS Satellite Summary Enabled	0
GPS Satellite Data Enabled	0

Table J.1: Communication setup parameters

EKF	value
Mag Variance	2
Acc Variance	2
Process Variance	100

Table J.2: Communication setup parameters

J.2.2 Calibration

To be able to use the IMU and obtain usable data all the sensors have to be calibrated respectively. This will be done for each sensor individually by the test in section J.2.3.

J.2.3 Stationary test

To test the IMU a test run is done by putting the system stationary and measure the outputs of the different sensors. First it should be understood what is to be expected as an outcome of the sensors in this stationary position. Then the output is examined and configured when necessary to match the desired outputs. Possible off-sets are referred to as biases and should be corrected.

Accelerometers

The first sensor which is examined is the accelerometer. In stationary position the measured accelerations in the x and y directions should be zero and the z direction should be -1 which stands for minus one gravity [24]. The accelerations are shown in figure J.2

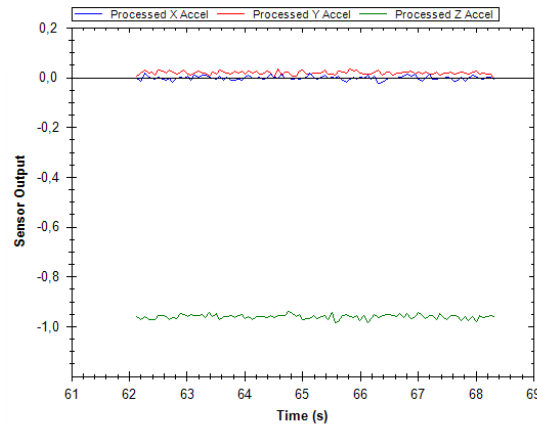


Figure J.2: Measured accelerations in default settings

It can be seen that there exist small biases for the x and y and a larger bias for z . After adjusting the bias parameters the measured accelerations look like in figure J.3.

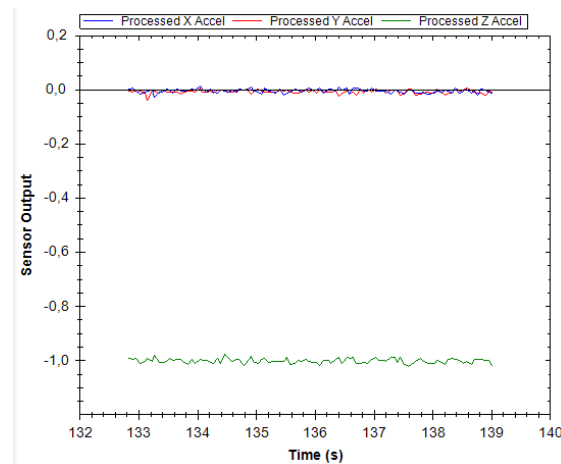


Figure J.3: Accelerations after bias correction

where the bias values are:

$$\ddot{X}_{bias} = \begin{bmatrix} 300 \\ 300 \\ 500 \end{bmatrix} \quad (\text{J.4})$$

It can be seen that the biases have indeed disappeared and the accelerometers are now ready for use.

Gyro

The gyros represent the angular velocities and in stationary position should be zero for roll (ϕ), pitch (θ) and yaw (ψ). The gyro output with the default settings are shown in figure J.4.

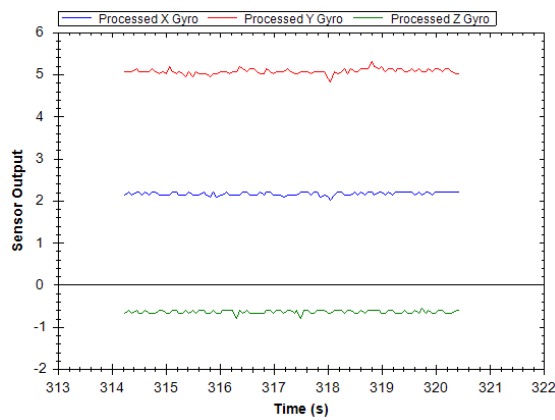


Figure J.4: Angular velocities in default settings

It can be seen that the gyros have large biases and should be adjusted. Using the "zero rate gyros" command in the CHR interface returns them to zero.

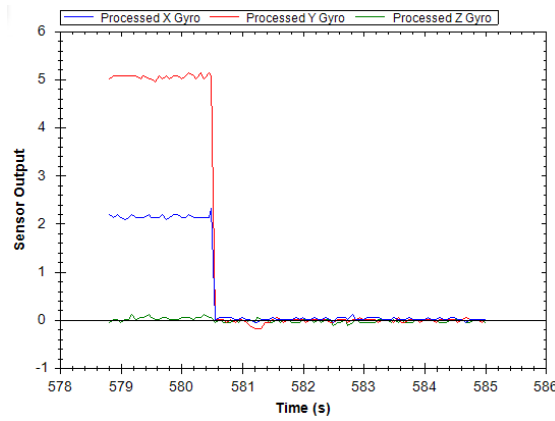


Figure J.5: Angular velocities in default settings

The effect of the zero rate gyros command is clearly visible. Resizing the window gives:

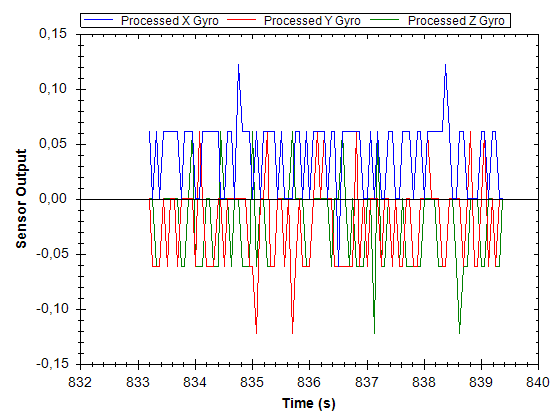


Figure J.6: Angular velocities after zero rate gyros command

The bias values can be read out after the calibration and yield:

$$\dot{\Phi}_{bias} = \begin{bmatrix} 31 \\ 73 \\ -9 \end{bmatrix} \tag{J.5}$$

It can be seen that the it has variations of 0.05 deg per second and peaks of 0.010.

Magnetometer

The magnetometer can be calibrated using the interface. In this calibration test the sensor data is recorded while the sensor is rotated to obtain the Earth's magnetic field.

At least a minimum of 200 points have to be collected before the calibrating can be performed. Moreover when the sensor hasn't covered all possible attitude configurations the calibration cannot be completed, showing an error in the screen.

To verify the consistency of the calibration tool two tests are performed. First the calibration procedure is carried out ten times in exactly the same way. Then the calibration process is done for 30 seconds with more random rotations. The procedure for the first test is given in table J.3.

axis	amount[deg]	direction	time [s]
x-axis	0-360	positive	0-5
x-axis	0-360	negative	5-10
y-axis	0-360	positive	10-15
y-axis	0-360	negative	15-20
z-axis	0-360	positive	20-25
z-axis	0-360	negative	25-30

Table J.3: Calibration method

the results can be seen in figure J.7.

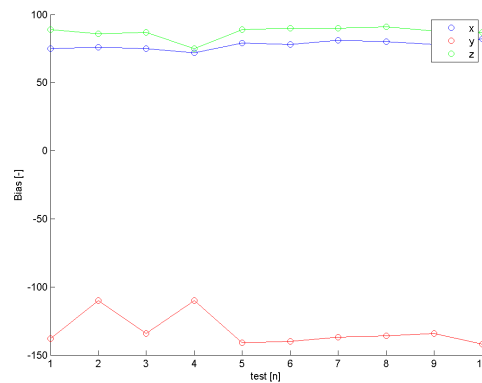


Figure J.7: Bias with equal rotations as calibration method

It shows a small variation in the bias for the x and z , but a larger variation in the first 4 number of tests on the y -axis.

Now the magnetometer is calibrated by rotating the sensor for 30 seconds randomly. The results are shown in figure J.8.

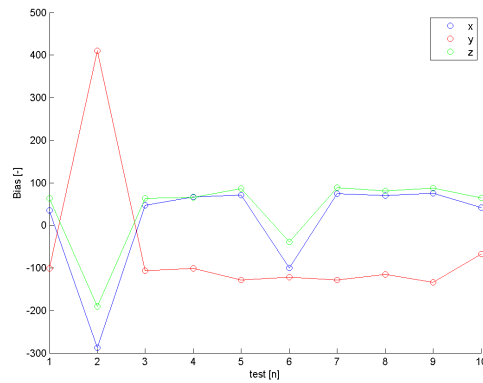


Figure J.8: Bias with random rotations as calibration method

The results show larger variations, however most values come close to the equal rotation method. Test number 2 and 6 are most probable disturbed by an external source and will be declared as a false measurement. Eliminating these two test numbers and taking the average gives a mag bias of:

$$Mag_{bias} = \begin{bmatrix} 70 \\ -122 \\ 82 \end{bmatrix} \quad (J.6)$$

Euler angles

Since all the three sensors have been corrected for there biases the Euler angles can be examined in the current configuration. The sensor is flat on the table, stationary, therefor the roll angle ϕ and the pitch angles θ should be close to zero. The yaw (ψ) depends on its heading compared to the Earth's magnetic field. The Euler angles in the current configuration are shown in figure J.9.

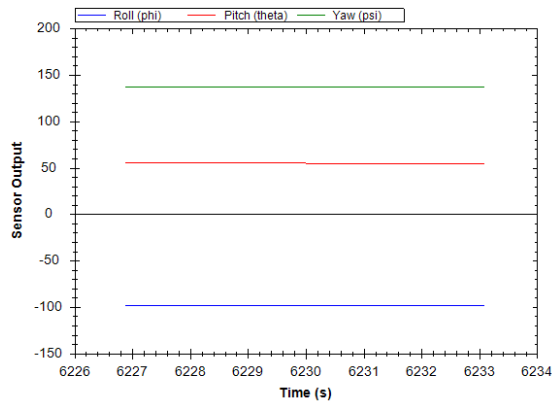


Figure J.9: Euler angles with default settings

Large biases can be seen and have to be adjusted. First the sensor is notified that is in flat position (roll and pitch are zero). This is done by sending the reference vector command for the magnetometer and the accelerometer respectively.

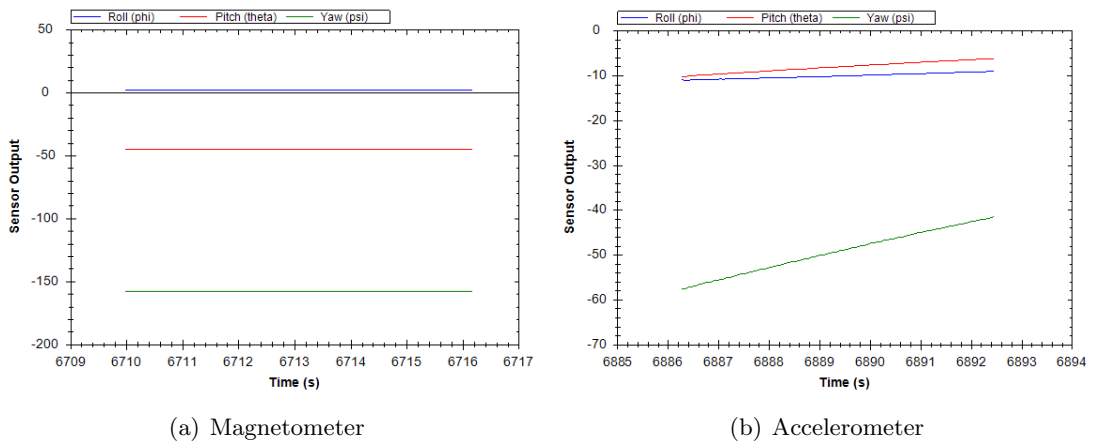


Figure J.10: Euler angles after sending reference vector command

After the magnetometer reference vector command, the Euler angles are offset differently, improving the bias of the roll. However after the accelerometer reference vector command has been sent a strong drift is induced. Waiting for about 100 seconds the Euler angles stabilize as can be seen in figure J.11.

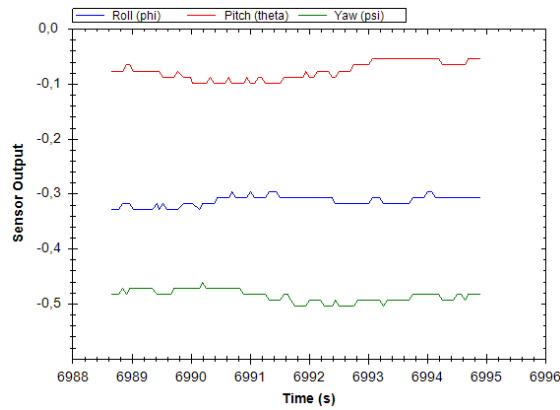


Figure J.11: Bias stabilized after reference vectors commands

This unstable effect should be eliminated and will therefor be investigated further. Keeping the sensor stationary for a longer period provided more insight in the time necessary to stabilize. The results are shown in figure J.12.

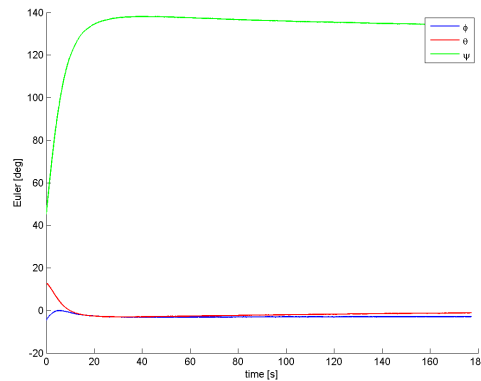


Figure J.12: Attitude in Euler angles in stationary position

It can be seen that the roll and pitch stabilize after about 20 seconds. The yaw angle ψ takes longer to stabilize namely in approximately 60 seconds. It is obvious that this is not acceptable. The Euler angles should stabilize much quicker. After inspection of the manual and contact with the manufacturer it was concluded that the solution could lie tuning in the in-build Extended Kalman Filter (EKF).

J.2.4 EKF tuning

The CHR-UM6 uses an EKF for the processed results. The interface contains three different values to tune. Two measurement noise matrices, one for the accelerometer

and one for the magnetometer, and the process noise matrix. Generally speaking the measurement noise matrices should be kept to factory default.

The process noise matrix is used to specify how much the EKF trusts the gyros with respect to the accelerometers and the magnetometers. Lower values result in trusting the gyros more and higher values will trust the other two sensors more. Which one should be chosen depends on its application.

- trusting gyros increases time-varying gyro output biases increases the DC errors in the angle estimate. This should be used when accelerations are large and interfere with the gravity vector.
- trusting the accelerometers and magnetometers increases the sensitivity of vibrations and distorted magnetic field measurements. This should be used when the platform is more stationary.

The default value EKF process variance value is 0.1 which is very low, therefore trusting the gyros more. The relatively small drift in the gyros could be the cause of the drift in the yaw axis of the Euler angles.

Setting the EKF process to higher value in this case 100, the stationary test is done again.

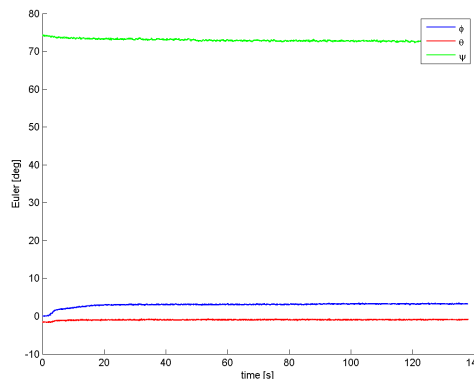


Figure J.13: Attitude in euler angles in stationary position with EKF tuning

It can be seen that the angles indeed stabilize much quicker. Hence it important to find the right value for this parameter.

J.2.5 Checklist IMU

To perform a accurate measurement the following checklist has to be followed. Using the CHR serial interface, in the menu: "Commands".

Commands	
1	Zero Rate Gyro
2	Set Accelerometer Reference Vector
3	Set Magnetometer Reference Vector
Checks	
4	Check if gyros are zero see figure J.6
5	Check if acc are $[0 \ 0 \ -1]$ see figure J.3
6	Check if euler angles are $[0 \ 0 \ \psi]$ see figure J.11
7	Check for drift of euler angles, if so check EKF setting

Table J.4: Checklist before measurements

J.2.6 Train test

In this section the IMU is put to the test. It is subjected to a known environment in this case a train is ran several laps along a track. The IMU-device is mounted on the train which is first accelerated after it runs several laps with constant speed, finally decelerating till a hold. Like as done before first the system is examined to determine what output is expected. Then the measurements are compared with this expected output.

The setup can be seen in figure J.14. It consists of a two circular parts and two straight parts. The train is controlled by a transmitter and is powered by an electric motor.



Figure J.14: Train experiment setup

It was discovered that the trains receiver and electric motor distorted the magnetic field affecting the measurements heavily. Therefore the sensor has been moved to a wagon behind the locomotive.

Accelerations

The accelerations in the x-direction should be around zero since it does not accelerate along the track. However when hitting the corner the train experiences more resistance of the track resulting in a slight deceleration which would be restored on the straight part. In the corners the train experience centrifugal forces resulting in accelerations in the y-direction, which return to zero on the straight part of the lap. The z-direction should be more or less constant around -1 gravity. The results are shown in figure J.15.

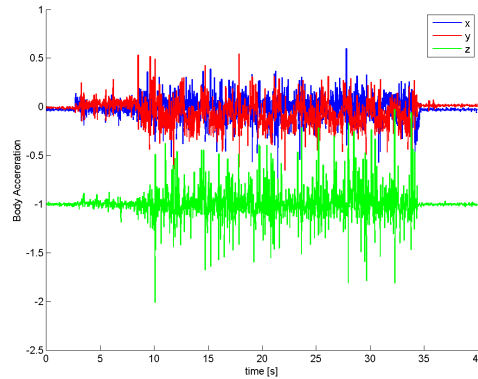


Figure J.15: Accelerations in the body fixed frame of the train test

It can be seen that the signal is very noisy, therefore a low pass filter was applied. To determine the cut-off frequency of the low pass filter the signal was transformed into the frequency domain using Fast Fourier Transform (FFT) which is shown in figure J.16.

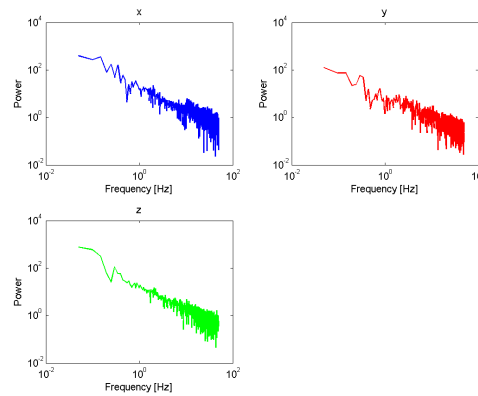


Figure J.16: FFT of the accelerations

Due to the low accelerations in the x and z direction the FFT mainly contains noise.

The main accelerations are in the y-direction it can be seen that most power is at lower frequencies. A cut-off frequency of 8 Hz has been chosen and is shown in figure J.17

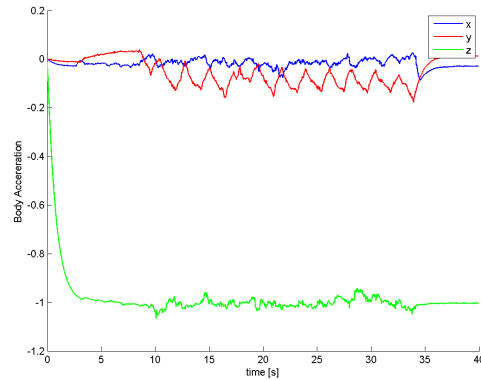


Figure J.17: Accelerations with a low pass filter

The signal is much clearer now and the measured data fits the expected profile. Note the effect of the filter at the beginning of the signal where the z-axis starts at zero and needs time to stabilize at -1 gravity. Furthermore the fluctuations in the z-axis are more than expected.

Euler angles

The expected Euler angles are zero for the pitch and roll whereas the yaw should turn 180 degrees at each turn. The results are shown in figure J.18.

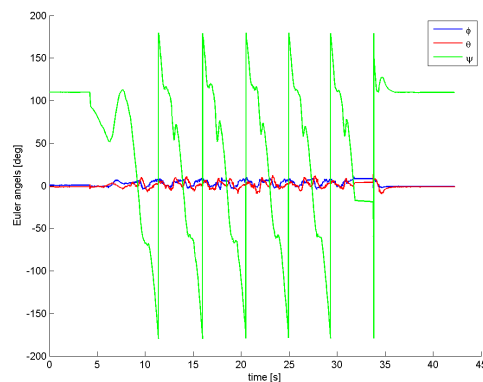
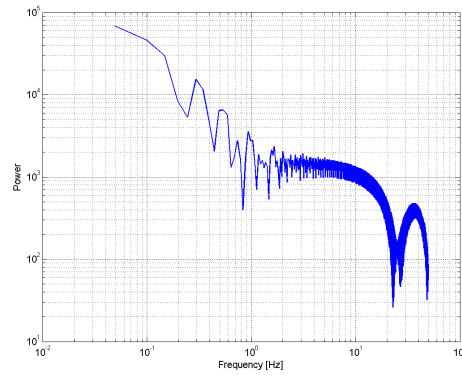


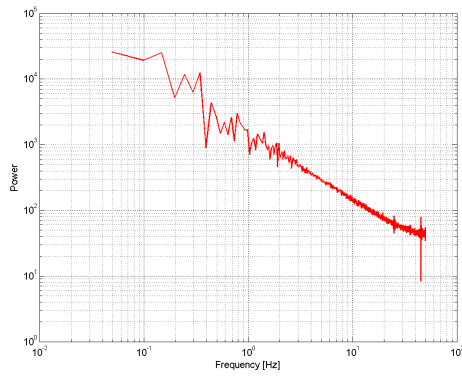
Figure J.18: Euler angles of the train running on a track

This signal should be filtered as well. The FFTs of the Euler angles are shown in

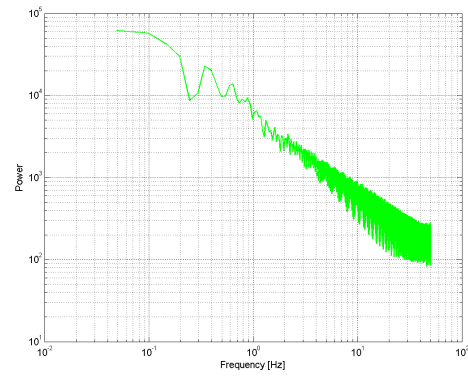
figure J.19



(a) Roll



(b) Pitch



(c) Yaw

Figure J.19: FFT of Euler angles

It can be seen that the power of the signal goes from 10^2 to 10^0 at frequencies below 10 Hz for the roll and in 5 Hz for pitch and yaw. Applying the filter at 10 Hz gives:

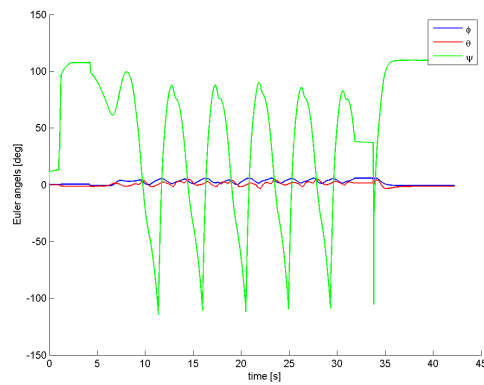


Figure J.20: Euler angles with a low pass filter

The filtered signal works fine for the roll and pitch angles, ϕ and θ but shows undesired behavior for the yaw. The peaks are being cut off which is not acceptable. Therefore a different representation should be examined, quaternions.

The quaternions are shown in figure J.21

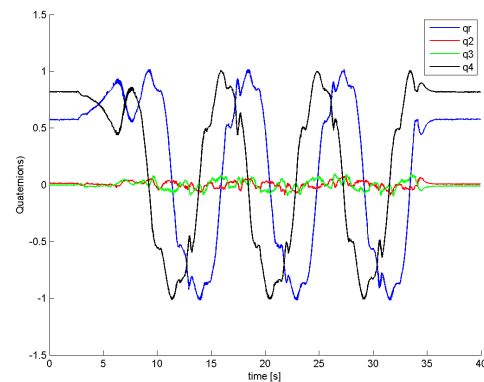
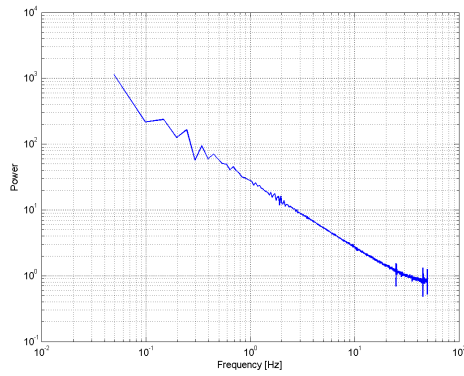
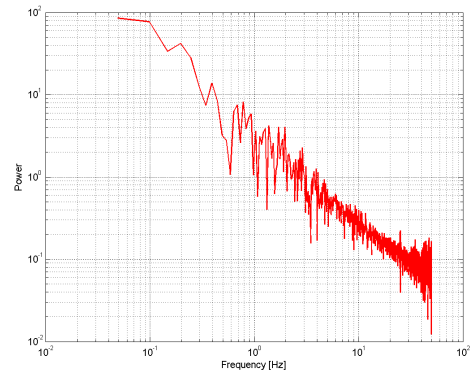


Figure J.21: Quaternion representation of the train test

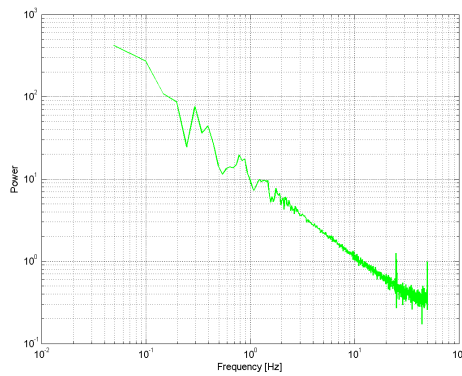
It can be seen that the quaternions do not experience this jump from -180 degrees to 180, which means this signal can be filtered without artifacts. Determining the cut-off frequency was again done by examining the FFTs.



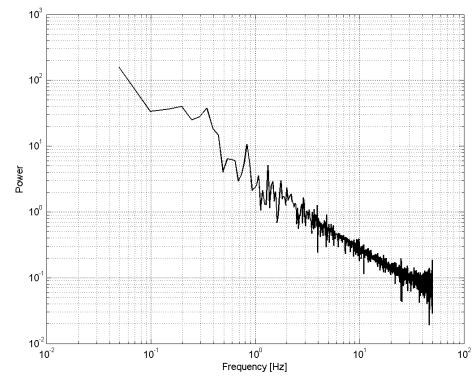
(a) Q1



(b) Q2



(c) Q3



(d) Q4

Figure J.22: FFT of quaternions

It can be seen that a cut-off frequency of 10 Hz covers most of the power of the signal. Applying the filter to the quaternions is shown in figure J.23.

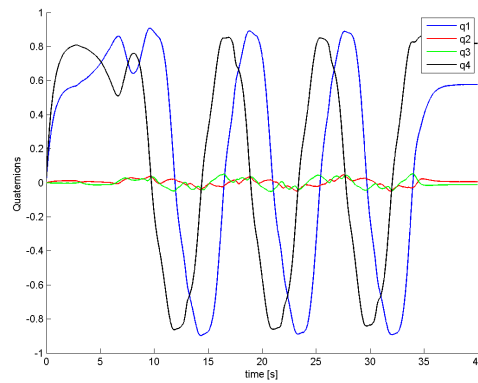


Figure J.23: Quaternion representation with low pass filter

The signal is much smoother and using this filtered signal the quaternions can be transformed back into Euler angles as shown in figure J.24

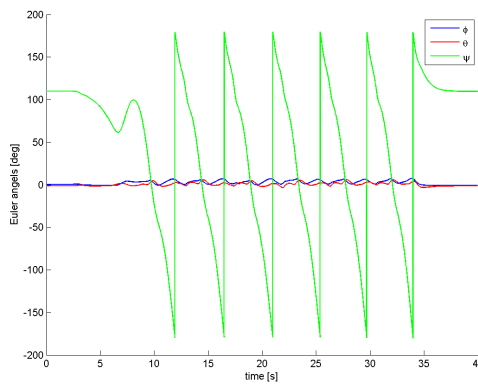


Figure J.24: Euler angles using filtered signal of quaternions

The signal is much smoother than figure J.18 but does not suffer from the same artifacts when the filter is applied directly to the Euler angles.

Position estimation

From the accelerations it is possible to estimate the position [17]. First the accelerations are transformed into the inertial frame and gravity should be deducted. Furthermore these inertial accelerations are integrated twice to obtain a position estimation. Transforming the body frame to the inertial frame:

$$\mathbf{a}_I = R_B^I \mathbf{a}_m + \begin{bmatrix} 0 \\ 0 \\ g \end{bmatrix} \quad (\text{J.7})$$

- R_B^I = the rotation matrix from the body to inertial frame
- \mathbf{a}_m = measured accelerations
- \mathbf{a}_I = inertial accelerations

The rotation matrix is obtained from [17] and depend on the attitude of the sensor, equivalently the Euler angles.

Since the sensor sends data at discreet intervals the integration is done by simply applying:

$$v_{i+1} = v_i + a_i \partial t \quad (\text{J.8})$$

$$s_{i+1} = s_i + v_i \partial t \quad (\text{J.9})$$

Applying this to the train test the velocities are shown in figure J.25.

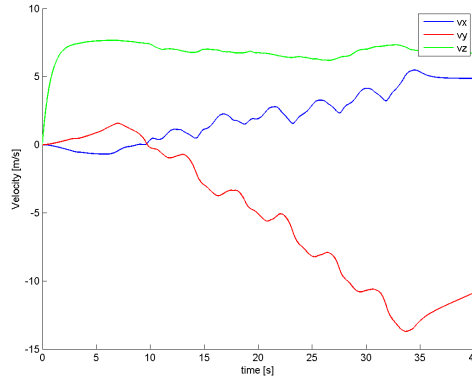


Figure J.25: Velocity estimates obtained from accelerations

It can be seen that the velocities quickly spin out of control. When integrating again the positions are obtained.

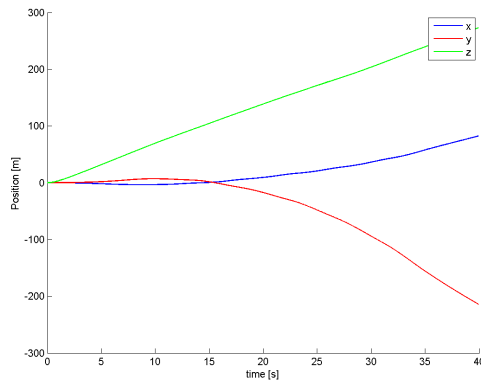


Figure J.26: Position estimates obtained from accelerations

It can be concluded that in this configuration, estimating the position is not possible.

J.2.7 delay

It is known that the clock of the IMU is accurate, hence when set at a broadcast rate of 73 it can be assumed that the frequency is 100.1569Hz or an interval δt of 0.009984 seconds. A time vector can be defined using this interval.

$$t = t_{start} : \delta t : t_{end} \tag{J.10}$$

To examine if delay exists a time stamp is added when a package is processed. Plotting IMU data with both time vectors.

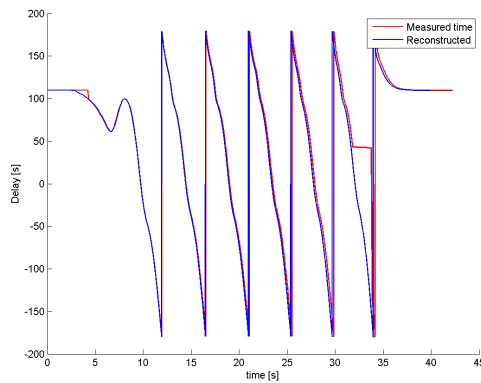


Figure J.27: Euler angle ϕ of the train with both time vectors

In figure J.27 it can be seen that the graphs do not match perfectly meaning that delay exists. Moreover it can be seen that the delay increases with time. This implies

the RAM is increasingly filled with unprocessed data. To obtain the magnitude of the delay the internal interval is subtracted from the timestamp and plotted in figure J.28.

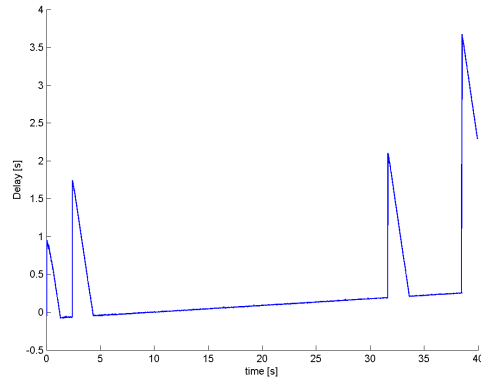


Figure J.28: Delay vs time

It can be seen that the time linearly increases with time, this confirms that the processing time is relatively constant. The peaks are due to other applications running at the same time and demanding CPU power. This illustrates how important it is to shut all other applications when logging. The peaks reflect the horizontal parts of the measured time in J.28. This is caused by another program running in the background. An easy solution was to use the created time vector to correct for the time delay using the known time. It has to be kept in mind that the program has to run long enough after the measurement to process all the data in the buffer.

J.3 Altitude

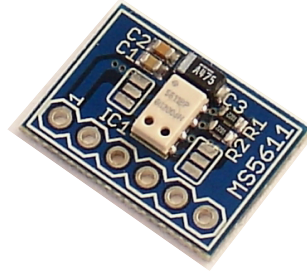


Figure J.29: The MS5611 Barometer [7]

The altitude is measured using an independent barometer. The barometer including the board can be seen in figure J.29. This device measures the temperature and the local pressure. The relation of the the pressure temperature and altitude is shown below [25]. The full derivation is given in appendix J.5.

$$z = \frac{T_0}{L} \left(\left(\frac{P(z)}{P_0} \right)^{\frac{-LR}{g}} - 1 \right) \quad (\text{J.11})$$

- $P(z)$ = Pressure at altitude [Pa]
- P_0 = Pressure at zero height [Pa]
- T_0 = Temperature at zero height [Pa]
- z = altitude [m]
- L = lapse rate, -0.0065 [K/m]
- R = gas constant for air, 287.053 [j/kgK]
- g = gravitational acceleration, 9.81 [m/s²]

J.3.1 Test

The MS5611 was put to the test. The first the temperature and pressure were measured during ten minutes (600 seconds) at stationary. In theory the temperature and pressure should be constant since the sensor remains in stationary position. The results are shown in figure J.30 and J.34.

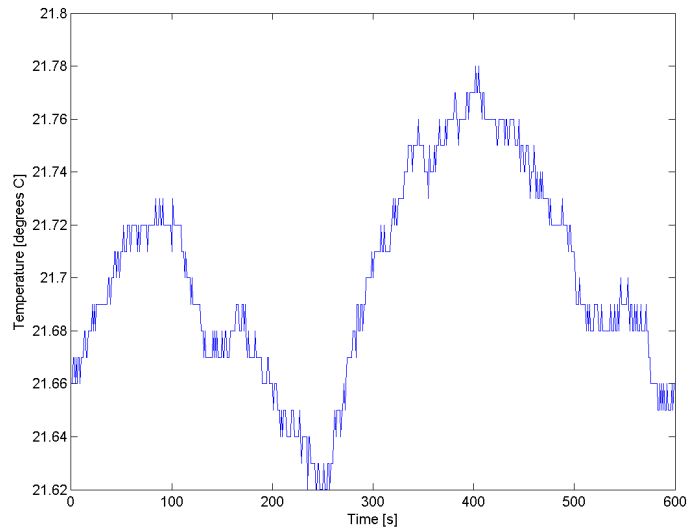


Figure J.30: Temperature measurement from MS5611

It can be seen that the temperature does vary slightly over time with the difference of the maximum value and minimum value being only $0.16\text{ }^{\circ}\text{C}$. The variance to mean ratio is $6.8924 \cdot 10^{-5}$.

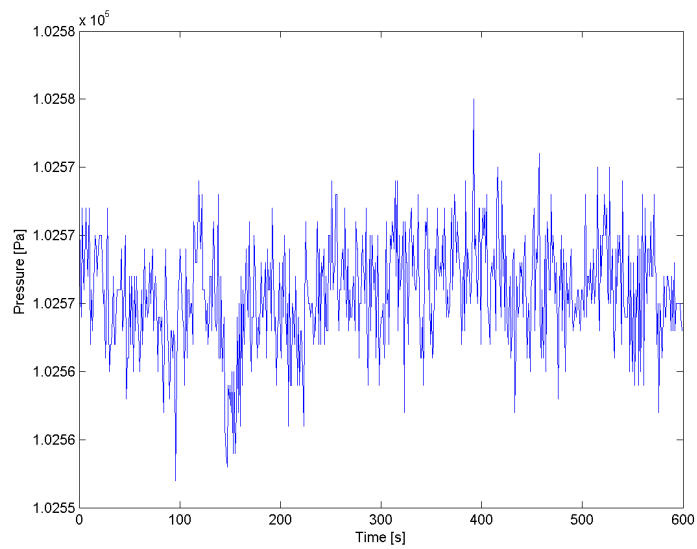


Figure J.31: Pressure measurement from MS5611

Temperature and the pressure remains constant with a difference of only 26 Pa compared with the average of $1.0256 \cdot 10^5$ resulting in a variance to mean ratio of $1.5309 \cdot 10^{-4}$.

When setting the mean of the the pressure as the pressure at zero height, the altitude is calculated with equation (J.11) and shown in figure J.35.

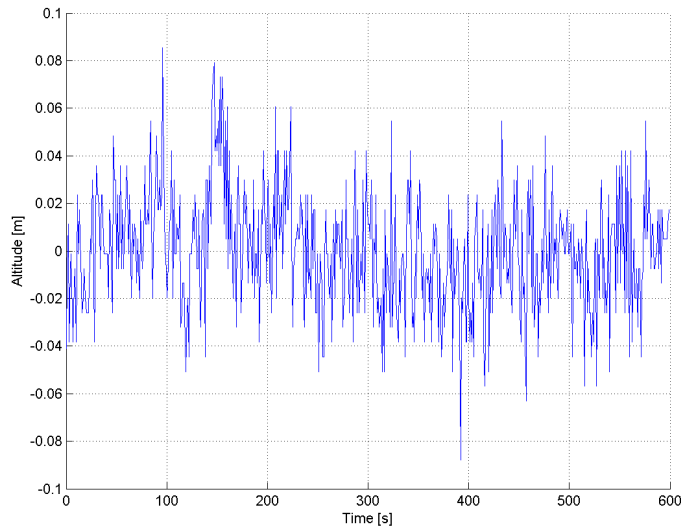


Figure J.32: Altitude measurement from MS5611

J.3.2 Height test

The barometers was put to the test again. First the raspberry PI was connected to a battery using a voltage converter to make it mobile.

The raspberry PI including the barometer is stationed at different heights using a closet. The shelves in the closets have different heights and are shown in figure J.33.

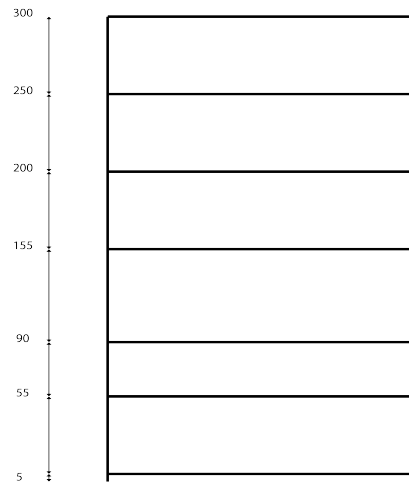


Figure J.33: The height of the shelves of the closet

First the barometer is stationed at for 30 seconds at every shelf starting from the bottom to the top and back again. This sequence was repeated once. The results are shown in figure J.34.

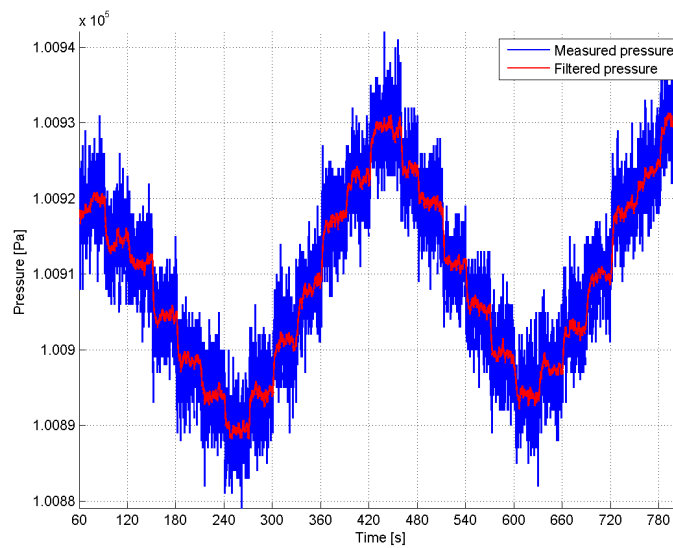


Figure J.34: The measured pressure during the heighttest. NOTE the test starts at $t = 60$ to let the barometer stabilize before the test

First the zero pressure has to be defined. This is the pressure measured at the lowest shelf which is located at $y = 0.05$ m. The sensor is stationed at this zero height three

times, at $t = [60\ 90]$, $t = [420\ 450]$, $t = [780\ 810]$. The second and third match relatively well, hence it was decided to take the mean of those periods and set it as the pressure on zero height, which resulted in $P_0 = 1.0092421 \cdot 10^5$. Using expression (J.11) the altitude was calculated and shown in figure J.35.

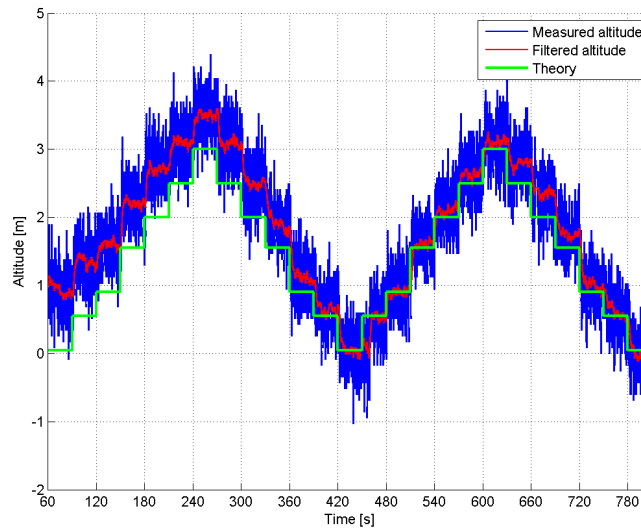


Figure J.35: Heighttest: the test starts at $t = 60$ to let the barometer stabilize before the test

It can be seen that setting the zero height pressure resulted in zero height at the lowest shelf at $t = [420\ 480]$ and $t = [780\ 810]$. The reference of the graph is set to the floor, 5 centimeters lower than the lowest shelf. In the second sequence the barometer matches the real height relatively well, however it does seem to have trouble on the way down at 2.5 and 2 meters height. It does finish at the same zero height as in the start of the second sequence.

J.4 Noise

From the graphs J.34 and J.35 it can be seen that the noise is relatively large. After consultation with Martijn Roelofs the suspicion raised that it might have been caused by the power supply of the Raspberry PI which fluctuates more than it should do. Therefore the barometer was powered by a Lab Power device shown in figure J.36.



Figure J.36: Lab Power Device [8]

Both power sources are compared:

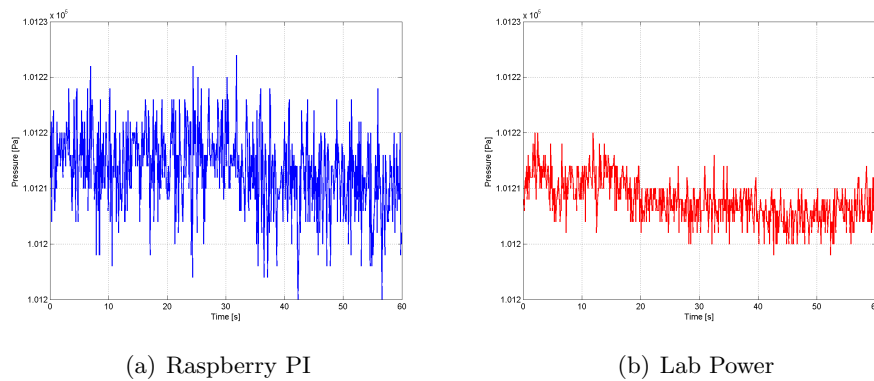


Figure J.37: Noise comparison with different power sources

Using a more stable power source did significantly reduced the noise in the signal.

J.5 Altitude derivation for baro meter

Using hydrostatic equilibrium where an infinitesimal change in pressure must oppose the gravitational force over that infinitesimal layer.

$$\frac{dP}{dz} = -\rho g \quad (\text{J.12})$$

- P = pressure [Pa]
- z = altitude [m]
- ρ = air density [kg/m^3]
- g = gravitational acceleration, 9.81 [m/s^2]

Including the ideal gas law:

$$P = \rho RT \quad (\text{J.13})$$

- R = gas constant for air, 287.053 [j/kgK]
- T = temperature [K]

Combining both (J.12) and (J.13) gives:

$$\frac{dP}{dz} = -\frac{g}{RT}P \quad (\text{J.14})$$

Taking temperature as a function of the altitude z a non-linear differential equation is obtained:

$$\frac{dP(z)}{dz} = -\frac{g}{RT(z)}P(z) \quad (\text{J.15})$$

Rewriting for integration:

$$\int_{P_0}^{P(z)} \frac{1}{P(z)} dP(z) = -\frac{g}{R} \int_0^z \frac{1}{T(z)} dz \quad (\text{J.16})$$

where $P(0) = P_0$.

Applying the integration for the left side:

$$\int_{P_0}^{P(z)} \frac{1}{P(z)} dP(z) = \ln(P(z) - P_0) \quad (\text{J.17})$$

$$= \frac{\ln(P(z))}{\ln(P_0)} \quad (\text{J.18})$$

For the right side of equation (J.15) the temperature has a constant lapse rate L , hence T as a function of z becomes:

$$T(z) = T_0 + Lz \quad (\text{J.19})$$

- L = lapse rate, -0.0065 [K/m]

Integrating gives:

$$\int_0^z \frac{1}{T_0 + Lz} dz = \frac{1}{L} (\log(T_0 + Lz) - \log(T_0)) \quad (\text{J.20})$$

gives

$$\int_0^z \frac{1}{T(z)} dz = \int_0^z \frac{1}{T_0 + Lz} dz \quad (\text{J.21})$$

Expanding the logarithmic terms:

$$\log(T_0 + Lz) = \log(T_0) + \log\left(\frac{Lz}{T_0} + 1\right) \quad (\text{J.22})$$

substituting in (J.20) yields:

$$\int_0^z \frac{1}{T_0 + Lz} dz = \frac{1}{L} \left(\log\left(\frac{Lz}{T_0} + 1\right) \right) \quad (\text{J.23})$$

Substituting the integrals back into (J.16)

$$\frac{\ln(P(z))}{\ln(P_0)} = -\frac{g}{R} \frac{1}{L} \left(\log\left(\frac{Lz}{T_0} + 1\right) \right) \quad (\text{J.24})$$

$$\ln P(z) = -\ln(P_0) \frac{g}{R} \frac{1}{L} \left(\log\left(\frac{Lz}{T_0} + 1\right) \right) \quad (\text{J.25})$$

Applying logarithm on both sides

$$P(z) = P_0 \exp\left(-\frac{g}{R} \frac{1}{L} \left(\log\left(\frac{Lz}{T_0} + 1\right) \right)\right) \quad (\text{J.26})$$

Using

$$\exp(ab) = \exp(a)^b \quad (\text{J.27})$$

with

$$a = \log\left(\frac{Lz}{T_0} + 1\right) \quad (\text{J.28})$$

$$b = -\frac{g}{RL} \quad (\text{J.29})$$

Applying (J.27) to (J.26) gives:

$$P(z) = P_0 \exp\left(\log\left(\frac{Lz}{T_0} + 1\right)\right)^{-\frac{g}{RL}} \quad (\text{J.30})$$

Rewriting for z :

$$P(z) = P_0 \left(\frac{Lz}{T_0} + 1 \right)^{-\frac{g}{RL}} \quad (\text{J.31})$$

$$\frac{P(z)}{P_0} = \left(\frac{Lz}{T_0} + 1 \right)^{-\frac{g}{RL}} \quad (\text{J.32})$$

$$\frac{P(z)^{-\frac{RL}{g}}}{P_0} = \left(\frac{Lz}{T_0} + 1 \right) \quad (\text{J.33})$$

$$\left(\frac{Lz}{T_0} + 1 \right) = \frac{P(z)^{-\frac{RL}{g}}}{P_0} \quad (\text{J.34})$$

$$\frac{Lz}{T_0} + 1 = \frac{P(z)^{-\frac{RL}{g}}}{P_0} \quad (\text{J.35})$$

$$\frac{Lz}{T_0} = \frac{P(z)^{-\frac{RL}{g}}}{P_0} - 1 \quad (\text{J.36})$$

$$z \left(\frac{L}{T_0} \right) = \frac{P(z)^{-\frac{RL}{g}}}{P_0} - 1 \quad (\text{J.37})$$

$$(\text{J.38})$$

Finally gives:

$$z = \frac{T_0}{L} \left(\left(\frac{P(z)}{P_0} \right)^{-\frac{RL}{g}} - 1 \right) \quad (\text{J.39})$$

J.6 RPM measurements

To measure the rpm of the engines the Eagle Tree Brushless RPM sensor was used. This sensor was connected directly to different polarities of the brushless motor. It measures the pulses of which the rpm could be derived. To obtain the rpm the number of poles need to be known.

J.6.1 Square wave test

First the working principle of the RPM sensors is tested using a function generator J.38.



Figure J.38: Function generator [9]

A square wave of 100Hz is generated and connected to the rpm sensor to see if it measures the signal up the signal. The signal was measured with an oscilloscope where the output was shown in figure J.39.

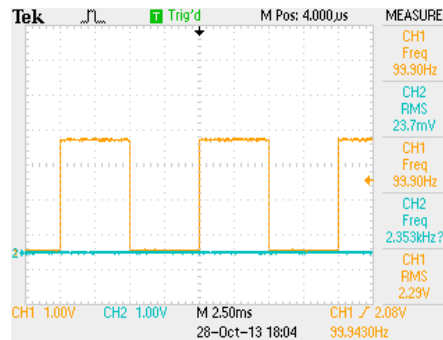
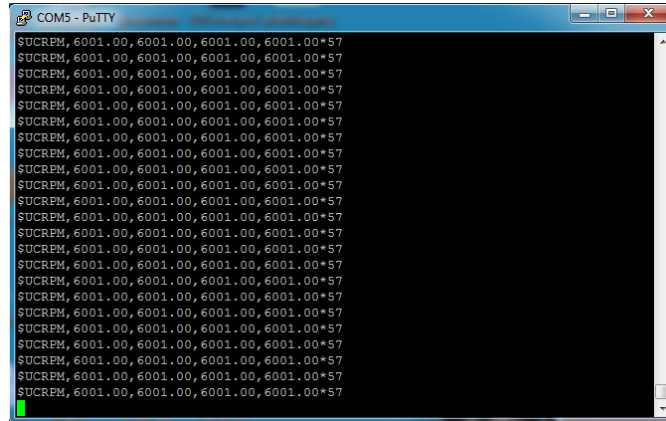


Figure J.39: Output of the function generator shown on channel 1

The RPM sensor measures "Rounds Per Minute", whereas the frequency generator outputs in frequency (Hz). Hence a frequency of 100 Hz would result in:

$$100 \cdot 60 = 6000 \text{ rpm} \quad (\text{J.40})$$

As a check the program only works when all four inputs are connected. Therefore the frequency generator's signal is connected to all four inputs simultaneously. When the RPM sensor is connected it gives the following output:



```
COM5 - PuTTY
SUCRPM, 6001.00, 6001.00, 6001.00, 6001.00*57
SUCRPM, 6001.00, 6001.00, 6001.00, 6001.00*57
SUCRPM, 6001.00, 6001.00, 6001.00, 6001.00*57
SUCRPM, 6001.00, 6001.00, 6001.00, 6001.00*57
SUCRPM, 6001.00, 6001.00, 6001.00, 6001.00*57
SUCRPM, 6001.00, 6001.00, 6001.00, 6001.00*57
SUCRPM, 6001.00, 6001.00, 6001.00, 6001.00*57
SUCRPM, 6001.00, 6001.00, 6001.00, 6001.00*57
SUCRPM, 6001.00, 6001.00, 6001.00, 6001.00*57
SUCRPM, 6001.00, 6001.00, 6001.00, 6001.00*57
SUCRPM, 6001.00, 6001.00, 6001.00, 6001.00*57
SUCRPM, 6001.00, 6001.00, 6001.00, 6001.00*57
SUCRPM, 6001.00, 6001.00, 6001.00, 6001.00*57
SUCRPM, 6001.00, 6001.00, 6001.00, 6001.00*57
SUCRPM, 6001.00, 6001.00, 6001.00, 6001.00*57
SUCRPM, 6001.00, 6001.00, 6001.00, 6001.00*57
SUCRPM, 6001.00, 6001.00, 6001.00, 6001.00*57
SUCRPM, 6001.00, 6001.00, 6001.00, 6001.00*57
SUCRPM, 6001.00, 6001.00, 6001.00, 6001.00*57
SUCRPM, 6001.00, 6001.00, 6001.00, 6001.00*57
```

Figure J.40: Output RPM sensors at a 100Hz square wave

Hence the RPM sensor gives the correct output for a square wave input, which is the same for all four inputs.

J.6.2 Motor test

The RPM sensor works correctly for the square wave, hence was put to the test with a real motor. The flight tests were performed by the Quad of Mikrokopter which is equipped with four Robbe 2827-34 outrunners.

The real RPM of the engines is given by:

$$RPM_{real} = \frac{RPM_m}{n_{poles}} \quad (J.41)$$

- RPM_m = measured RPM [rounds/minute]
- n_{poles} = number of poles [-]

J.6.3 Rotational velocity

For the rotational velocity measurements the same Eagle Tree rotational velocity sensors are used for the log platform. First the number of poles of the brushless electric motor needs to be determined. As indicated by the manufacturer the motor has 14 poles. However the configurations of the poles determines the number of magnetic poles. To verify this the rotational velocity was measured using an alternative method, using a LED and a sensor from a fire alarm and a transparent circular piece of plastic with a marker.

When the marker interrupted the light a voltage drop showed on the oscilloscope. Measuring the interval between two sequential drops is the equivalent of one period of the rotation. Comparing the results it can be concluded that the brush less motors have 7 magnetic poles.

To protect the sensor from an optocoupler is used. This enables signal transmission while separating the electric signal. A resistor is added to admit the high enough input voltage.

J.7 Interface

To collect all the data the motherboard was selected, namely the Raspberry Pi Model B. This is a small but very powerful mini-computer. It runs on Raspbian which is Linux based. The different sensors will be connected using the scheme shown in figure J.41.

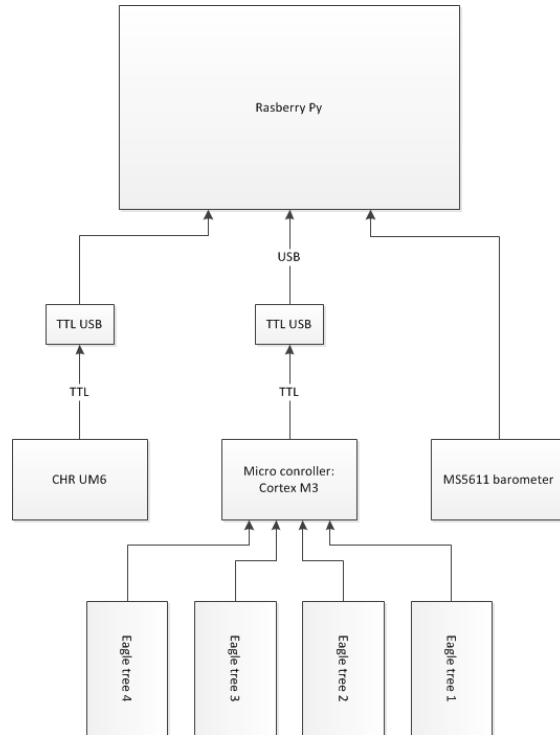


Figure J.41: Layout of the sensors connected to the Raspberry PI

To make the complete package compact a circuit board was designed. This circuit board was designed by Aran Dokoupil a student of electrical engineering.

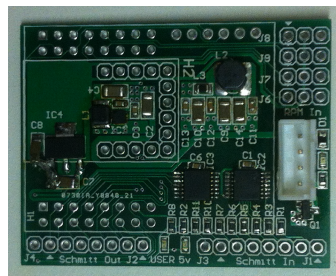


Figure J.42: Circuit board with the components

The board contains two Schmitt triggers in case the flanks of the signal of the motors are not steep enough. Furthermore a voltage regulator and a coil were added to the circuit. After the headers are soldered the Pololu UART to usb converter can be incorporated.

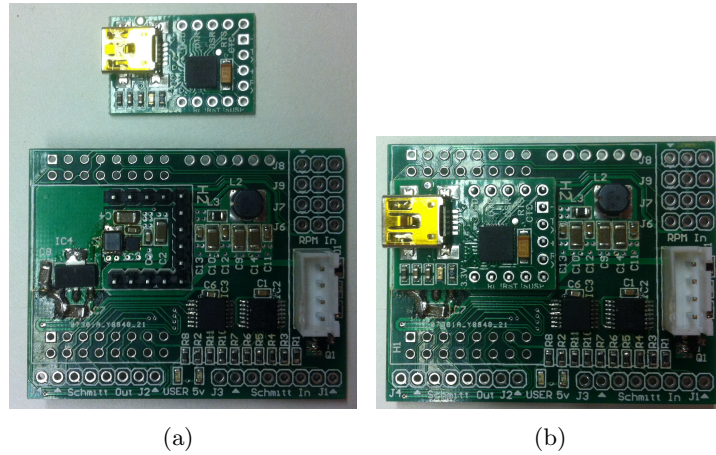


Figure J.43: The Pololu USB connector incorporated in the circuit board

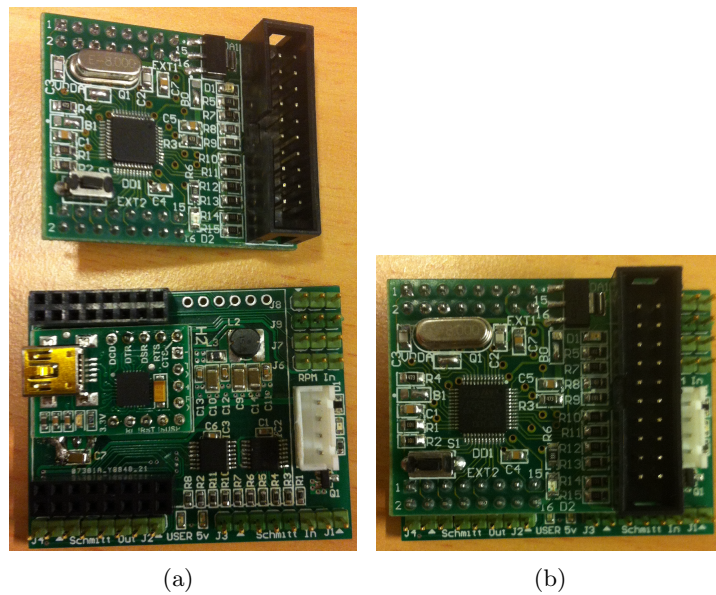


Figure J.44: The Cortex μ C incorporated the circuit board

Connecting the circuit board to with the USB for data connection and with the charger cable of the battery to power the system up.

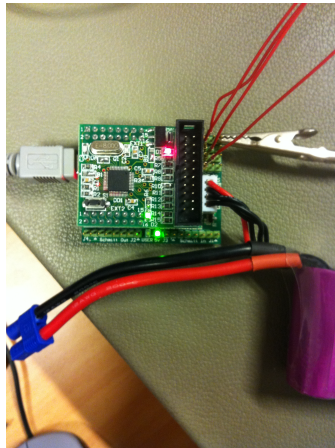


Figure J.45: Circuit board powered up and functional

In figure J.45 the system is powered up and connected with USB. The RPM sensors are simulated with the function generator for testing purposes like the test in section J.6.1

A JAVA program is written to read and log the data from the CMU. The layout of the program can be seen in figure J.46.

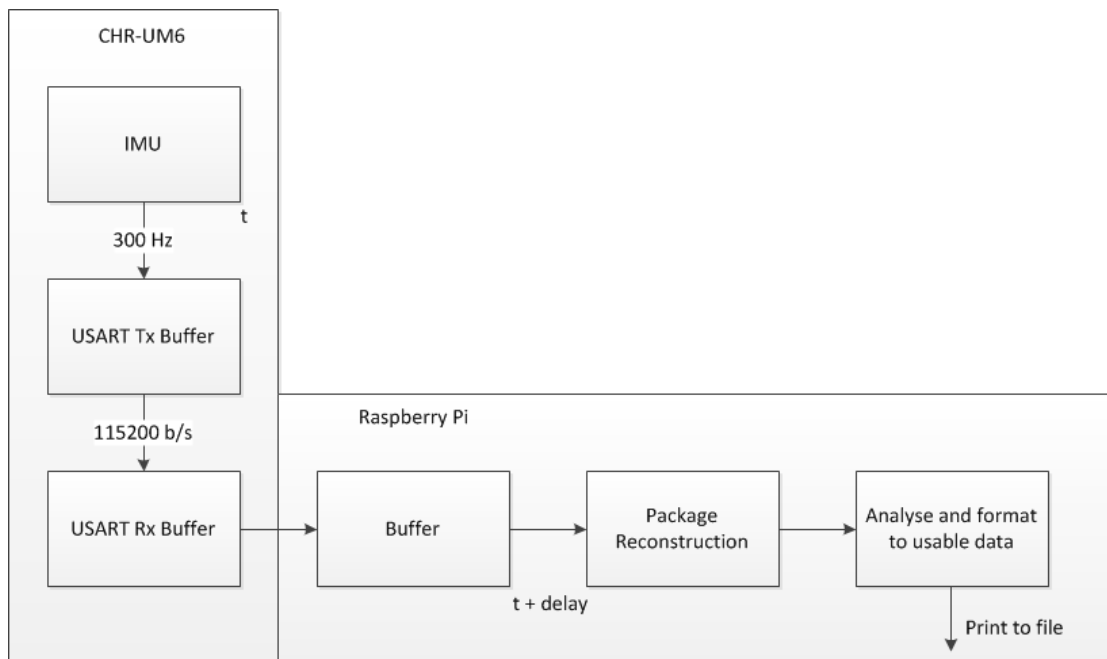


Figure J.46: Layout of the interface for the CHR-UM6 IMU sensor

The internal clock of the sensor can be assumed to be accurate and needs to be configured to send data at 100Hz. The broadcast rate can be set using increments of 0 to 255. First the exact broadcast frequency was determined. From the manual the frequency can be set using [26]:

$$f = \frac{280}{255}R_{br} + 20 \quad (\text{J.42})$$

- f = the broadcast frequency
- R_{br} = the broadcast rate which can be set between 1 and 255

The closest one can get to 100 Hz is at $R_{br} = 73$ which gives a frequency of:

$$f = 100.5916Hz \quad (\text{J.43})$$

The maximum broadcast rate when all IMU data is sent is determined by:

$$f_{max} = \frac{B}{n_{data}c_{package}b_{char}} \quad (\text{J.44})$$

- B = the baudrate 115200 [*bit/s*]
- n_{data} = number of data, which consist of gyro, magnetometer, accelerometer, euler angles and quaternions, yields 5.
- $c_{package}$ = number of chars in one package, which is 7 for the checksum and the header and 8 for the data, which results in 15
- b_{char} = a char character corresponds to 10 bits.

this results in a maximum broadcast frequency of $f = 153.6Hz$, which is higher than the desired broadcast frequency.

Examining the interface in figure J.46 the signal flow can be analyzed. First it enters the transmission buffer and then the reception buffer. These processes cause an unknown but relative small delay. This delay can be measured experimentally and remains constant once determined. Secondly the data is transferred to the buffer of the computer board, which causes another delay which is dependent on the available processing power of the Raspberry PI. If the delay of processing the data is smaller than the interval of two sent packages there won't be any delay. If the processing time is longer than the interval between two packages it means it is not ready to process the new package when it is received. This package is stored in the Random Access Memory (RAM) until it has finished processing. To ensure no data is lost it has to be verified that there is enough RAM to store the delayed data. This is discussed further in section J.2.6.

J.7.1 Baro

The barometer is connected through the I^2C interface directly to the PIN header of the raspberry PI. The connections are shown in figure J.47.

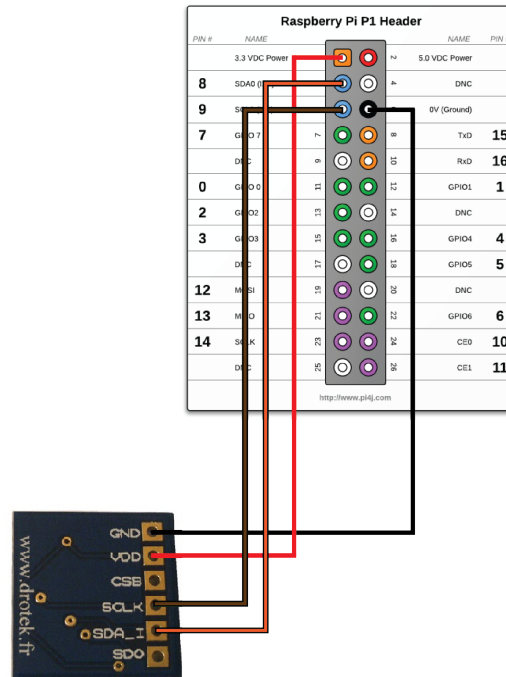


Figure J.47: Layout of the sensors connected to the Raspberry PI

In contrary to the IMU the barometer does not broadcast its measurements, but a command has to be sent before the barometer returns the value. A program has been written to obtain the values on a regular basis using.

Appendix K

Autopilot

The hardware which will be used to execute the commands to stabilize and fly the aircraft is the Lisa M autopilot [19]. The Lisa M hardware has control loops build in. The control loops in the model have to be consistent with the control loops on the LisaM. The Lisa M has an attitude control loop using a PID controller and acceleration as shown in figure K.1 [27].

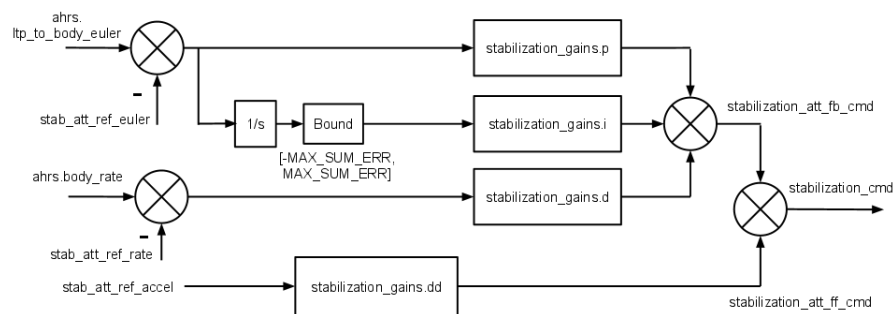


Figure K.1: Attitude control loop

The control loop consists of feed forward and feedback control. The feed forward is done through the rotational accelerations. This controller is programmed directly into Matlab. The full elaboration is shown in Appendix L

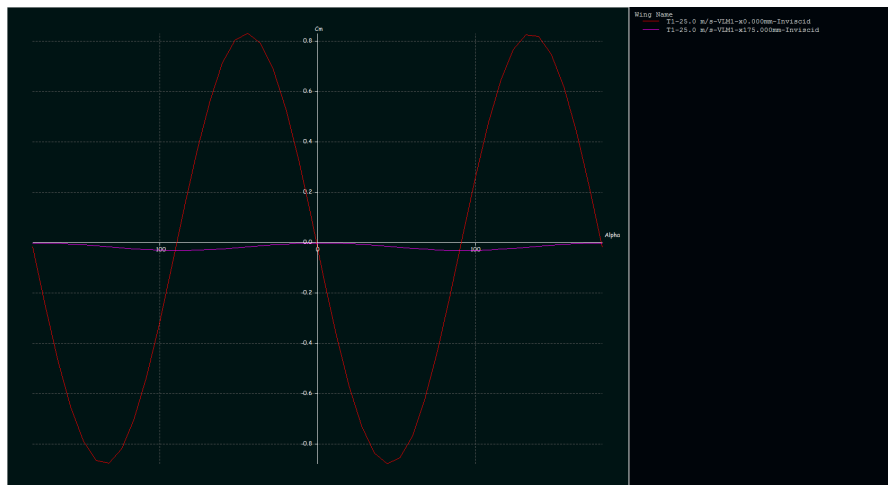


Figure K.3: XFLR5 finding the neutral point

This results in a neutral point of $x = 175\text{mm}$.

Appendix L

Attitude control

The attitude controller is programmed directly into Matlab. The controller consist of a PID feedback controller and a P feedforward controller. The dummy variables ξ and ϱ represent the euler angles, θ , ϕ , ψ and \dot{p} , \dot{q} , \dot{r} , respectively.

L.1 Feedback PID

The feedback control input is:

$$u_{FB} = K_{p\xi} (xi_{des} - \xi) + K_{d\xi} \dot{\xi} + K_{i\xi} \Xi \quad (L.1)$$

where.

$$\dot{\xi} = \begin{bmatrix} \dot{\phi} \\ \dot{\theta} \\ \dot{\psi} \end{bmatrix} = \begin{bmatrix} 1 & \sin \phi \tan \theta & \cos \phi \tan \theta \\ 0 & \cos \phi & -\sin \phi \\ 0 & \frac{\sin \phi}{\cos \theta} & \frac{\cos \phi}{\cos \theta} \end{bmatrix} \begin{bmatrix} p \\ q \\ r \end{bmatrix} \quad (L.2)$$

$$\ddot{\xi} = \frac{\partial}{\partial t} \dot{\xi} \quad (L.3)$$

$$\ddot{\phi} = \dot{p} + \cos \phi \tan \theta \dot{r} + \sin \phi \tan \theta \dot{q} \quad (L.4)$$

$$+ \cos \phi r \left(\tan(\theta)^2 + 1 \right) \dot{\theta} + \sin \phi q \left(\tan(\theta)^2 + 1 \right) \dot{\theta} \quad (L.5)$$

$$+ \cos \phi \tan \theta q \dot{\phi} - \sin \phi \tan \theta r \dot{\phi} \quad (L.6)$$

$$\ddot{\theta} = \cos \phi \dot{q} - \sin \phi \dot{r} - \cos \phi r \dot{\phi} - \sin \phi q \dot{\phi} \quad (L.7)$$

$$\ddot{\psi} = \frac{\sin \phi \dot{q} + \cos \phi q \dot{\phi} + \sin \phi \tan \theta q \dot{\theta}}{\cos \theta} \quad (L.8)$$

$$+ \frac{\sin \theta \left(\cos \phi \cos \theta \dot{r} - \cos \theta \sin \phi r \dot{\phi} \right) - \cos \phi \cos \theta^2 r \dot{\theta}}{\cos \theta \sin \theta^2} \quad (L.9)$$

L.2 Feedforward control

The feedforward control is defined as:

$$u_{FF} = K_{dd}\varrho \tag{L.10}$$

$$\varrho = \begin{bmatrix} \dot{p} \\ \dot{q} \\ \dot{r} \end{bmatrix} \tag{L.11}$$

Both controls are added to obtain the total control input:

$$u = u_{FB} + u_{FF} \tag{L.12}$$

Appendix M

Flight test

M.1 Sweeps

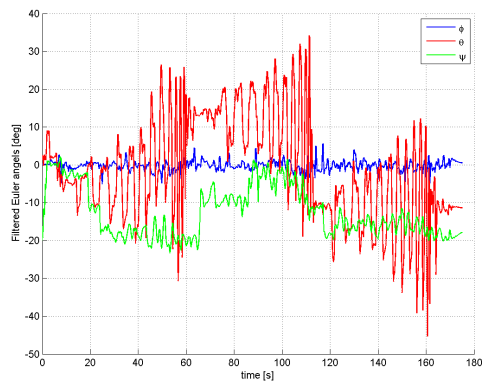


Figure M.1: Flight test pitch sweep

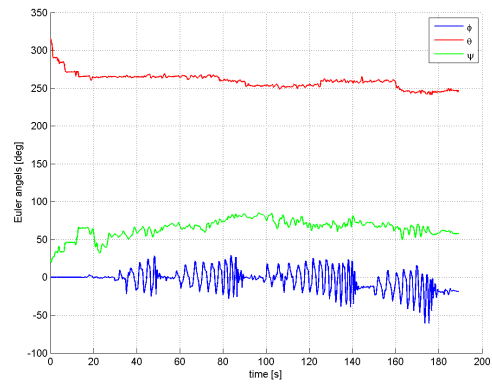


Figure M.2: Flight test roll sweep

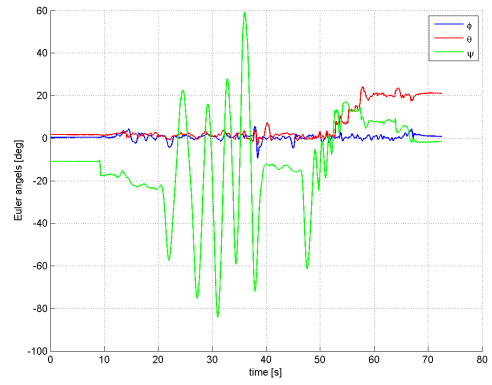


Figure M.3: Flight test yaw sweep

M.2 Steps

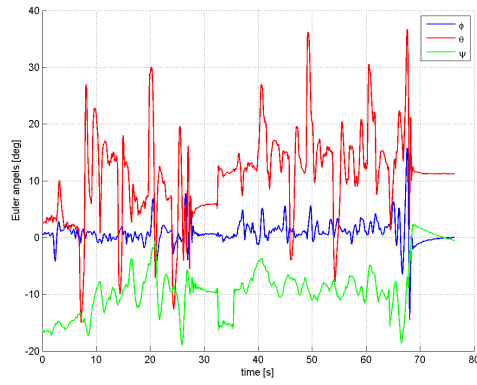


Figure M.4: Flight test pitch step

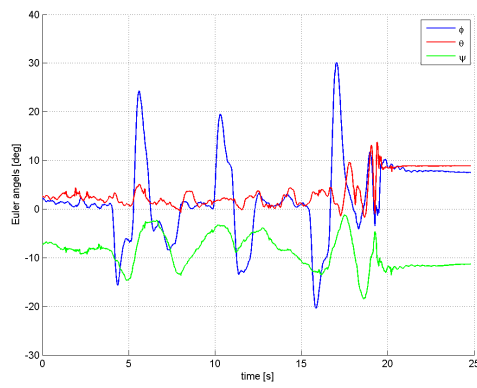


Figure M.5: Flight test roll step

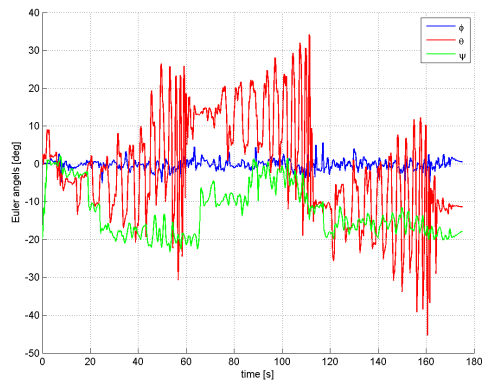


Figure M.6: Flight test yaw step

Appendix N

Checklist for flight test

Before a test flight a sequence of procedures have to be followed to ensure a proper measurement for a test flight. This includes proper calibration of the autopilot of Dr. One as the calibration of the sensors for the logging purposes.

N.1 IMU

The IMU has to have the same settings as from the traintest J.1

However different EKF settings, since the platform is not stationary any more but much more agile. More information on this can be found in appendix J.2.4.

EKF	value
Mag Variance	2
Acc Variance	2
Process Variance	1

Table N.1: Communication setup parameters

To ensure proper logging, the two USB cables have to be inserted in a specific order. First the IMU has to be connected, this will receive the identity *dev ttyUSB0* then the RPM sensors have to be connected receiving identity *dev ttyUSB1*. This is important, otherwise the log program will not work. It can be checked easily by starting up the motors to idle speed and see if the just created files, LogIMU% and LogRMP% increase in size.

Before every test session the IMU has to be calibrated, this is done with the same check list as from the train test:

Commands	
1	Zero Rate Gyro
2	Set Accelerometer Reference Vector
3	Set Magnetometer Reference Vector
Checks	
4	Check if gyros are zero see figure J.6
5	Check if acc are $[0 \ 0 \ -1]$ see figure J.3
6	Check if euler angles are $[0 \ 0 \ \psi]$ see figure J.11
7	Check for drift of euler angles, if so check EKF setting

Table N.2: Checklist before measurements

Appendix O

Checklist for flight test

Before a test flight a sequence of procedures have to be followed to ensure a proper measurement for a test flight. This includes proper calibration of the autopilot of Dr.One as the calibration of the sensors for the logging purposes.

O.1 IMU

The IMU has to have the same settings as from the traintest J.1

However different EKF settings, since the platform is not stationary any more but much more agile. More information on this can be found in appendix J.2.4.

EKF	value
Mag Variance	2
Acc Variance	2
Process Variance	1

Table O.1: Communication setup parameters

To ensure proper logging, the two USB cables have to be inserted in a specific order. First the IMU has to be connected, this will receive the identity *dev ttyUSB0* then the RPM sensors have to be connected receiving identity *dev ttyUSB1*. This is important, otherwise the log program will not work. It can be checked easily by starting up the motors to idle speed and see if the just created files, LogIMU% and LogRMP% increase in size.

Before every test session the IMU has to be calibrated, this is done with the same check list as from the train test:

Commands	
1	Zero Rate Gyro
2	Set Accelerometer Reference Vector
3	Set Magnetometer Reference Vector
Checks	
4	Check if gyros are zero see figure J.6
5	Check if acc are $[0 \ 0 \ -1]$ see figure J.3
6	Check if euler angles are $[0 \ 0 \ \psi]$ see figure J.11
7	Check for drift of euler angles, if so check EKF setting

Table O.2: Checklist before measurements

Bibliography

- [1] R. Roxxy, “Robbe roxxy bl outrunner 2827-34.” http://www.conrad.nl/medias/global/ce/2000_2999/2300/2310/2314/231423_BB_00_FB.EPS_1000.jpg, 2013. [Online; accessed 17-February-2014].
- [2] Mikrokofter, “Mikrokofter picture Quad.” https://www.mikrocontroller.com/images/MikroKopter_L4.jpg, 2013. [Online; accessed 16-July-2013].
- [3] Mikrokofter, “Mikrokofter picture Hexa.” <http://mikrokofter.altigator.com/images/mikrokofter-kits/MK-Hexa.jpg>, 2013. [Online; accessed 16-July-2013].
- [4] Mikrokofter, “Mikrokofter picture Octo.” <https://www.mikrocontroller.com/images/MK-Okto.jpg>, 2013. [Online; accessed 16-July-2013].
- [5] Transition-Robotics, “Quadshot UAV.” <http://transition-robotics.com/collections/quadshots/products/the-mocha>, 2013. [Online; accessed 22-July-2013].
- [6] Team-ATMOS, “ATMOS UAV.” <http://vimeo.com/63935988>, 2013. [Online; accessed 22-July-2013].
- [7] rcgroups, “MS5611 Barometer.” <http://www.rcgroups.com/forums/attachment.php?attachmentid=4040815>, 2013. [Online; accessed 24-September-2013].
- [8] T. Electronics, “Lab Power device.” <http://www.gelec.com.hk/eed/item/images/1240395683803.jpg>, 2013. [Online; accessed 14-October-2013].
- [9] H. Packard, “Tone Generator.” http://labaparaty.pl/index.php?id_product=1502&controller=product&id_lang=1, 2013. [Online; accessed 29-October-2013].
- [10] Matternet, “Matternet.” <http://www.matternet.us>, 2013. [Online; accessed 16-July-2013].
- [11] D. Muller, *Aircraft Performance Analysis*. VDM Verlag, 2009.
- [12] J. Anderson, *Introduction to flight 5th ed.* McGraw Hill, 2004.
- [13] J. Brandt and M. Selig, “Propeller performance data a low reynolds numbers,” *AIAA Aerospace Sciences Meeting*, vol. 49, p. 18, January 2011.

- [14] A. Schwab, "From 2D to 3D." Multibody dynamics B, 2005.
- [15] A. L. Schwab and J. P. Meijaard, "How to draw euler angles and utilize euler parameters," in *ASME 2006 International Design Engineering Technical Conferences, Computers and Information in Engineering Conference*, 2006.
- [16] S. Taamallah, "Quadcopter modeling and control." NLR-TP-2014 , 2014.
- [17] CH-Robotics, *AN-1007 Estimating Velocity and Position Using Accelerometers*, 2012.
- [18] M. V. Cook, *Flight dynamics principles*. Arnold, 1997.
- [19] Paparazzi, "Lisa M autopilot." http://wiki.paparazziuav.org/wiki/Lisa/M_v2.0, 2014. [Online; accessed March-2014].
- [20] Transition-Robotics, "Quadshot." <http://transition-robotics.com/>, 2013. [Online; accessed 22-July-2013].
- [21] Team-ATMOS, "ATMOS." <http://www.atmosuav.com/>, 2013. [Online; accessed 22-July-2013].
- [22] K. W. Eastman N. Jacobs and R. M. Pinkerton, "The characteristics of 78 related airfoil sections from tests in the variable-density wind tunnel," tech. rep., 1935.
- [23] G. E. Systems, "Understanding and Using DC Motor Specifications." DC motor, 2005.
- [24] CH-Robotics, *AN-1008 - Sensors for Orientation Estimation*, 2012.
- [25] P. S. A. Society, "A Quick Derivation relating altitude to air pressure." Barometer, 2004.
- [26] CH-Robotics, *UM6 Ultra-Miniature Orientation Sensor Datasheet*, 2012.
- [27] Paparazzi, "Control Loops Paparazzi." http://wiki.paparazziuav.org/wiki/Control_Loops, 2014. [Online; accessed March-2014].